DOPED SOL-GEL MATERIALS FOR THE PRODUCTION OF OPTICAL FIBERS

THÈSE N^{O} 3442 (2006)

PRÉSENTÉE À LA FACULTÉ SCIENCES ET TECHNIQUES DE L'INGÉNIEUR

Institut d'imagerie et optique appliquée

SECTION DE MICROTECHNIQUE

ÉCOLE POLYTECHNIQUE FÉDÉRALE DE LAUSANNE

POUR L'OBTENTION DU GRADE DE DOCTEUR ÈS SCIENCES

PAR

Urs PEDRAZZA

ingénieur en science des matériaux diplômé EPF
de nationalité suisse et originaire de Zurich (ZH) et Waltenschwil (AG)

acceptée sur proposition du jury:

Prof. R.P. Salathé, directeur de thèse
Prof. W. Lüthy, rapporteur
Prof. M. Pollnau, rapporteur
Prof. N. Setter, rapporteur

Lausanne, EPFL
2006

To my parents

Version abrégée

La technologie sol-gel offre d'intéressantes perspectives d'avenir pour la fabrication de fibres optiques, avec la possibilité d'incorporer dans un solvant approprié des dopants et co-dopants solubles. Les dopants sont ensuite homogénéisés dans la matrice.

Le sujet de ce travail a été de produire le cœur des fibres par la méthode sol-gel, afin de fabriquer des lasers à fibres optiques dopés au ytterbium, et de rechercher leurs propriétés.

La démarche sol-gel de ce travail a été adaptée pour produire, avec succès, des lasers à fibres optiques dopé au ytterbium par la méthode sol-gel. Ce procédé chimique comporte de l'eau et de l'alcool, dont les groupes hydroxyles atténuent fortement la lumière. La méthode de déposition du cœur de la fibre a été étendue par un traitement complémentaire thermique à 1800°C. Cette vitrification intermédiaire, entre la déposition de couches successives, a été appliquée pour minimiser la concentration du groupe hydroxyle dans le cœur et pour homogénéiser les couches déposées avant de collapser le tube dans une préforme et ensuite de tirer des fibres. Dans le cas d'une fibre mono-mode, le cœur a été assemblé avec trois couches épaisse de 2.7 μm chacune. Pour les fibres multi-mode, six couches ont été déposées. Après les avoir collapsées, les préformes ont été tirées en fibres.

Les fibres sol-gel obtenues ont été étudiées par rapport à leurs propriétés structurelles et optiques. Les fibres présentent un cœur avec une section de forme radiale. Cette structure est connue de certaines fibres produites par déposition chimique de vapeurs modifiées (MCVD). La distribution des tensions mécaniques dans les fibres sol-gel étudiées sont dans le même ordre de grandeurs que les fibres MCVD. Les fibres présentent des pertes de 31 dB/km à 1100 nm.

L'activité laser a été démontrée avec un seuil compris entre 32 mW et 90 mW, et une efficacité d'émission laser allant jusqu'à 73%. La puissance de sortie maximale de 44 mW a été limitée par la pompe.

Abstract

The sol-gel technology offers highly interesting prospects for fiber fabrication. The main advantage is the possibility to incorporate any dopants and co-dopants soluble in a suitable solvent. Generally, these dopants are homogeneously dissolved in the matrix.

The objective of this work is to produce fiber cores with the sol-gel technique, to fabricate ytterbium doped sol-gel fiber lasers, and to investigate their properties.

The sol-gel route was adapted to successfully build ytterbium doped sol-gel fiber lasers. This wet chemistry process involves water and alcohol, but the hydroxyl groups of these liquids highly attenuate guided light. The fiber core deposition was therefore extended with thermal annealing at 1800 °C for vitrification and to minimize the hydroxyl group content in the fiber core. In case of a mono-mode fiber laser the core was built with three 2.7 μm layers. These layers were deposited with this intermediate vitrification applied between subsequent layers. In the case of multi-mode fibers six layers were applied similarly. After collapsing, the preforms were drawn to fibers.

The produced fibers were investigated in view of structural and optical properties. The sol-gel fibers show cores with a radial structure in their cross sections. This structure is also known from the modified chemical vapor deposition (MCVD) technique. The stress distribution within sol-gel fibers is in the same range as in MCVD fibers. The fibers show losses of 31 dB/km at 1100 nm.

Laser action has been demonstrated. With thresholds between 32 mW and 90 mW a slope efficiency of up to 73 % has been reached. The maximum output of 44 mW was limited by the available pump power.

Table of Contents

1 Introduction **13**

2 Silica Fibers **15**
2.1 Dopant and Co-Dopant 15
2.2 Weakly Guiding Fibers 19
2.3 Attenuation of Light 22

3 Sol-Gel Technology **27**
3.1 Overview 27
3.2 Chemistry 28
3.3 Coating 33

4 Preform and Fiber Processing **37**
4.1 Intermediate Vitrification 37
4.2 Collapsing 39
4.3 Preform Investigation 39
4.4 Drawing 45

5 Fiber Properties **49**
5.1 Attenuation 49
5.2 Microstructure 52
5.3 Stress 53
5.4 Spectroscopy 60

6 Laser **63**
6.1 Ytterbium 63
6.2 Yb^{3+} Sol-Gel Fiber Laser 66

Appendix **69**
A Index of Refraction 69
B Fluorescence Lifetime of Small Nd^{3+} Doped Particles 70
C Photonic Crystal Fiber 82
D Chemistry 83
E Stress Determination 85
F Bleaching 89
G Laser Equations 91

Bibliography **97**

Acknowledgments **111**

Curriculum Vitae **113**

1 Introduction

Since the realization of the first rare-earth doped low-loss single-mode optical fiber in 1986 [1], the modified chemical vapor deposition (MCVD) is the standard production method for industrial applications because of the excellent degree of purity achievable. The substrate for MCVD deposition is generally a rotating silica tube. A combination of $GeCl_4$, $SiCl_4$, phosphorous, fluorine, O_2 and He gases is injected into the tube. An electrical furnace or an oxyhydrogen or plasma torch travels along the tube and heats the gases up to about 2000°C. The gases react with each other and a porous soot layer of SiO_2 is formed inside the tube. For passive fibers, the soot is directly vitrified into a layer of glass by the traveling furnace. For active fibers, before vitrification the soot is soaked with additional dopants. Then, the tube is collapsed and drawn to fibers. [2-4]

The present work describes the production and characteristics of an ytterbium doped aluminum co-doped sol-gel silica glass fiber laser, fabricated via the sol-gel route. The sol-gel technique offers highly interesting prospects for fiber fabrication. Any co-/dopants soluble in a suitable solvent can be homogeneously incorporated in the core matrix. This gives the opportunity to develop optically active fiber cores in a wide range of dopants, concentrations and geometry in a rather elegant way. The sol-gel technique is a wet chemistry process avoiding the use of highly hazardous gases as required in MCVD technique. It is further very cost effective.
As a wet chemistry process sol-gel technique leads to a high concentration of hydroxyl (OH) groups. They originate from the solvents and from the sol-gel reaction steps. Guided light is highly attenuated by OH stretching vibrations. Another drawback is the minor purity of the sol-gel precursors, with respect to the MCVD gases.

Sol-gel produced neodymium doped fiber lasers have already been published [5,6]. As yet, however, no ytterbium doped sol-gel fibers are reported. Ytterbium shows a simple energy scheme, which prevents excited state absorption and cross relaxation. A high concentration of ytterbium therefore does not lead to quenching. It was shown that Yb can be doped up to 10 at.-% in garnet [7] without any quenching effects. Reabsorption due to the overlap between absorption and emission spectra leads to tunability of the laser emission. The laser wavelength depends on the fiber length, as shown for the range between 970 nm and 1200 nm [8,9]. Ytterbium can also serve as a sensitizer for erbium.

We adapted the sol-gel technique to build fiber cores by depositing few 2.7 μm thick layers onto the inner wall of silica tubes. The minor purity of the chemicals, compared to those of the MCVD technique, was irrelevant for the purposes of this work. The attenuation by hydroxyl groups is negligible in the 1 μm range. Nevertheless, for future applications at longer wavelengths it was also an objective of this work to minimize the hydroxyl content in the fibers.

Reduced losses are achieved with an intermediate vitrification at 1800 °C between the depositions of subsequent layers. The produced ytterbium doped aluminum co-doped mono-mode as well as a multi-mode fiber lasers are described as follows.

Silica Fibers (chapter 2). This chapter describes the properties of dopants and co-dopants for active fiber cores, the principles of cylindrical waveguides and the mechanisms of light attenuation.

Sol-Gel Technology (chapter 3). The physics and chemistry of sol-gel technology is introduced and the procedure applied in this work is presented.

Preform and Fiber Processing (chapter 4). The intermediate vitrification to minimize the hydroxyl group content and to homogenize the sol-gel layers is described. The tube collapsing, the fiber preform properties and the fiber drawing are illustrated.

Fiber Properties (chapter 5). Results of the fiber characterization such as absorption spectroscopy, scattering losses, core microstructure and induced stress are reported.

Laser (chapter 6). Even with the first attempt laser action was achieved in these sol-gel fibers. The performances of the different ytterbium doped aluminum co-doped sol-gel silica glass fiber lasers are presented.

2 Silica Fibers

The silica fiber cores in this work are doped with Yb^{3+} and co-doped with Al^{3+} (section 2.1). These optically active cores provide guiding of light (section 2.2). Attenuation of the guided radiation is treated in section 2.3.

2.1 Dopant and Co-Dopant

The used concentration of the optically active dopant does not sufficiently rise the refractive index of the core to enable guiding of light. A co-dopant has to be added. The used co-dopant is alumina.

The refractive index is influenced by the amount of dopants and co-dopants, by wavelength, temperature, thermal history and fiber tension. The effects of the dopants and co-dopants are described below and the influence of stress is described in chapter 5, *Fiber Properties*. Other mechanisms are neglected for the data in this work. They may be very important for telecommunication fibers but are secondary for short laser fibers. For general information about the dependence of the index of refraction on wavelength and temperature refer to Appendix A.

Dopant

Amongst trivalent rare earth (RE) ions, the smallest ion Ce^{3+} owns a single 4*f* electron, whereas the biggest ion Yb^{3+} owns thirteen. The 4*f* electrons are shielded outwards by a noble gas configuration shell. For the rare earths Pr^{3+}, Nd^{3+}, Sm^{2+}, Eu^{3+}, Tb^{3+}, Dy^{2+}, Dy^{3+}, Ho^{3+}, Er^{3+}, Tm^{3+}, Tm^{2+}, and Yb^{3+} laser action of the 4*f* shell was demonstrated. Cerium does not show lasing transition in the 4*f* shell; the small single energy gap is easily quenched by multi-phonon processes. On the abscissa in Fig. 2.1 are the RE denoted with ascending atomic number, the ordinate shows the position of the different energy levels in wave numbers (cm^{-1}). The wave numbers in reciprocal or inverse centimeters are defined as follows,

$$\tilde{\nu} = \lambda^{-1}, \tag{2.1}$$

where the wavelength in vacuum λ is commonly quantified in centimeters (cm).

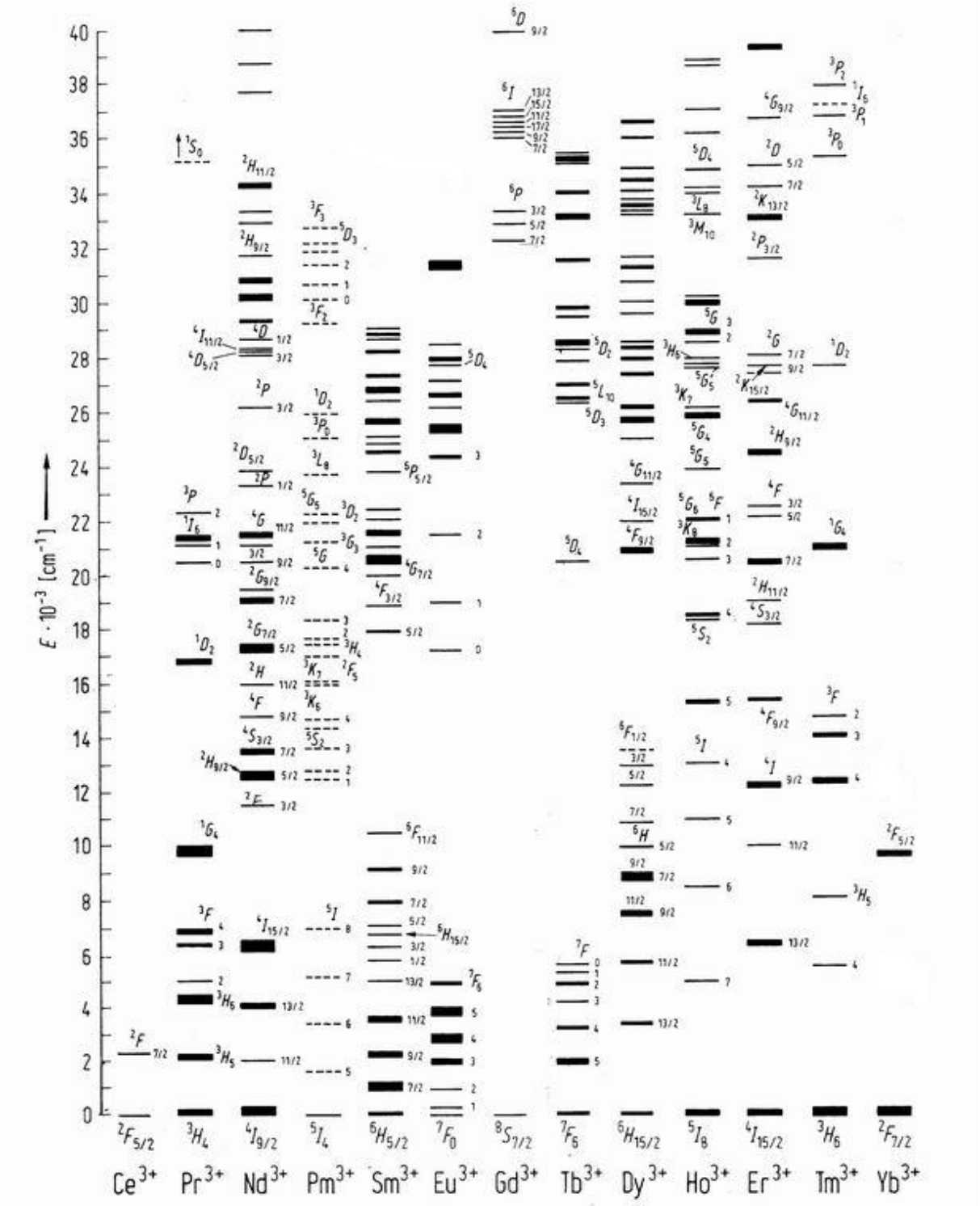

Figure 2.1 Energy levels of the RE ions. [10]

Cerium shows only tunable ultraviolet (UV) laser activity of the $5d \rightarrow 4f$ transition [11,12]. The rare earth ion Yb^{3+} used in the present work is the optically active ion. In contrast to the 3*d* shell electrons the 4*f* shell electrons of the Yb^{3+} ion are shielded by the 8 electrons of the 5*s*

and 5*p* shells. The states of these electrons only weakly interact with the ligands. The Stark level splitting amounts to only few 100 cm^{-1}. The states are very narrow-band and therefore promise laser transitions with high gain.

Some RE doped crystals or glasses are very well suited to absorb the diode wavelengths mentioned above, such as Nd^{3+}, Tm^{3+} and Yb^{3+}. Ytterbium ions absorb efficiently over the wavelength range of 800 nm to 1100 nm. When used as sensitizer for erbium, the excited ytterbium ions transfer their energy to the erbium ions, and gain between 1.53 μm and 1.56 μm is obtained. The peculiarities of the Yb^{3+} energy scheme are discussed in chapter 6, *Laser*. [9,10,13,14]

Attempts have been made to achieve laser action also with transition metals. Transition metals have a stronger interaction with the surrounding media, which can lead to the loss of laser action. Therefore transition metals are incorporated preferably in crystal hosts at well defined sites with constant site symmetry. The ideal type of host for 3*d* ions therefore is a crystal.

Fiber devices doped with embedded nanoparticles or quantum dots will open a new field of possibilities for active laser systems. Neodymium doped garnet was milled in the frame of this work to obtain sub-micron and nanoparticles. The dependence of the fluorescence lifetime on particle size was investigated, and the influence of the index of refraction of the surrounding medium on the lifetime was examined. The experiments are reported in Appendix B.

Co-Dopant

Figure 2.2 shows the influence of different co-dopants used frequently in silica fiber technology. The abscissa is the co-dopant concentration (mol-%), the ordinate shows n_D, the index of refraction measured at the wavelength of the sodium *D*-line, 589 nm [15].

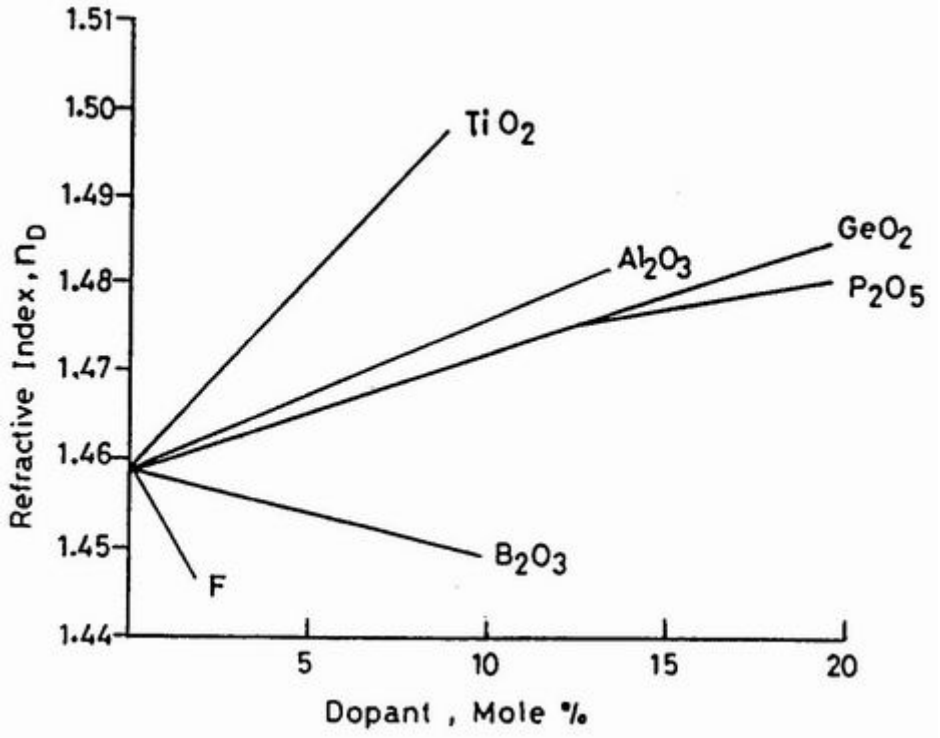

Figure 2.2 Influence of the concentration of several co-dopants on the refractive index [16].

The most effective riser of the index of refraction is titania, followed by alumina, and the germanium and phosphorus oxides, whereas with boron and fluorine the refractive index can be depressed. The refractive index n_D of alumina is 1.761 [17], of titania 2.5 and of silica 1.458 [18]. The material dispersion, the wavelength-dependent response of a substrate to waves, falls to zero at 1.3 μm in silica single-mode telecom fibers [15].

Titania in silica shows deteriorating effects on waveguide properties, as known in literature [17]. Only 4 % of titania is enough to achieve a sufficient increase of the index of 0.01. But preliminary research on planar sol-gel silica glass waveguides showed that already this small amount lead to cracked, powdery and off-peeling coatings.
Therefore alumina was chosen as co-dopant, having additionally an important advantage: ytterbium can be doped up to 10 at.-% in yttrium aluminum garnet (YAG) without any quenching effects [7], but RE ions are badly soluble in silica glass. With alumina RE ions are dissolved in Al-shells. This dissolution makes it possible to incorporate RE ions in silica. The sols for the fiber lasers were co-doped with 10 at.-% alumina as solubilizer for 1 at.-% Yb-ions [9]. The RE ions to alumina ratio 1:10 showed the best influences on spectroscopic properties of neodymium in glass [19]. Co-doping with alumina leads to two different local bonding configurations in the SiO_2 network. The tetrahedral bonding configuration of $AlO_{4/2}$ acts as a network former, and the octahedral coordination of oxygen atoms acts as a network modifier such as $AlO_{6/2}$ [9,20]. Two different types of local electric fields, two different quasi-lattice conditions surround the dopant Yb^{3+}. When doping ytterbium in crystalline alumina, it

was shown [21] that only a small amount of ytterbium ions enter the lattice as a substitute. Concentrations higher than 0.05 % of ytterbium develop $YbAlO_3$ and $Yb_3Al_5O_{12}$ phases within corundum. It was shown by Patra et al. [22], that the absorption intensities of Nd, Pr and Sm in sol-gel glasses raise with the addition of aluminum, between 2.29 % and 4.86 % for samarium, within 11.28 % and 41.50 % for praseodymium, and between 17.43 % and 69.56 % for neodymium, depending on the wavelength. This can be explained by lowering the symmetry of the ion in neighboring position to the Al ions, allowing an intermixing of the *f* states of the RE ion with higher state configuration such as 5*d*. This makes to some extend forbidden transitions more probable [22].

In the next section, the guiding of light in a core with a higher index of refraction than the cladding is discussed.

2.2 Weakly Guiding Fibers

The guiding of light in a cylindrical dielectric waveguide is based on total reflection of the light in the core at the core/cladding interface. The core has a higher index of refraction than the cladding. Total reflection occurs only if the angle of incidence between beam and the surface normal θ_i is larger than the critical angle of total reflection, θ_c,

$$\theta_i \geq \theta_c = \arcsin\left(\frac{n_2}{n_1}\right), \tag{2.2}$$

with the index of refraction n_1 of the core and n_2 of the cladding, Figure 2.3.

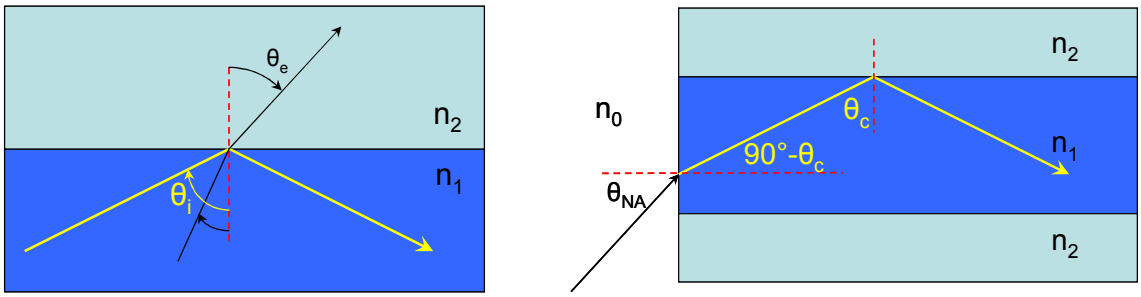

Figure 2.3 Total internal reflection and ray geometry for numerical aperture derivation.

The different propagating modes see different effective indices. The effective index describes the spatial dispersion. This phenomenon was neglected in this work. It is apparent that for total reflection to occur, n_2 must be less than n_1. For angles greater than θ_c, the sine of the exit angle $\sin\theta_e$ would be greater than 1 according to Snell's law,

$$\cos\theta_e = \sqrt{\left(1 - \frac{n_1^2}{n_2^2}\sin^2\theta_i\right)}. \qquad (2.3)$$

Therefore the light is totally reflected. Total reflection occurs when (2.2) can not be solved for real angles anymore. The angles in this case become complex. [23,24]

The fibers in this work are single-step index fibers. The single-step index fibers consist of two concentric homogeneous dielectrics. The inner dielectric, or core, fills the region $r < a$ and is of refractive index n_1. The outer material ($r > a$), the cladding, is of index n_2, where $n_2 < n_1$. Together with the core diameter a, they define the numerical aperture NA (or $N.A.$), which is the sine of the maximum angle of an incident light ray that becomes totally confined within the fiber. For all front surface angles less than θ_{NA}, the upper interface angle is greater than θ_c, and so θ_{NA} is the maximum acceptance angle of the fiber core [24,25].

Using Snell's law at the front surface along with $\sin\theta_c = n_2/n_1$, it is found with n_0 the index of the ambient atmosphere,

$$N.A. \equiv n_0 \sin\theta_{NA} = \sqrt{n_1^2 - n_2^2}\,. \qquad (2.4)$$

In this work single-mode as well as multi-mode fibers were produced and investigated. They form two classifications of practical concern. Standards on dimensions for telecommunication fibers have been set by various committees. Among these are the Electronic Industries Association (EIA), the International Electrotechnical Commission (IEC), International Telecommunication Union (ITU) and the Comité Consultatif International Télégraphique et Téléphonique (CCITT). All have specified a cladding diameter of 125 µm as the production standard for most single- and multi-mode fibers. Core diameters are usually 50 µm or 62.5 µm for multi-mode fiber and between 8 µm and 10 µm for single-mode fibers. Values for the normalized index difference Δ,

$$\Delta = \frac{n_1^2 - n_2^2}{2n_1^2}, \qquad (2.5)$$

are usually expressed in percent and are approx. 0.2 % for single-mode and approx. 1 % for multi-mode fibers. This and the expression for the numerical aperture in Eq. (2.4) are derived

for multi-mode fibers if the diameter is distinctly larger than wavelength of the guided light. Especially in case of mono-mode fibers with dimensions in the range of the wavelength, this simple geometrical model is not valuable anymore, and has to be replaced with a more complex description based on Maxwell's equations. This derivation as well as the one of photonic crystal fibers (PCF) are outside the scope of this work and can be found in textbooks [26-28]. PCF often are also referred as micro-structured fibers [24,29]. They are the more recent class of optical fiber waveguides, incorporating periodic structural features that determine the guiding properties. The first photonic crystal fibers drawn in Bern are presented in Appendix C. The word microstructure was applied in this work also in context of cross section investigations of drawn sol-gel fibers.

Most fibers used at the time for telecom applications are operated under weakly guiding conditions with the index of the core being only slightly higher than the index of the cladding [24]. The term weakly guiding was introduced by Gloge [30]. Equation (2.5) in this case is replaced by the weakly guiding approximation,

$$\Delta \approx \frac{n_1 - n_2}{n_1}. \qquad (2.6)$$

An important parameter for single-mode fibers, weakly guiding or not, is the cut off frequency. The normalized frequency is defined by

$$V = ka\sqrt{n_1^2 - n_2^2} = kaNA \qquad (2.7)$$

with a the core diameter and k the wave number ($=2\pi/\lambda$). For normalized frequencies below a critical value, the cut-off frequency V_0, all higher order modes are cut off and only the fundamental mode can propagate. The cut-off frequencies for different modes are calculated from the roots of Bessel functions, as described in detail in the literature [27,30-32]. The lowest cut-off frequency is given by $V_0 = 2.405$.

In single-mode fiber production, the cut-off wavelength λ_c is usually specified. According to (2.7), λ_c is given by $\lambda_c = 2\pi aNA/V_0$. The single bend attenuation method has become a standard technique for measuring λ_c. If a fiber with 140 mm bent radius carries two (or more) modes, the loss shows a sharp decrease if the wavelength is tuned up as soon as the higher modes do not propagate anymore at wavelength higher than λ_c. The cutoff wavelength is defined as the value of λ at which the loss has decreased to 0.1 dB above zero level in a 2 m long fiber. The attenuation mechanisms of fibers and especially of the sol-gel built silica glass fibers presented in this work are discussed in more detail in the next section.

2.3 Attenuation of Light

The mechanisms attenuating the guided light are categorized in intrinsic or extrinsic losses. The attenuation consists of radiation absorbing mechanism and scattering effects. Attenuation losses originate from the optically active ions in the matrix. Scattering losses originate from the whole matrix.

Intrinsic Losses

Intrinsic losses arise from the fundamental material properties of the glasses used in fiber fabrication. They can be reduced by appropriate choice of wavelength and through various design compromises that involve different material compositions. Figure 2.4 shows the intrisic losses of silica glass. The abscissa denotes the photon wavelength (μm), the photon energy (eV), and the wave number (cm^{-1}, Eq. 2.1), respectively. In spectroscopy the photons usually are described with wave numbers, whereas in laser physics the wavelength is more common. The ordinate in Fig. 2.4 denotes the losses (dB/km).

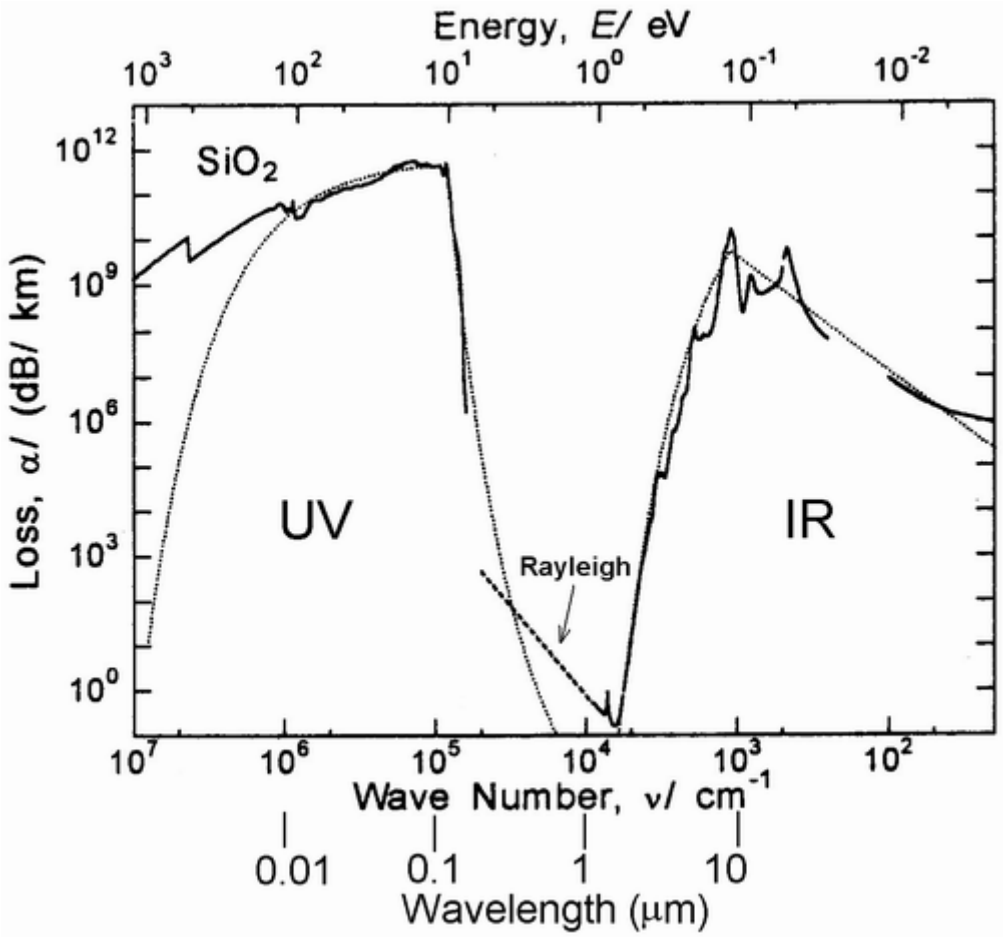

Figure 2.4 Absorption spectra of silica glass from the ultraviolet (UV) range to the infrared (IR) range. Dottet curves: model absorption spectra calculated to reproduce the measured refractive index curve; solid curves: measured spectra; broken line: Rayleigh scattering and loss spectrum of a low loss pure silica core single-mode fiber. [33]

The intrinsic losses in the ultraviolet range, up to 0.4 μm, and the infrared absorption above 2 μm are laying outside the wavelengths important for the fibers in this work. The important intrinsic mechanism in this case is Rayleigh scattering. Lord Rayleigh calculated the scattered intensity I from dipole scatterers smaller than the wavelength, to be a function of the initial intesity I_0, the number of scatterers N, the distance x from the scatterer, the polarizability α, the wavelength λ, and the observation angle θ,

$$I = I_0 \frac{8\pi^4 N\alpha^2}{\lambda^4 x^2}(1+\cos^2\theta)\,. \qquad (2.8)$$

Classically it is described by the excitation of atomic dipoles, as dipolar scattering.

The experimental determination of the scattering losses at non-absorbing wavelength relies on Beer-Lambert's law,

$$I = I_0 e^{-\varepsilon l}, \tag{2.9}$$

where l is the beam's path length, ε the scattering coefficient per length, I the measured and I_0 the launched intensity [34]. The losses at the given waveguide length (dB/km) are calculated with

$$loss_l\ (dB) = 10 \log_{10} \frac{I_0}{I}. \tag{2.10}$$

The scattering losses of a given wavelength can be converted to another wavelength by re-scaling,

$$\alpha_{s2} = \alpha_{s1} \frac{\lambda_1^4}{\lambda_2^4}. \tag{2.11}$$

One important intrinsic loss is the possible presence of micro-crystallites in the sol-gel deposited fiber core.

Extrinsic Losses

Extrinsic losses arise from imperfections in the fabrication process. They can be reduced to insignificant levels with appropriate refinements, e.g. by avoiding impurities such as transition metals [24,35-37]. The extrinsic losses in this work are led by hydroxyl groups. OH groups in silica glass induce fundamental absorption at 2.7 μm. The OH groups exist in silica as isolated (free) and hydrogen bonded states. The isolated OH induces a sharp peak at 3672 cm^{-1} (2.723 μm) and the hydrogen bonded OH induces a broad peak at 3608 cm^{-1} (2.772 μm). Absorption due to H_2O molecules also appears at 1611 cm^{-1} (6.207 μm), table 2. [33]

Table 2 Peak positions and intensities of OH absorption bands in silica glass. [38]

Wavelength (μm)	Intensity (dB/(km ppm))
2.72	10'000
2.21	201
1.38	62.7
1.25	2.7
1.14	0.07
0.94	1.6
0.88	0.08
0.72	0.08

The typical OH induced losses in the fibers appears at 1.38 µm, 1.25 µm and 0.94 µm. The 1.38 µm loss is the most intense. OH groups in MCV-deposited fiber cores are removed by dehydration in a Cl_2 atmosphere. [38-40]

It lies in the nature of the sol-gel fabrication, which in fact is a wet chemistry process, to incorporate large quantities of OH groups, by using water (H_2O) as reagent, alcohol as solvent and as by-products during condensation. So the OH groups are undesirable accompaniments of this process, their attenuation of the guided light are referred to be extrinsic losses too, although they are an inherent part of the sol-gel deposited glassy matrix.

In this work the investigated fibers were all uncoated. This involves handling with extreme care to avoid particular deteriorations while producing and handling. Figure 2.5 visualizes intrinsic and extrinsic loss origins together with the special defects caused by mishandling uncoated fibers such as dents and micro-bending.

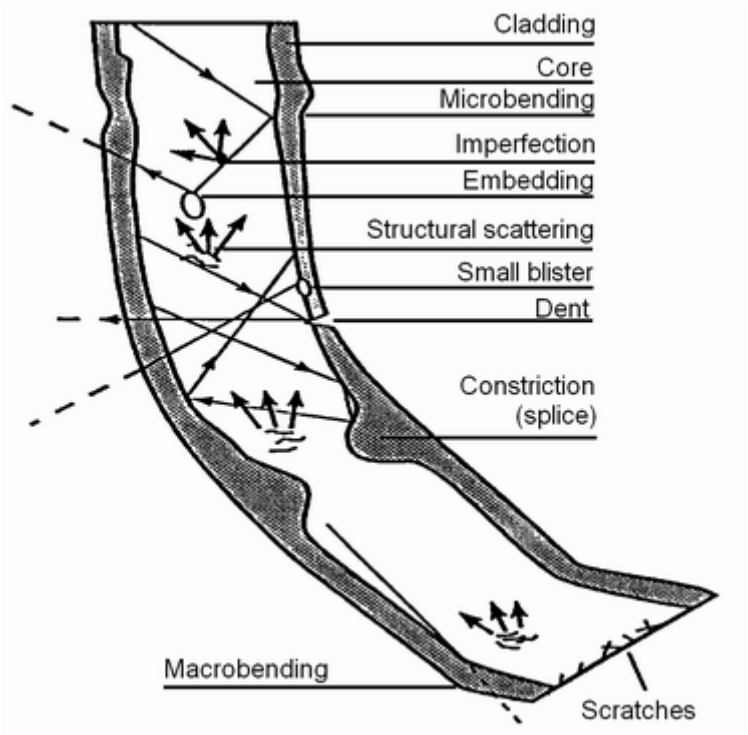

Figure 2.5 Particular deteriorations to avoid while producing and handling especially fibers. [41]

Figure 2.6 shows the different devolutions of micro- and macro-bending on the attenuation. The abscissa shows the wavelength (nm), the ordinate the attenuation (dB/km).

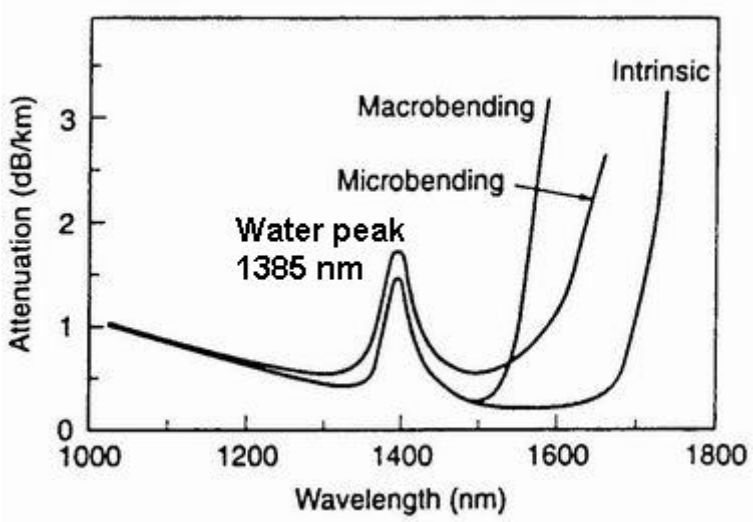

Figure 2.6 Phenomenological illustration of the effects of macro- and micro-bending on the attenuation. The water peak is located at 1385 nm. [42]

Macro- and micro-bending losses manifest themselves as rapid increases in attenuation beyond a critical wavelength. Both are associated with changes in optical mode confinement due to stress-induced changes in the refractive index profile (RIP) as a result of bending. Macrobending is easily envisioned, while micro-bending is characterized by small amplitude variations of the order of a nanometer with a periodicity of the order of a millimeter. Microbending can result from the expansion mismatches between cable components [18]. Macrobent is called a fiber when having a bend radius given by the following inequation,

$$\frac{r}{d} > \frac{n_1 + n_2}{n_1 - n_2}, \tag{2.12}$$

with diameter d and the refractive index n_1 of the core and the refractive index n_2 of the cladding [24]. Loss measurements are usually performed with a bend diameter of 280 mm, according to IEC and ITU [43].

3 Sol-Gel Technology

For beginning, a short excursion in history, back to the real first optical application of the sol-gel technique, shows another fascinating and beautiful facet of this technique.

3.1 Overview

The term *sol-gel* is a compound of the abbreviation *sol* for solution and the word *gel*, describing a dense network of fine particles dispersed in a solvent. The earliest application of sol-gel technology was during the Old Stone Age (the Upper Paleolithic), 17'000 years ago in Lascaux (France). These cave paintings of the first modern humans, the Cro-Magnon hunters, show realistic images of large animals and human handprints, Fig. 3.1. Another example, the ceiling of the painted gallery in the cave is shown in Fig. 1 on page 3 [44].

Figure 3.1 "Troisième taureau", cave painting in Lascaux (France). [45]

The early humans mixed, grinded and heat treated various stones, ores, limestones and calciumcarbonates. Beneath aluminum silicates contained in the feldspars, the incorporated compounds were e.g. turgit, a brown iron oxide, glauconite, a potassium containing aluminum silicate with yellow color, and laterite, iron and aluminum hydroxide containing rocks with intensive red color, just to mention a few. The Magdalénien-humans collected at places up to 40 km away from the cave. The early humans are called Cro-Magnons because the first skeletons were found in March 1868 in the Cro-Magnon rock shelter at Les Eyzies, and Magdaléniens

referring to one of the later culture of the upper Palaeolithic located at the type site La Madelaine, both places located in the Dordogne, France.
The special treatment of the minerals led to small particles with diameters of 100 nm and more and with pores with 6 nm diameter and more. Subsequently, the early humans stabilized hydrophobilcally the powders in water with talcum or with fats (from blood). The applied paintings show up to 750 μm layer thickness. [14,46-48]
This procedure can be summarized as the main process steps of the sol-gel technique: to stabilize a sol, a *solution of colloidal particles*, with repulsive layers and attractive London force, and to build subsequently the color painting, a gel, *dense network of fine particles in a solvent* by Brownian coagulation and London force.

Modern products of the sol-gel technique are ceramics and glasses in form of ultra-fine powders, monosized powders, particles, monolithic solids, aerogels, coatings and membranes. Technical applications are planar devices such as sensors for heat and pressure, structured materials, e.g. photonic crystals, chemical sensors and biomedical applications as entrapment of molecules for biosensors. In addition, complex geometry such as multi-core fibers or microstructured fibers with gradients in the dopant concentration or even mixed or multiple doping conditions can easily be produced. Sol-gel technique offers the flexibility of dopant content, any H_2O or ethanol soluble dopant can be incorporated, homogeneity of the dissolved parts, and adjustable processing temperatures (200 °C – 2000 °C). The sol-gel route is generally very cost-effective.
Up to now, high quality sol-gel layers have been used to fabricate Nd^{3+}-doped Al_2O_3-SiO_2 lasing fiber cores [5,6], and co-doping by MCVD of thick xerogels, deposited by sol-gel to build fiber preforms [49,50], as well as molding sol-gel derived rods and tubes for drawing [51-53] were presented. Matejec et al. [50] describes a high temperature treatment at 1600 °C, to anneal thick sol-gel layers that are additionally MCVD co-doped.

3.2 Chemistry

In today's sol-gel technique, the colloidal particles usually are produced via the chemical route. The two involved reactions are the hydrolysis and condensation, as presented in the following.

The sol-gel processing involves the synthesis of an inorganic network by a chemical reaction in solution not far above room temperature, e.g. at 40°C – 50°C. Basically, a solution is prepared that is led to react in a process called gelation. The reactions leading to gelation are hydrolysis and condensation of metal organic compounds in a solution. In this work, the forma-

tion of a silica sol-gel from the alkoxide tetraethyl-orthosilicate (TEOS) in ethanol (EtOH, C_2H_5OH) and H_2O was performed. The two reaction steps are the hydrolysis,

$$Si(OC_2H_5)_4 + H_2O \rightarrow Si(OC_2H_5)_{4-x}(OH)_x + x \cdot C_2H_5OH, \qquad (3.1)$$

with subsequent and parallel polymerization to build siloxane bonds (...-Si-O-Si-...) through condensation reactions

$$Si(OC_2H_5)_{4-x}(OH)_x + Si(OC_2H_5)_4 \rightarrow (HO)_{x-1}(OC_2H_5)_{4-x}Si\text{-}O\text{-}Si(OC_2H_5)_3 + C_2H_5OH, \qquad (3.2)$$

leading to a polymeric solution with increased viscosity. The condensation can also occur between partly or fully hydrolyzed precursor molecules, leading to the condensation also of water.

The hydrolysis can be accelerated by adding a catalyst to the solution, typically - and also used in this work - is hydrochloric acid (HCl). This transformation leads to a colloidal solution, a sol. Colloids are a stable intermediate state between solution and suspension. Sols with particles up to 500 nm are generally long time stable.

The sols in this work were used within several days after production and were shaken before application. The two reactions are presented more detailed in the following, and the most important stages are summarized at the end.

Hydrolysis

The polymerization process is commonly divided into three domains of the negative base-10 logarithm of the hydrogen ions concentration (*pH*): $pH < 2$, *pH* from 2 to 7, and $pH > 7$. Regardless of *pH*, hydrolysis occurs by the nucleophilic attack of the oxygen contained in H_2O on the silicon atom as evidenced by the reaction of isotopically (^{18}O) labeled H_2O with TEOS that produces only unlabelled alcohol in both acid- and base-catalyzed systems [17,54]

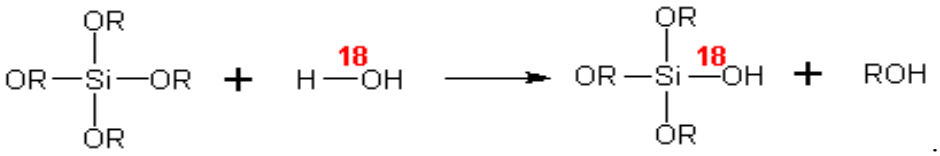

(3.3)

It can be seen in figure 3.2 how the *pH* affects the hydrolysis rate. The abscissa denotes the value of *pH*, the ordinate denotes the logarithm of the rate constant k_{spont}, -1 and +1 denote the slope of the graph.

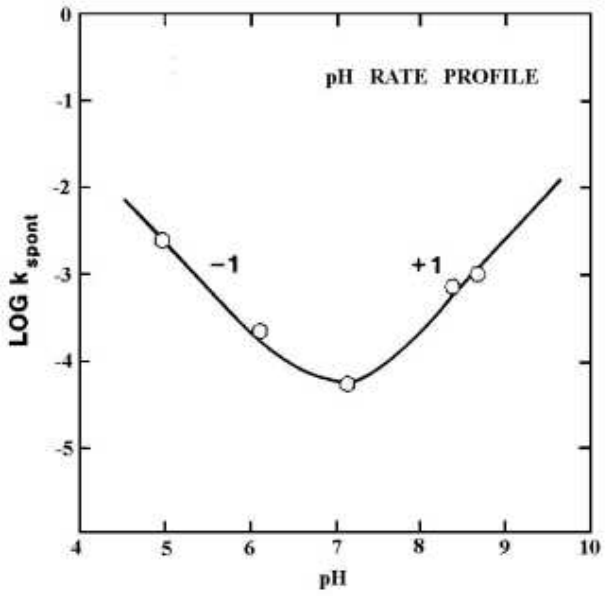

Figure 3.2 *pH* rate profile for hydrolysis in aqueous solution. [55]

Strong acidic and strong alkaline conditions enhance the rate constant. Although hydrolysis can occur without addition of an external catalyst, it is most rapid and complete when they are employed. Mineral acids, mostly HCl, and ammonia are most generally used, however, other catalysts are acetic acid, potassium hydroxide, amines, potassium fluoride, and hydrofluoric acid (HF) [17]. Under acidic conditions, it is likely that an alkoxide group is protonated in a rapid first step. Electron density is withdrawn from the silicon atom, making it more electrophilic.

Figure 3.3 shows the gel times as function of the ratios H_2O:EtOH:TEOS. The abscissa denotes the water:TEOS ratio, the ordinate denotes the time to gel (h).

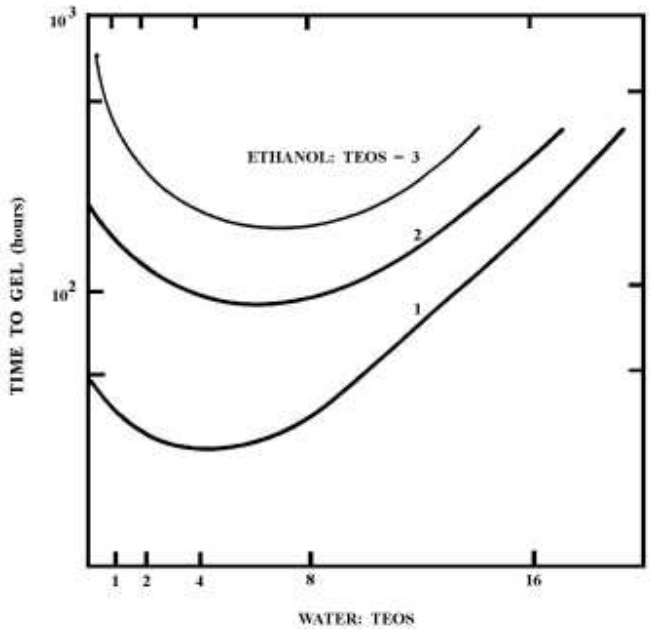

Figure 3.3 Gel times as a function of H_2O:TEOS:EtOH ratio. [17]

Low ethanol and moderate water content enhance the sol stability.

Once the hydrolysis started, the condensation reaction can begin too, and the two reactions proceed parallel.

Condensation

Between *pH* 2 and *pH* 6 condensation rates are proportional to [OH^-] concentrations. Acid-catalyzed condensation mechanism involves a protonated silanol species. Protonation of the silanol makes the silicon more electrophilic and thus susceptible to nucleophilic attack. The most basic silanol species (silanols contained in monomers or weakly branched oligomers) are the most likely to be protonated. The sol-gel transition incorporates the growth of clusters by polymerization and aggregation due to Brownian coagulation and attractive London force. Growth stops when the particles reach 2 - 4 nm in diameter [56]. Links between clusters are formed until one single macrocluster is formed over the whole sol. All sols in this work were produced in the acid catalyzed regime. Dissolution rate and relative gel time as a function of *pH* are shown in Fig. 3.4. The abscissa denotes the *pH*, the ordinate shows the logarithm of the rate of dissolution and the relative gel time respectively.

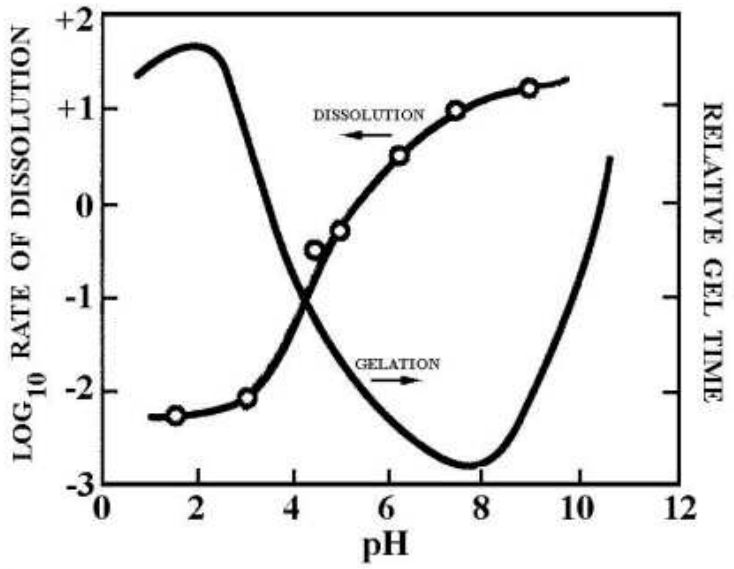

Figure 3.4 Dissolution rate and relative gel time as a function of *pH*. [17]

Summary

According to [57], sol-gel polymerization occurs in three stages:

1. Polymerization of monomers to form particles.
2. Growth of particles.
3. Linking of particles into chains, then networks that extend throughout the liquid medium, thickening into a gel.

In general sol-gel derived silicon oxide networks under acid-catalyzed conditions yield primarily linear or randomly branched polymers which entangle and form additional branches resulting in gelation. Silicon oxide networks derived under base-catalyzed conditions yield more highly branched clusters which do not interpenetrate prior to gelation and thus behave as discrete clusters, Fig. 3.5.

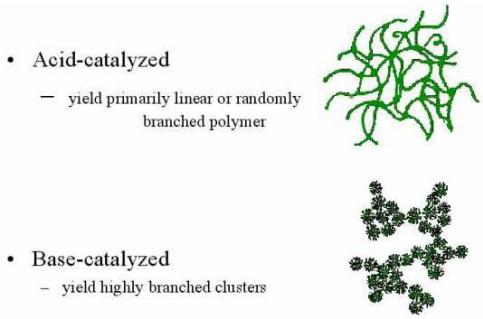

Figure 3.5 Summary of acid/base sol-gel conditions. [54]

The used chemicals and the general and particular formulations for the sols in this work are described in Appendix D.

3.3 Coating

To cover surfaces, the sol is applied via spin coating, capillary coating, roll coating, printing technique or dip coating. The method applied in this work was dip coating in the broadest sense or *inverse dip coating*, since the tubes were not dipped into the sols, but the sols were elevated in the tubes by evacuation. Figure 3.6 shows the dip coating technique, Fig. 3.7 its physics and chemistry.

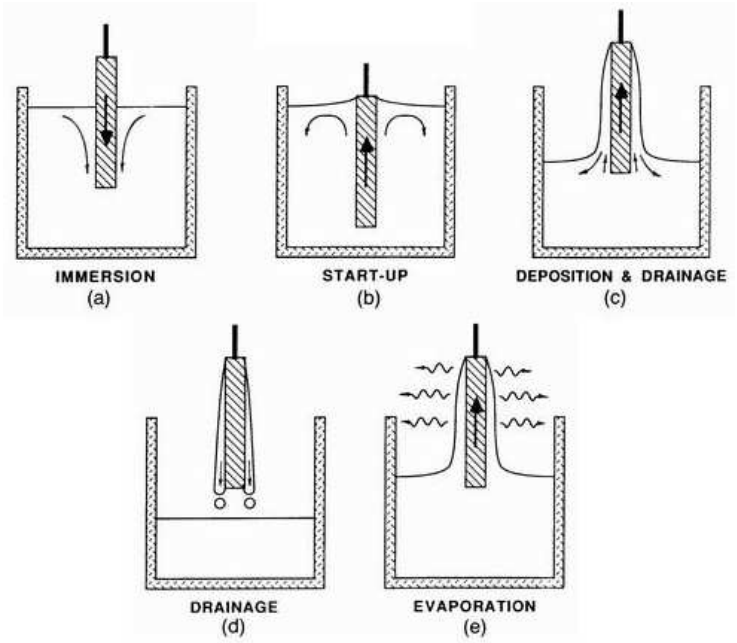

Figure 3.6 Dip coating. [17]

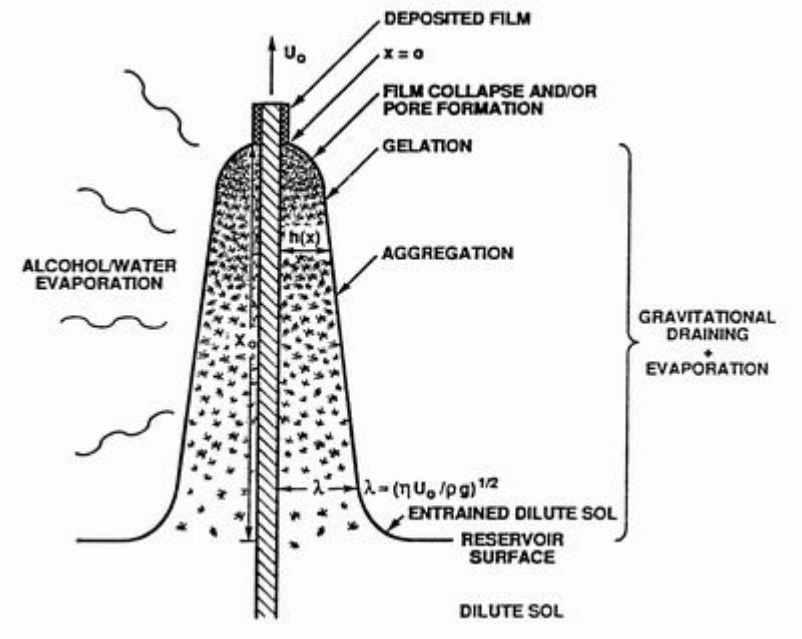

Figure 3.7 Physical and chemical processes during dipping. [17]

The same mechanisms as described in figures 3.6 and 3.7 build a xerogel layer when elevating a sol into a tube. In the tube, however, the evaporation is not uniform. The solvent builds a saturated atmosphere within the tube that gravitates and exits the tube at the lower end. Ambient air flows into the tube from the upper end. The evaporation rate therefore depends on the position in the tube. Nevertheless in our experiments no significant variation of layer thickness was observed. The coating thickness d can be calculated by the Landau-Levich equation,

$$d = 0.94 \frac{(\eta v)^{\frac{2}{3}}}{\gamma_{LV}^{\frac{1}{6}} (\rho g)^{\frac{1}{2}}}. \qquad (3.4)$$

with the liquid-vapor surface tension γ_{LV}, the density ρ, the viscosity η and earth' gravity g. This equation is valid only for planar waveguides, but not for tube inner wall coatings. The coating thicknesses were measured in this work with mechanical profilometry on planar layers, and with optical profilometry applied to preforms.

The dependence of the gel microstructure on the sol formulation is summarized in table 3. [14,17,54,58-61]

Table 3 Effect of sol formulation on gel microstructure.

TEOS (moles)	EtOH (moles)	H_2O (moles)	Average Pore Radius (nm)	Surface area (m^2/g)	Total Pore Volume (cm^3/g)
1.0	4.0	4.0	8-10	550	3.50
1.0	3.0	6	6	650	2.61
1.0	2.0	5	3	750	2.00

Xerogel layers usually are thermally annealed after depositing. The term *annealing* is used for post-processing methods that improve certain film or surface properties. For example, a surface can be thermally heated (annealed) to remove internal stresses or to complete oxidation. Thermal post-treatment densifies the xerogel, burns out organic by-products and reduces the OH group content. Annealing also completes the reaction of non-reacted TEOS in the film.

Before coating, the silica glass tubes consisting of Herasil-3, Heralux-WG or HSQ 300 (Heraeus Quarzglas GmbH & Co. KG, Kleinostheim Germany) were cleaned with diluted HF. The resulting silica removal is far below 5 µm since the concentration of the applied HF is only a few percents (25 wt.-% HF ablates approx. 5 µm during 5 minutes exposure time [62]). After drying the tube was mounted in vertically position. The tube was mounted on a stage, so that the lower opening plunged in the sol vessel. The preform was filled with the sol by reducing the pressure with a hand pump. The tube was then emptied by lowering the liquid level with a speed of 200 cm/min and subsequently flushed for 20 minutes with gaseous nitrogen for drying. Before coating with the next layer, the newly deposited layer was vitrified as described in the next chapter.

4 Preform and Fiber Processing

Three preform cores were produced with thick layers. The $Yb_{20}Ti_{6.4}(SiO_2)_{73.6}$ preform (code[1] f-9) was produced without the intermediate vitrification. Its six thick layers were vitrified during collapsing and drawing only. The fibers thereof show high scattering losses, did not lase (non-lasing fibers/non-lasing preform). The $Yb_1Al_{10}(SiO_2)_{89}$ mono-mode preform (IAP code f-20) and the $Yb_1Al_{10}(SiO_2)_{89}$ multi-mode preform (IAP code f-21) were both produced with intermediate vitrification.

4.1 Intermediate Vitrification

The term vitrification was used by Brinker and Scherrer [17] in the context of freezing pore liquid for avoiding fracture. In this work vitrification is used as thermal post-processing or thermal annealing like "*Vitrify: To convert into, or cause to resemble, glass or glassy substance, by heat and fusion*" [63]. The desired mechanisms ameliorating the sol-gel layer properties are densification of the xerogel, out-burning of organic by-products, homogenization of the structure due to partial melting, sintering, and viscous flow, and reduction of the OH group content.

The undesired accompaniment when thermal annealing metal oxides such as silica SiO_2, titania TiO_2 and alumina Al_2O_3 or binary or ternary phase diagrams out of these, is the possible re-crystallization at low cooling rates. Un-doped sol-gel silica layers showed crystallization into cristobalit at cooling rates lower than 5 °C / min as found during preliminary research. Cristobalit is the high temperature modification of silica, appearing as midget crystals, fine-fibered aggregates and scabs [14]. Cristobalit was found as well to crystallize out of commercial fused quartz at cooling rates of 5 °C/min during preliminary research.

The idea of high temperature intermediate vitrification between the depositions of subsequent thick xerogel layers was derived from the general procedure during MCVD deposition [2,50,64], where each of the up to 70 MCV deposited layer [24] experiences automatically a vitrification by the very high temperatures. An overview over the origin and subsequent development of the MCVD technique is given by MacChesney [3]. The procedure in this work resembles also a procedure reported by Matejec and coworkers [50]. They applied thick coatings together with a thermal annealing at 1600 °C, while the coatings were additionally co-doped by MCV-deposited P_2O_5.

[1] Code used in the Laser Division of the Institute of Applied Physics (IAP), University of Bern, Switzerland.

In this work each deposited sol-gel layer was vitrified on a motorized lathe (Fig. 4.1) by an electric furnace moving twice along the tube with a speed of (5 ± 1) cm/min and a temperature of the oven (1800 ± 100) °C as measured with a pyrometer. During this step, the tube was prevented from collapsing by an inner helium/oxygen gas flow with 1 kPa excess pressure.

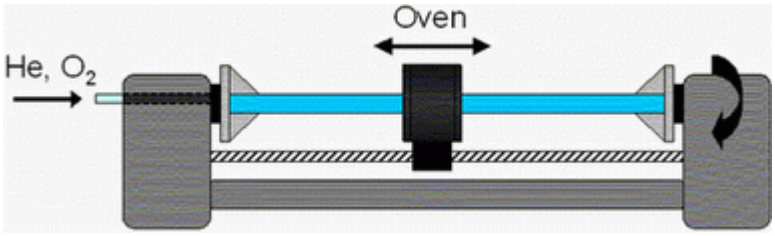

Figure 4.1 Motorized lathe.

Let c be the hydroxyl concentration in the layers during vitrification. The change of the OH content at a certain position in the layer is expressed with Fick's law in the one-dimensional, cylindrical form,

$$\frac{\partial c}{\partial t} = D\left(\frac{1}{r}\frac{\partial c}{\partial r} + \frac{\partial^2 c}{\partial r^2}\right), \tag{4.1}$$

with t the time, r the path length along the radius, and the diffusion coefficient D. D depends on temperature via the Arrhenius equation

$$D = D_0 e^{-\frac{E}{RT}}, \tag{4.2}$$

with the pre-exponential term D_0 (m^2/s) and the activation energy E (J/mol). The diffusion coefficient changes during vitrification mainly with the temperature. But also the number of interfaces influences D. Interfaces are the areas between subsequent layers. They build discontinuities in the matrix. When vitrifying later layers, the first layers still show diffusion. This diffusion is influenced by interfaces via D.

The hitherto existing IAP method was to vitrify all deposed layers during collapsing and drawing only. The OH diffusion thereby was affected by small paths of each layer and many interfaces. The new method presents thick layers, affecting the path length r, and few interfaces influencing D. However, it was appraised experimentally in this work which of these influences predominates the hydroxyl diffusion.

The Herasil type quartz used in this work is produced by flame-fusion cultured crystalline quartz grains in an oxygen hydrogen flame. Flame-fusion incorporates OH groups in the SiO_2-network. The used tubes show similar quality. The optical quality of the fiber cladding was irrelevant in this work. It only has to be denoted that OH groups can diffuse from the cladding into the sol-gel core at higher temperatures. But since the H_2O content in the sol-gel core is far above 180 ppm like in Herasil [65,66], namely in the order of magnitude of 1 mol-%, this effect was also neglectable. Furthermore the tube quartz type is specified that it is not possible to reduce OH by thermal treatment. This indicates the immobility of the OH groups in the host. Likewise other diffusion mechanisms during drawing [67] were neglected in this work since the dopant migration would have been outwards the cores in the cladding material, thereby enlarging the doped cross section area and the effective core.

The combination of applying thick coatings together with intermediate vitrification was applied three times, always with a new sol: preliminary research tubes (repeated five times with one sol), and two lasing preforms.

4.2 Collapsing

The tubes are shrunken on the lathe with temperatures of the cylindrical resistance furnace amounting to (2100 ± 100) °C. An inner helium/oxygen gas flow with 1 kPa excess pressure was applied to prevent to tubes from uncontrolled collapsing. The shrinking thereby is applied from the gas-inlet side towards to gas-outlet side. The final shrinking, the collapsing mechanism itself is a single pass of the oven with opposite direction, from gas-outlet to gas-inlet. Due to the reduced speed of the oven in this last pass the glass gets so hot from the black body radiation of the furnace that it collapses with surface tension as driving force [69]. Collapsing was done at Dätwyler Fiber Optics, Boudry (Switzerland). Before drawing, the structure, hydroxyl content, cristallinity and RIP of the collapsed preforms were investigated.

4.3 Preform Investigation

Structure

A photograph of the preform macrostructure is shown in Fig. 4.2.

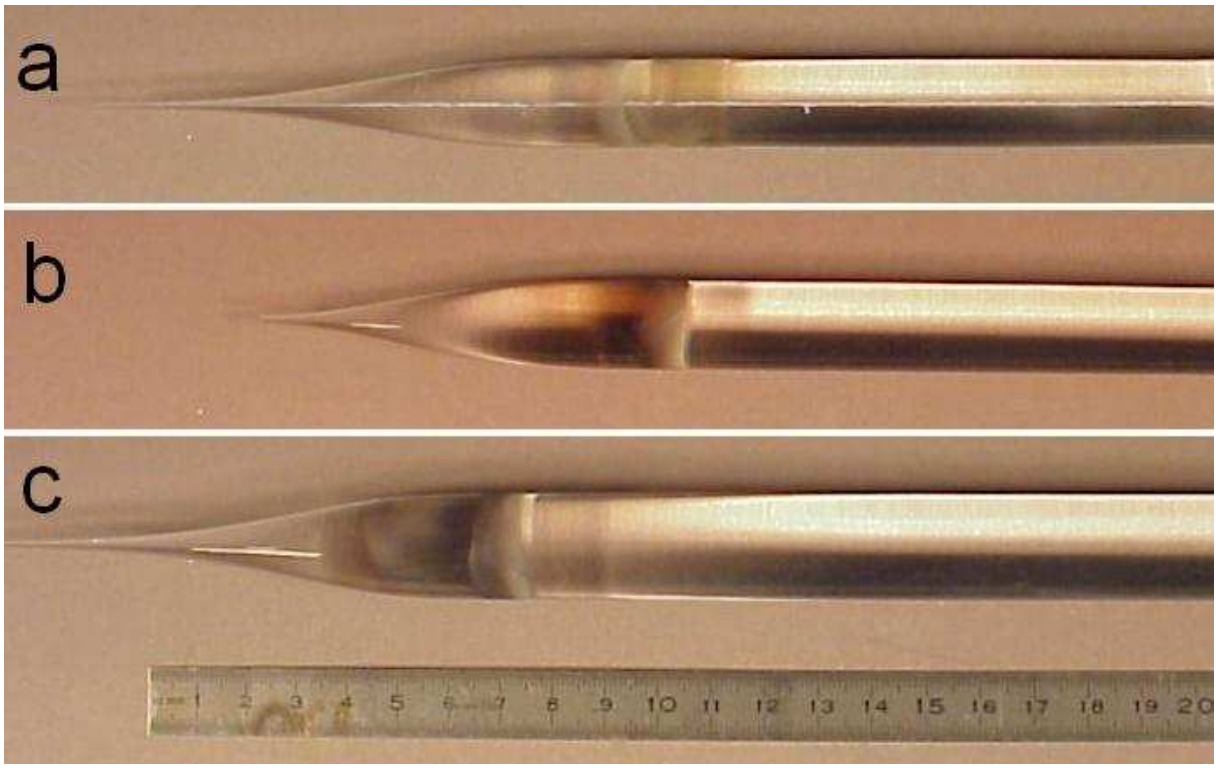

Figure 4.2 Macrostructure of a) the non-lasing preform, b) the mono-mode laser preform, and c) the multi-mode laser preform (c). The images were taken after drawing and show the neck down regions with residuals from the oven.

The core of the non-lasing preform is clearly visible in Fig. 4.2 due to scattering. The cores of the intermediately vitrified lasing preforms are invisible. Figure 4.3 shows the binocular micrographs of slides of the non-lasing preform and the mono-mode laser preform.

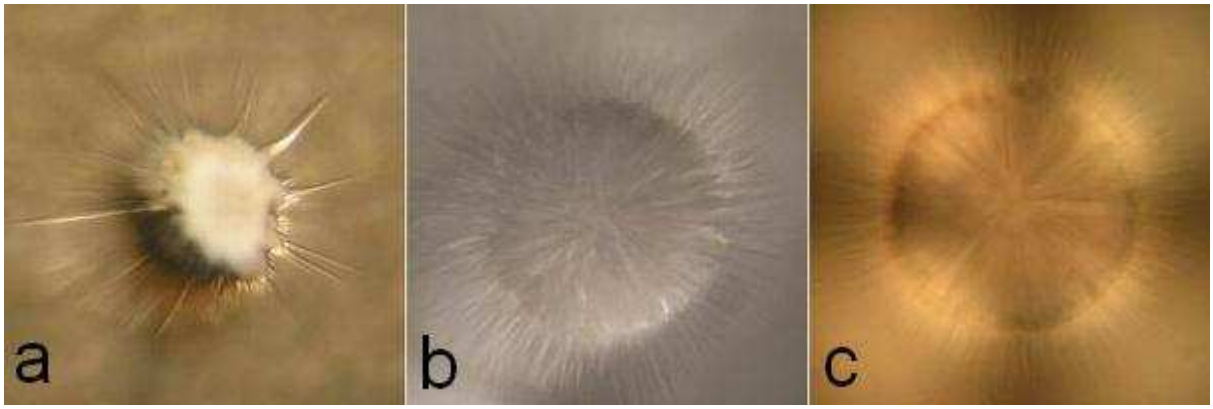

Figure 4.3 Binocular micrographs of preform slides of a) the non-lasing preform (f-9), b) the mono-mode laser preform (f-20), both with reflected light, and c) of f-20 in transmitted light modus. Edge length of each picture 4 mm.

All fiber preforms in this work have a radial structure in their cross sections. Especially the non-lasing preform shows long rays running from the core center into the cladding. This is not in agreement with the work of McNamara et al. [68] where they locate cracks particularly inside the deposited core. These authors call the core cross section “starburst”.

OH Content

Attenuated total reflection Fourier transform infrared spectroscopy (ATR-FTIR) was used (Perkin Elmer Spectrum One FTIR with Specac Golden Gate Diamond ATR, having a diamond of type IIa) to detect the OH^- -bond oscillations in the core of polished preform slides. The signal to noise ratio (SNR) of the instrument with ATR-gate amounts to 12.6 dB over the whole range.

The non-lasing preform and the multi-mode preform were investigated, together with two former IAP preforms. A Tb_5:Al_{10}:$Ti_{10}(SiO_2)_{75}$ preform was built with 19 thin layers and vitrification by collapsing and drawing [69], and a Nd_1:Al_{10}:$Ti_2(SiO_2)_{87}$ preform was built with 30 thin layers [6], also without intermediate vitrification. Figure 4.4 shows the ATR-FTIR spectra with inverse wave numbers (cm^{-1}) on the abscissa and the transmission (%) on the ordinate.

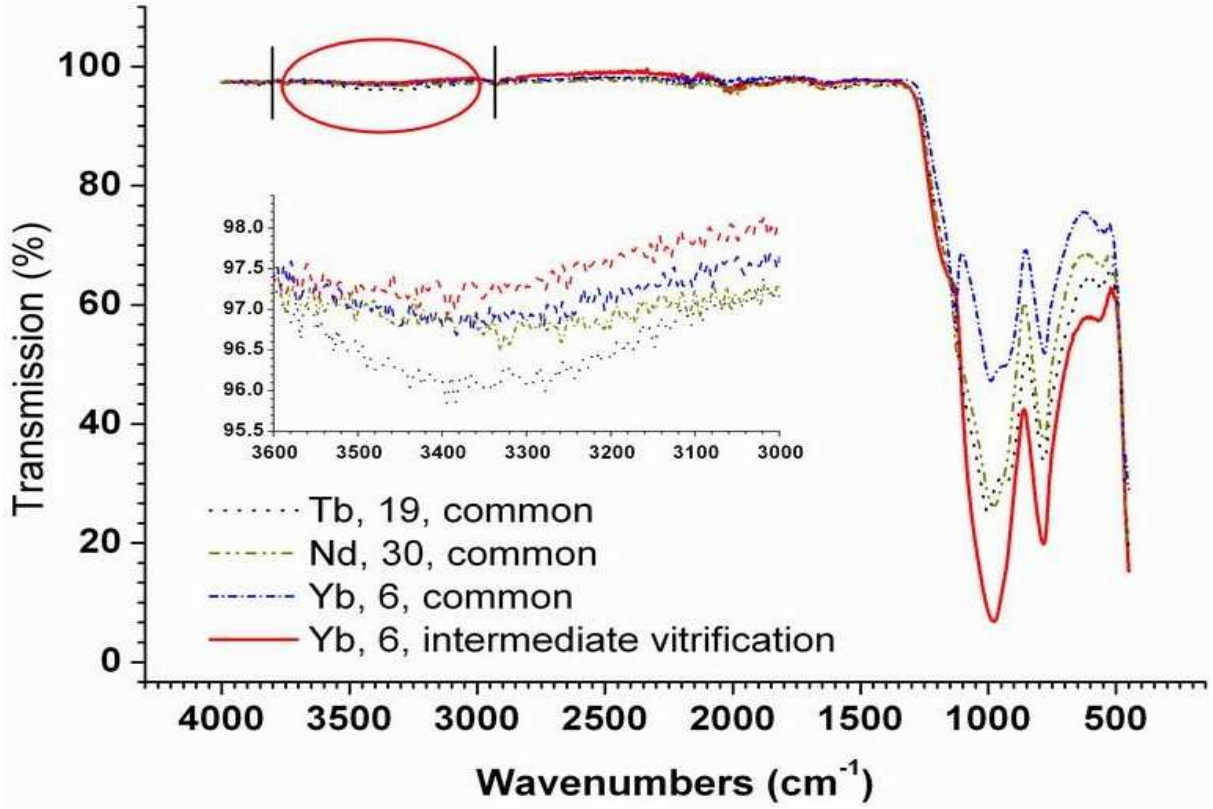

Figure 4.4 ATR-FTIR spectra. The spectra were shifted by a constant offset, thereby crossing each other at the black vertical lines.

OH groups appear around (3200-3500) cm^{-1} in case of hydrogen bondings and around (3500 - 3700) cm^{-1} in case of monomers. The data in literature [70] for the Si-O-Si vibrations are (400-500) cm^{-1}, (750-850) cm^{-1} and (1000-1250) cm^{-1}. In Fig. 4.4, the Si-O-Si vibrations cause the peaks 455 cm^{-1}, 802 cm^{-1} and 1090 cm^{-1}, superposing the Al-O-Al oscillations of this $Yb_1Al_{10}(SiO_2)_{89}$ fiber. In the region (2435 – 1775) cm^{-1}, the spectra shows disturbances caused by the instrument, as proved by reference measurements.

In the OH absorption region of 3000 cm^{-1} to 3600 cm^{-1} the instrument is at its detection limit. Nevertheless there is a tendency that shows a decreasing hydroxyl content in the order Tb-fiber, Nd-fiber, non-lasing fiber and multi-mode fiber. As therefore indicated the influence of many layer interfaces onto the diffusion constant D, Eq. (4.1) is stronger than the influence of longer path length r.

Cristallinity

To testify that the cooling ramp was steep enough to prevent components of the ternary phase diagram to crystallize out, XRD powder patterns were made routinely on polished preform slides. The laser fiber preform cores were X-ray amorphous.

Refractive Index Profile

The multi-mode preform (IAP f-21) was investigated with commercial profilometry (Dätwyler Fiber Optis, Boudry Switzerland). The RIP over the cross section was measured along the preform axis at six different positions applying refracted near-field technique with helium-neon laser wavelength (HeNe, 632.8 nm). The refracted near field technique is the industry standard to determine the RIP of optical fibers and is described in detail by White [71]. Figure 4.5 shows the RIP. The abscissa denotes the position along the preform (mm), the ordinate shows the modification of the index of refraction compared to the cladding value.

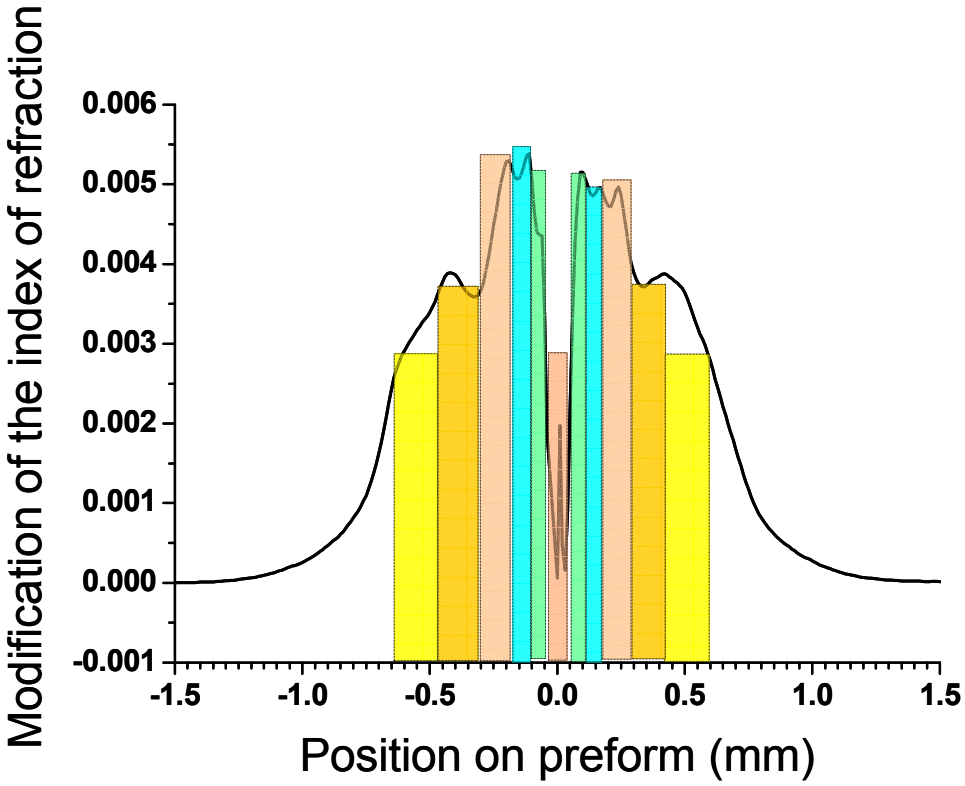

Figure 4.5 RIP of the multi-mode fiber preform. The colored bars estimate the thickness of each of the six layers.

No thickness fluctuation along the preform axis was detectable, thus the layers were uniformly deposited. The innermost layer shows a dip due to evaporation of dopants and co-dopants during collapsing. This mechanism is well known from MCVD technique and explained by the evaporation of volatile co-dopants and dopants [4]. The colored bars were applied visually and estimate the thickness of each of the six layers. Hayer and co-workers [72] found an increasement of the silica content up to more than five times in consolidated layers. Their results on a combined sol-gel and MCVD process aligns with the present results. Hayer et al. collapsed their preforms at 1950 °C, whereas we used 2100 °C (temperature of the oven). Two main mechanisms enlarge the first deposed layers compared to the innermost layers at these high temperatures: diffusion of dopants towards the cladding and evaporation of dopants out of the last deposed layers. The index of refraction of the cladding is 1.4457 ± 0.0001, the average index of refraction within the core (second moment of the index distribution, also called the core equilibrium diameter) is 1.4492 ± 0.0017. This results in an average thickness of 2.7 µm for each of the six layers. NA is 0.1 according to Eq. (2.4), Δ is 0.24 %, Eq. (2.6). These are common values for single-mode fibers [24].

4.4 Drawing

Drawing Tower

Figure 4.6 shows the schematics of the IAP drawing tower.

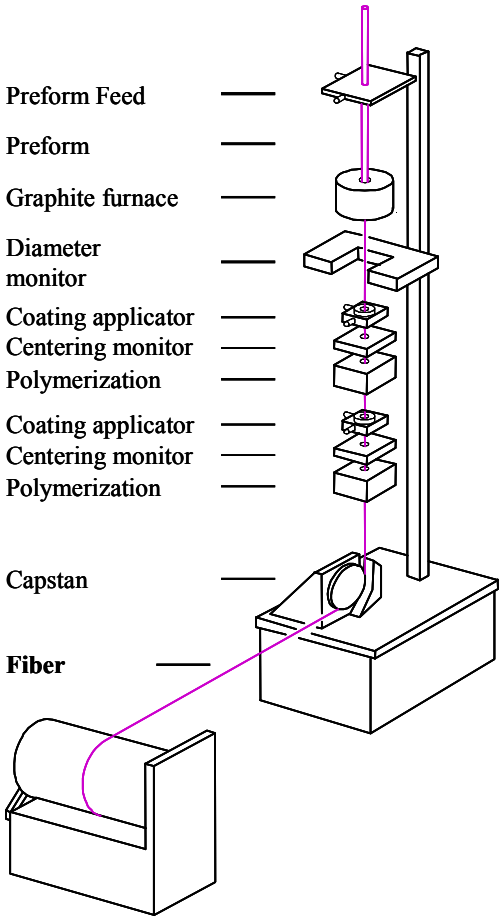

Figure 4.6 Drawing tower schematics. [64]

Especially in the temperature range from 1600 °C to 2000 °C, the viscosity of pure silica glasses can be described by Eq. (4.3)

$$\eta = 1.05 \times 10^{-10} \exp\left(\frac{E_0}{RT}\right), \tag{4.3}$$

where E_0 = 620.9 kJ/mol is the activation energy. The values relevant in this work are calculated in table 4.1. [73,74]

Table 4.1 Viscosity of pure silica glass.

Temperature		Viscosity (P)
(K)	(°C)	
2025	1750	1'088'549
2075	1800	447'640
2125	1850	191'942

The doped core has typically a decreased viscosity due to the network changes of the dopants. Since the volume fraction of the core in the fiber is 2 ‰, this influence was neglected.

The parameter range for drawing temperatures, drawing speeds and drawing tensions in this work cannot be compared to corresponding ranges in the literature. These parameters depend on the properties of the drawing tower. The drawing tower at the IAP was built as research facility.
The drawing tensiometer was operating during drawing of one fiber (f-9) only. Temperature values denoted in the following signify the measured temperature of the oven, and not the temperature of the preform.

Drawing Parameters

The applied oven temperatures, the preform feed rates, drawing speeds, and if available the drawing tensions for relevant fibers are listed in table 4.2.

Table 4.2 Relevant drawing parameters.

Fiber (IAP code)	Drawing parameters				Diameter (μm)	
	Preform feed (mm/min)	Temperature (°C)	Speed [a] (m/min)	Tension [a] (N)	Cladding	Core
Non-lasing (f-9)	0.3 ± 0.1	1800 ± 10	6 ± 0.5	0.030 ± 0.005	270 ± 7	13 ± 3
		1850 ± 10	6 ± 0.5	0.011 ± 0.01	240 ± 6	12 ± 3
			9 ± 0.5	0.019 ± 0.01	160 ± 5	8 ± 3
Mono-mode (f-20)	0.3 ± 0.1	1750 ± 10	6 ± 0.5	-	170 ± 5	8 ± 0.5
		1800 ± 10	6 ± 0.5	-	290 ± 8	13.8 ± 0.6
			8 ± 0.5	-	250 ± 7	11.9 ± 0.6
			10 ± 0.5	-	195 ± 6	9.3 ± 0.5
		1850 ± 10	6 ± 0.5	0.014 ± 0.01 [b]	225 ± 7	10.7 ± 0.6
			8 ± 0.5	0.019 ± 0.01 [b]	180 ± 5	8.5 ± 0.5
			10 ± 0.5	0.024 ± 0.01 [b]	137 ± 4	6.5 ± 0.2
Multi-mode (f-21)	0.3 ± 0.1	1800 ± 10	8 ± 0.5	-	220 ± 6	17 ± 0.7

[a] Relative values and standard deviations within each temperature only.
[b] Estimated values.

The drawing temperatures of all fibers in this work range from 1650 °C to 1850 °C, the drawing speeds from 4 m/min to 10 m/min. Within these values the mentioned fibers are in manageable ranges of thickness and viscosity, since drawing temperatures lower than 1650 °C break the fibers and temperatures higher than 1850 °C are unsuitable because the fibers are close to dropping due to their own weight at the moderate drawing speeds applied. The fibers were all drawn without applying coatings.

The diameter of the fiber depends on drawing speed (or tension) and preform feed. This is an experimentally well known behavior and also predicted by mass conservation [64,75]. When comparing the different diameters for the mono-mode fibers (f-20) shown in Tab. 4.2, this behavior seems not to be reproduced in this work. This shows that preform feed and drawing speed was not balanced leading to a shift of the neck-down region in the oven at different temperatures.

5 Fiber Properties

The results of the investigation of fiber attenuation, i.e. scattering losses and absorption, microstructure, stresses and spectroscopy of the fibers are presented in the following. The setup for optical investigations is shown in Fig. 5.1.

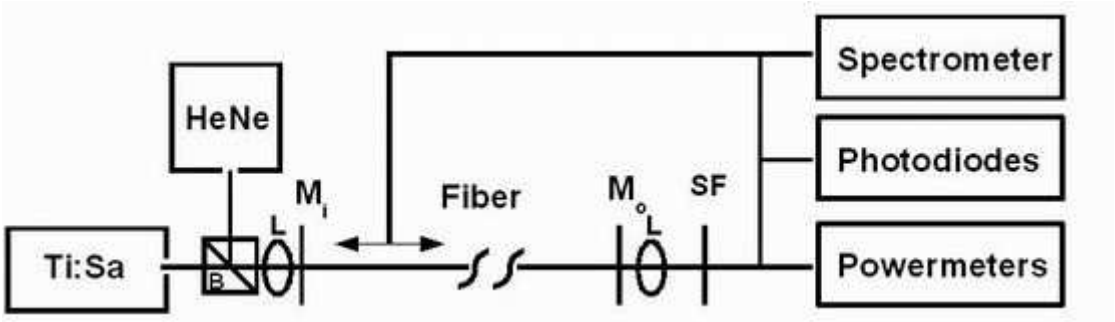

Figure 5.1 Experimental setup for determination of losses, absorption, fluorescence and laser emission spectra. Experimental arrangement for laser characterization, with the titanium:sapphire laser (Ti:Sa), the helium-neon laser (HeNe), the beam splitter (B), lenses of f = 30 mm (L), the incoupling mirror (M_i), various out coupling mirrors (M_o) and selective filters (SF, short and long pass). The spectrometer or photodiodes or powermeters have been adjusted behind the selective filters depending on the desired measurement. A movable fiber collected the signal for the spectrometer.

The equipment consisted of a stabilized HeNe laser LHP-991 (Melles Griot, Carlsbad CA, USA), a tunable Ti:sapphire laser model 3900 (Spectra Physics, Mt.View CA, USA), and a near infrared fiber spectrometer AVS-USB 2000 (Avantes, LL Eerbeek, The Netherlands). The power meters were a Model 210 (Coherent, Santa Clara CA, USA), a PD300 and a 10A (both Ophir, Peabody MA, USA). Various standard silicon photodiodes and fast germanium diodes were used.

5.1. Attenuation

Scattering Losses

The scattering losses were determined with cutback experiments at the non-absorbed wavelength 632.8 nm (HeNe radiation). The results were extrapolated to other wavelengths with Eq. (2.11). In table 5.1, the scattering losses of the present work are compared to fibers produced previously at the IAP.

Table 5.1 Scattering losses.

IAP code	Core composition	Manufacturing / Remarks	Losses $\alpha_{loss}^{1100\ (a)}$ (dB/km) when drawn @ temperature (°C)
f-9	$Yb_{20}Ti_{6.4}(SiO_2)_{73.6}$	Vitrification by collapsing and drawing	> 7'338 ± 2'190 @ 1800 (b)
f-20 and f-21 (c)	$Yb_1Al_{10}(SiO_2)_{89}$	Mono-mode or multi-mode fibers, intermediate vitrification	58 ± 4 @ 1800 31.2 ± 2.2 @ 1850
Nd-IAP(d)	$Nd_1{:}Al_{10}{:}Ti_2(SiO_2)_{87}$	Common technique, vitrification by collapsing and drawing only	181 @ 1850
Tb-IAP(e)	$Tb_5{:}Al_{10}{:}Ti_{10}(SiO_2)_{75}$	Common technique, vitrification by collapsing and drawing only	2'190 ± 329 @ 1850
Tb-IAP	$Tb_2{:}Al_{10}(SiO_2)_{88}$	Common technique, vitrification by collapsing and drawing only	53 (f) @ 1800

(a) Extrapolated from the HeNe wavelength with Eq. (2.11).
(b) Upper loss detection limit.
(c) The loss measurements have been recorded on f-21 (multi-mode fiber) and transferred to f-20 (mono-mode fiber).
(d) No standard deviation calculated. Data from literature [6].
(e) As measured on a Tb-doped fiber drawn at the IAP, similar to fibers described by [69], but with titania as additional dopant.
(f) Measured on a 1.75 m long fiber, no standard deviation calculated. Data from [69].

The non-lasing ytterbium doped fiber (f-9) showed no more guided light above detection limit in the core after 31 cm. The losses of the multi-mode Yb^{3+} doped laser fiber produced with intermediate vitrification and drawn at 1850 °C shows the lowest scattering losses. This measurement was performed on a 28 m long fiber, and this value has the smallest standard deviation. The data for the last Tb fiber was taken from literature. This loss value was measured on a 1.75 m long fiber; the standard deviation was not reported [69]. The losses of the only other published fiber lasers with its core built with sol-gel layers show losses amounting to 100 dB/km at 1.06 μm [5], or 181 dB/km [6]. They are both Nd^{3+} doped lasers.
Titania co-doping apparently increases the scattering losses. As reported in detail in chapter 6, *Laser*, the intermediately vitrified Yb^{3+} fiber lasers show slope efficiencies up to 73 %. This is much higher than the sol-gel neodymium fiber lasers reported in literature. They have 3.5 % ([6] titania co-doped) or 42 % ([5], alumina co-doped) slope efficiency. Although Nd^{3+} has lower quantum efficiency than Yb^{3+}, this indicates that the intermediate vitrification could also enhance the neodymium doped sol-gel fiber laser efficiency.

Derived from the cutoff frequency in Eq. (2.7), the cutoff wavelength was calculated to be 828 nm in case of the mono-mode fiber f-20 and 1.36 μm in case of the multi-mode fiber f-21.

Absorption

The absorption of the laser fibers was determined with low pump power to avoid the influence of ground state bleaching. Bleaching is described in detail in Appendix F. In Appendix G, *Laser Equations*, the small signal gain of an absorbing fiber is discussed.
The extinction coefficient at the pump wavelength was α_{ext}^{908} (335 ± 20) dB/m, measured by recording the fluorescence light emitted perpendicularly to the fiber axis while exciting the fiber at 908 nm. After subtracting the scattering losses this leads, together with the concentration of the absorbing species of 7.65 x 10^{19} cm^{-3}, to an absorption cross section σ_{abs}^{908} of (1.01 ± 0.11) x 10^{20} cm^2. The loss of ytterbium ions due to evaporation during vitrification and collapsing is not included in this standard deviation. Table 5.2 compares this value with data from literature for different silica hosts.

Table 5.2 Absorption cross sections in silica hosts.

Host	Yb conc.	σ_{abs} at which wavelength	Reference
Pure silica glass	0.2 at.-%	0.6 x 10^{20} cm^2 912 nm	[76]
		2.6 cm^2 974 nm	[77]
Silica with 10 at.% Al	1 at.-%	(1.01 ± 0.11) x 10^{20} $cm^{2\,(a)}$ 908 nm	This work
Germanosilicate glass	0.04 at.-%	0.75 x 10^{20} cm^2 908 nm	[78]
Germanosilicate glass	0.055 at.-%	0.8 x 10^{20} cm^2 908 nm	[8]

(a) Standard deviation does not include loss of ytterbium ions due dopant evaporation during preform preparation.

The absorption cross section of $Yb_1Al_{10}(SiO_2)_{89}$ is comparable with that of germano silica glass, both systems were excited at 908 nm. The cross section in this work is slightly higher. Possible errors are the undetermined evaporation of ytterbium ions during preform fabrication or the presence of color centers. Paschotta et al. [78] found an unsaturable absorption of ytterbium ions in alumino-phospho-silicate and germanosilicate fibers. They supposed fast energy migration between Yb^{3+} ions towards energy trapping color centers.

5.2. Microstructure

The microstructure recorded with scanning electron microscopy (SEM; acceleration voltage between 10 kV and 30 kV) is shown in Fig. 5.2.

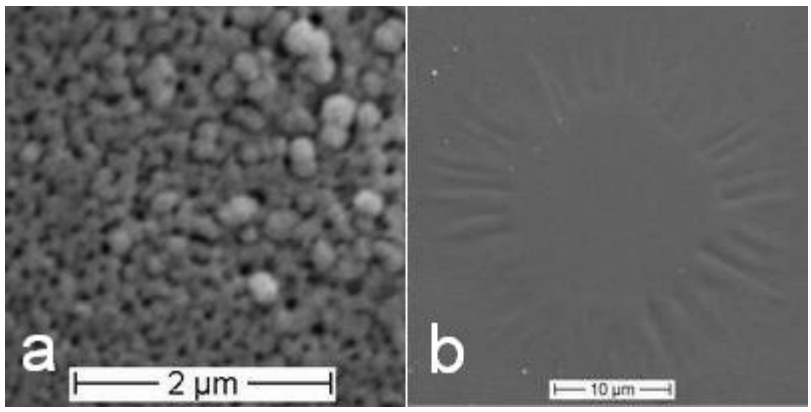

Figure 5.2 SEM micrographs of a) the core area of the non-lasing preform, and b) of the multi-mode.

The cleaved fibers have been etched for 10 minutes in 3 wt.-% HF. This pre-treatment resulted in the best SEM contrast. The fibers show radially structured cross sections also after drawing. The non-lasing titania co-doped fiber (f-9) shows a powdery core (Fig.5.2a). To investigate the influence of increased temperature, the mono-mode fiber f-20 was investigated when drawn at two temperatures, 1800 °C and 1850 °C. Both drawing temperatures resulted in the same fiber cross section images (the fiber drawn at 1850 °C is shown in Fig. 5.2b).
The cross section of the multi-mode laser fiber f-21 without the radial rays is approx. 18 µm wide. This corresponds to the value 17.8 µm, as obtained by RIP. Adding the area with radial rays results in a 31 µm wide cross section. This suggests the rays running from the core into the cladding, again in contrast with the works of McNamara et al. [68] and An et al. [79] about "starburst" cores. The problem behind this calculation is the unknown lateral resolution of the commercial RIP. Therefore a SEM micrograph was recorded with backscattered 25 keV electrons to show the distribution of ytterbium within the cross section, Fig. 5.3.

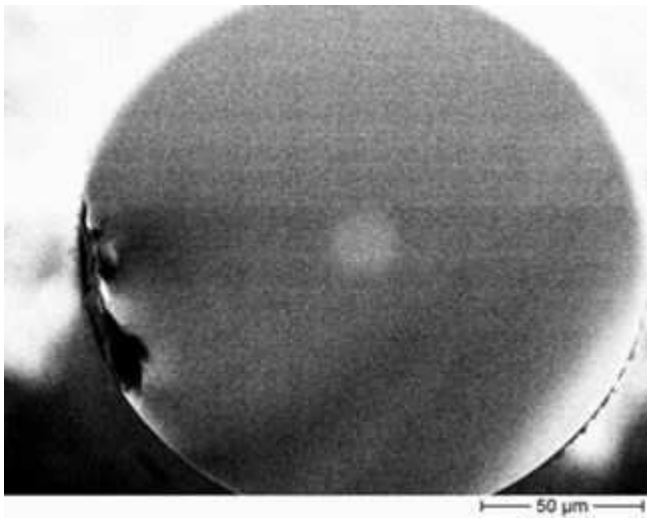

Figure 5.3 SEM micrograph recorded with backscattered 25 keV electrons.

The core is clearly visible, the cross section is approx. 20 µm wide. This aligns with the homogeneous disc in Fig. 5.2b.

5.3. Stress

Experiments

The thermal history of the fiber preform is not of importance for the interpretation of the stress data in the preform [80]; in this work we therefore focus only on stress contribution by fiber drawing. During drawing, the silica glass is cooled down very fast under a constant external force. This results in a thermal stress part and a mechanically induced stress contribution. The stress profile is the superposition of these two contributions.

Mechanically induced stress is built up during drawing due to the radial variation of the viscoelastic properties of the fiber. The core shows lower viscosity during drawing than the cladding, so in this case most of the drawing tension is taken up by the cladding. When the fiber behaves more and more elastically on cooling, it tends to fix the stress in the cladding material by converting the strain to stress. Consequently, stress is frozen in the fiber after removal of the drawing tension, and essentially taken up by the cladding, with a linear dependence between external drawing force and drawing induced stress.

Thermal stresses are introduced into the fiber when cladding and core solidify, i.e. when the temperature on the fiber is smaller than the softening temperature of the glasses. The origin of

the thermal stress is a free strain that results from a mismatch in thermal expansion coefficients between core and cladding. Since the thermal stress originates intrinsically, the thermal stress integral over the two cross section areas equals zero. In general, the thermal expansion coefficient is a function of temperature. The thermal expansion coefficient of alumina at 1600 °C amounts $\alpha(T)= 9x10^{-6}$/°C, of titania at 17.5 °C $\alpha(T)= 22x10^{-6}$/°C and of fused silica $\alpha(T)= (5x10^{-7})$/°C [66,81,82]. The addition of titania lowers the thermal expansion coefficient of silica, alumina raises it [2].

The determination of the stress in a fiber relies on the measurement of phase retardation profiles, caused by the accumulated stress-induced birefringence. An introduction to the theory is given in Appendix E; the setup is shown in Fig. 5.4.

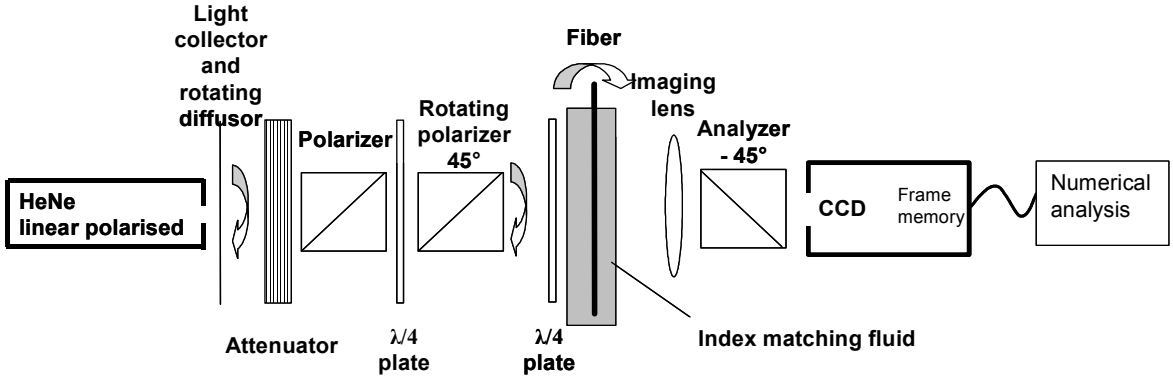

Figure 5.4 Tomography setup. The setup is assembled from a polarization controller, a Sénarmont compensator, and imaging optics.

The polarization controller consists of the combination of a polarizer, a quarter wave plate, and a second rotating polarizer. The first polarizer is illuminated with incoherent light from the laser source. Due to the high spatial coherence of the HeNe laser, a rotating diffusor is used to impair speckle formation in the image plane. The incoherent light behind the diffusor is collected by a lens (focal length 20 mm) and linearly polarized. The linear polarization is converted into circular by a quarter wave plate, whose fast axis is aligned under an angle of 45° with respect to the main axis of the polarizer. When the polarization of the incoming light is ideally circular, than the power of the transmitted light does not depend on the rotating angle. The intensity and homogeneity of the light illuminating the fiber is adjusted by a condenser situated between the quarter wave plate and the fiber. The intensity distribution of the illuminated fiber is sampled by a polarization contrast microscopy objective, which is especially designed for polarization sensitive measurements and thus does not add any birefringence. The objective images the fiber in a charged-coupled device (CCD) camera, which is

used for data acquisition. The combination of quarter wave plate and fiber turns the linear polarization emerging from the rotating polarizer. The light leaving the fiber is again linearly polarized, but its angle is turned in proportion to the retardation introduced by the fiber. To convert the change in polarization angle to a modulation of intensity, an analyzer making an angle of -45° with the fiber axis is put between the microscope objective and the CCD camera. The Sénarmont compensator thereby consists of the second quarter wave plate, the condenser, the fiber, the objective, and the analyzer. [80,83-88]

Literature data are mostly of binary cores, consisting of the silica matrix and only one dopant or co-dopant. The sol-gel fibers in this work consist mainly of the silica matrix, a dopant and one co-dopant, leading to ternary phase diagrams. We assume that the literature data in general is valid for ternary cores too.

The stress distribution 2D-tomograms of the fibers have been investigated at the Advanced Photonics Laboratory (APL), Swiss Federal Institute of Technology Lausanne, Switzerland.

The fiber f-20 (Yb_1:Al_{10}:$(SiO_2)_{89}$) in this work was investigated together with two previous IAP fibers, a neodymium doped sol-gel fiber and a terbium doped sol-gel fiber. They had the core compositions Nd_1:Al_{10}:$Ti_2(SiO_2)_{87}$ and Tb_5:Al_{10}:$Ti_{10}(SiO_2)_{75}$, both with a Herasil-3 cladding. The neodymium and terbium doped fibers are high loss fibers. They were investigated because they have different titania contents. The Nd^{3+} doped fibers has 2 at.-%, the Tb^{3+} doped fiber has 10 at.-% titania. The drawing conditions of these three fibers together with fiber dimensions and losses are summarized in table 5.3.

Table 5.3 Drawing conditions and losses of the sol-gel built fibers.

Fiber	Drawing temperature (°C)	Drawing speed [(a)] (m/min)	Drawing tension [(a)] (N)	Diameter fiber / core [(b)] (μm)	Losses [(c)]
f-20	1750 ± 10	6	-	170 / 8	(67 ± 20) dB/m @ 632.8
	1800 ± 10	6	-	290 / 13.8	-
		8	-	250 / 11.9	(0.53 ± 0.08) dB/m @ 632.8
					(58 ± 9) dB/km @ 1100
		10	-	195 / 9.3	-
	1850 ± 10	6	0.014	225 / 10.7	-
		8	0.019	180 / 8.5	(0.28 ± 0.02) dB/m @ 632.8
					(31 ± 2) dB/km @ 1100
		10	0.024	137 / 6.5	-
Nd	1800 ± 10	4	-	160 / 7.8	1.35 dB/m @ 632.8
Tb	1800 ± 10	7	-	150 / 9.4	(20 ± 3) dB/m @ 632.8

(a) Measurement of drawing speed and tension have an offset and can be used for relative comparison within on temperature only.
(b) With constant preform feed (0.3 mm /min).
(c) Determined at HeNe wavelength and extrapolated by Rayleigh's lay to wavelengths relevant for laser action.

Results

The stress values in the next table (5.4) are compared with data for germanium and phosphorus doped fibers from literature. Figure 5.5 shows stress profiles with the abscissa showing the position along the fiber diameter (μm), and the ordinates showing the stress. In fiber literature stress is usually denoted in (kg/mm^2).

Table 5.4 2-D tomographic stress measurements.

Fiber type (at.-%) in silica	Drawing temperature and drawing velocity	Fiber diameter Core diameter	Max. core stress [(a)]
Sol-gel	1800 ± 10 °C	195 µm	(1.29 ± 0.05) kg/mm^2
Yb_1:Al_{10}	10 m/min	9.3 µm	
	1850 ± 10 °C	137 µm	(0.99 ± 0.07) kg/mm^2
	10 m/min	6.5 µm	
Sol-gel	1800 ± 10 °C	160 µm	(1.16 ± 0.05) kg/mm^2
Nd_1:Al_{10}:Ti_2	4 m/min	7.8 µm	
Sol-gel	1800 ± 10 °C	150 µm	(8.2 ± 0.1) kg/mm^2
Tb_5:Al_{10}:Ti_{10}	7 m/min	9.4 µm	
MCVD	-	125 µm	-5 kg/mm^2
Ge 9 at.-% [(b)]	-	6.7 µm	
MCVD	-	125 µm	-4 – -12 kg/mm^2
P 24 at.-% [(c)]	-	6 µm	
Ge [(d)]	1900 – 2100 °C	140 µm	0.5 – 3 kg/mm^2
	5 – 60 m/min	-	

(a) Positive values denote axial tension, negative stress number denote compression.
(b) Data from [89].
(c) Depending on drawing temperature within 1800 °C and 1940 °C, data from [90].
(d) Concentration unknown, data from [84].

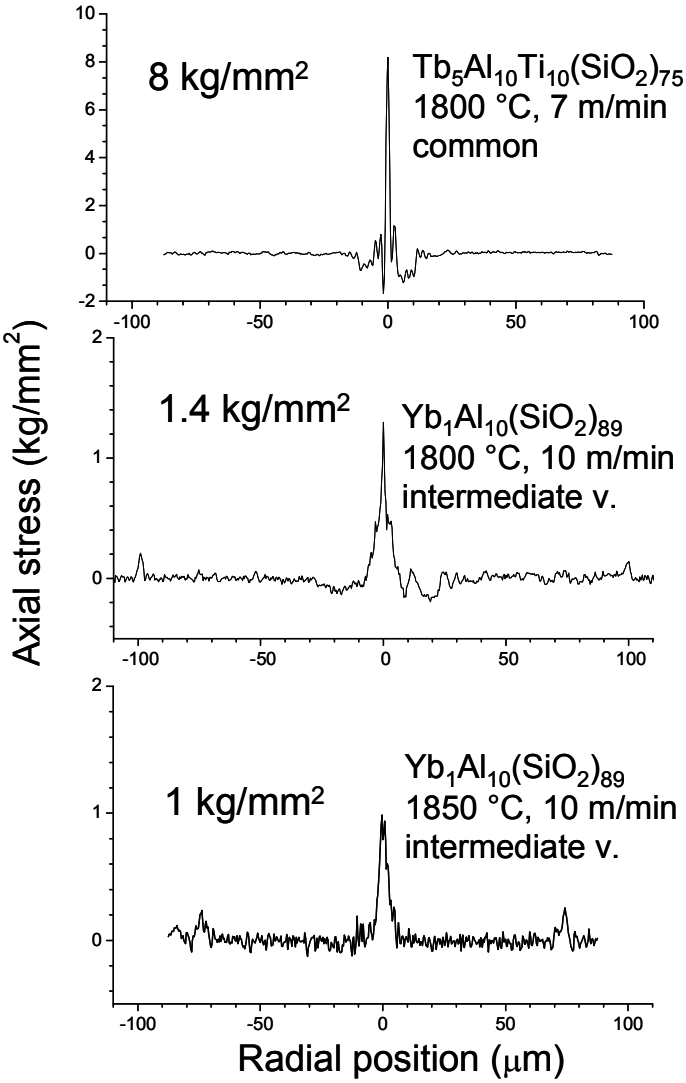

Figure 5.5 Stress profiles of a) Yb_1:Al_{10} -doped sol-gel fiber, drawn at (1800 ± 10) °C with 10 m/min drawing speed (drawing tension unavailable), b) Yb-doped sol-gel fiber, drawn at (1850 ± 10) °C with 10 m/min drawing speed (0.024 N drawing tension) and c) Tb-doped sol-gel fiber having a high content of titania (10 at.-%), drawn at (1800 ± 10) °C with 7 m/min drawing speed (drawing tension unavailable). The image shows a zoomed cutout around the fiber core.

For all sol-gel fibers, the stress in the cladding is within the detection limit. The stress in the core of the Yb-doped sol-gel fiber amounts to (1.29 ± 0.05) kg/mm^2, when drawn at 1800 °C, decreasing to (0.99 ± 0.07) kg/mm^2 if drawn at 1850 °C, both with 10 m/min drawing speed. The Tb-doped sol-gel fiber Tb_5:Al_{10}:Ti_{10} with its high titania content shows the highest core stress (8.2 ± 0.1) kg/mm^2. This fiber was drawn at 1800 °C with 7 m/min, the neodymium doped fiber Nd_1:Al_{10}:Ti_2 drawn at 1800 °C with 4 m/min, has (1.16 ± 0.05) kg/mm^2 core stress.

Figure 5.6 shows the 3-D-tomogram of the multi-mode Yb^{3+} fiber built from 12 stress profiles collected at angle steps of 30° over the cross section. The abscissa and the ordinate demote the position on the fiber cross section (μm), the colors represent the amount of stress (kg/mm^2).

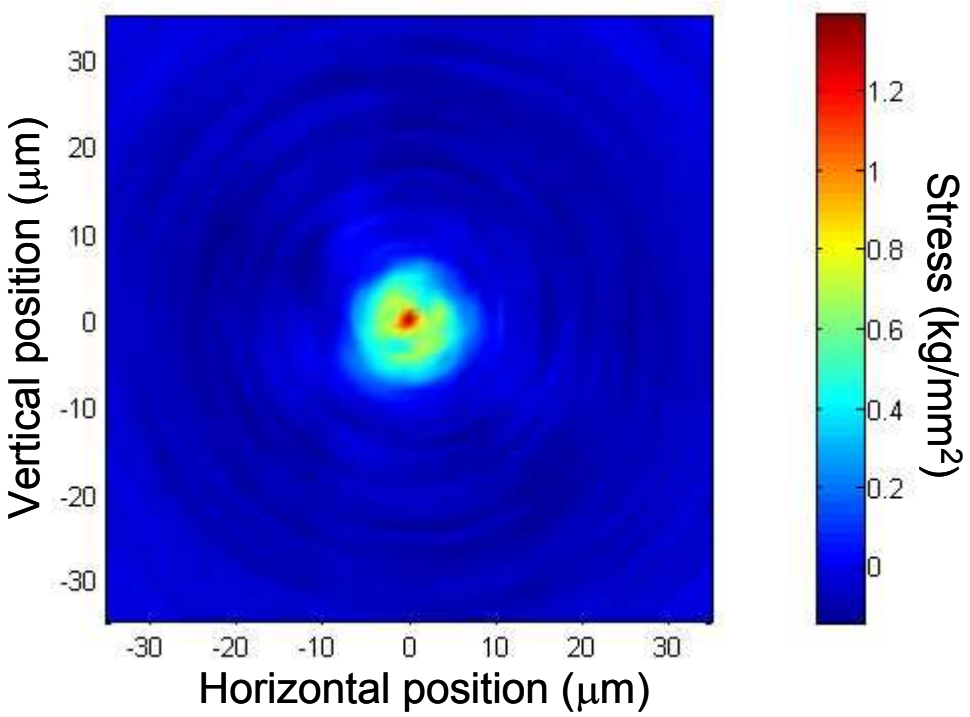

Figure 5.6 3-D-tomogram of the core region of an Yb_1:Al_{10} doped sol-gel silica glass fiber with 290 μm diameter.

The qualitative stress distribution looks the same for all investigated sol-gel fibers.

Discussion

Due to the small drawing tensions applied in this work, the stress in the cladding of all fibers is below the detection limit [91], in correspondence with theory since tension and speed are related linearly. The discussion therefore can concentrate on thermal stress contribution, which is the result of mismatches between thermal expansion coefficients.

A total of at least 11 at.-% dopants and co-dopants have been incorporated into the sol-gel silica matrix in this work. It is evident that this amount is responsible for a significant mismatch of the thermal expansion coefficient between core and cladding, leading to stress centered in

the core that is reduced with increasing temperature. Since the titania co-doped sol-gel fiber shows the highest stress, the thermal expansion coefficient $\alpha(r,T)$ at a radial position r and temperature T varies more in the titania co-doped fibers than in alumina co-doped fibers. Data for titania in silica was found in literature and shows linear behavior up to 9 % titania content. The experimental data indicate, that the change of the thermal expansion in case of titania as co-dopant in a sol-gel silica host must be stronger than with the co-dopant alumina.

The highest drawing temperature in this work is (1850 ± 10) °C. It is assumed that the homogenization of the microstructure is strongest at this temperature, similar to the mechanisms studied for sintering optical waveguides [92]. Subsequently losses are diminished by closing cracks, although this can not be seen with binocular microscopy or SEM. The stress in the core center should decrease since the mismatch in the thermal expansion coefficient inside the core decreases due to the more homogenized glassy network, and because the step-like change between core and cladding is flattened.

5.4 Spectroscopy

The absorption spectra of the $Yb_1Al_{10}(SiO_2)_{89}$ laser fibers were recorded at 974 nm on a multi-mode fiber preform slide (f-21), figure 5.7. The abscissa denotes the wavelength (nm), the ordinate the transmitted intensity (%).

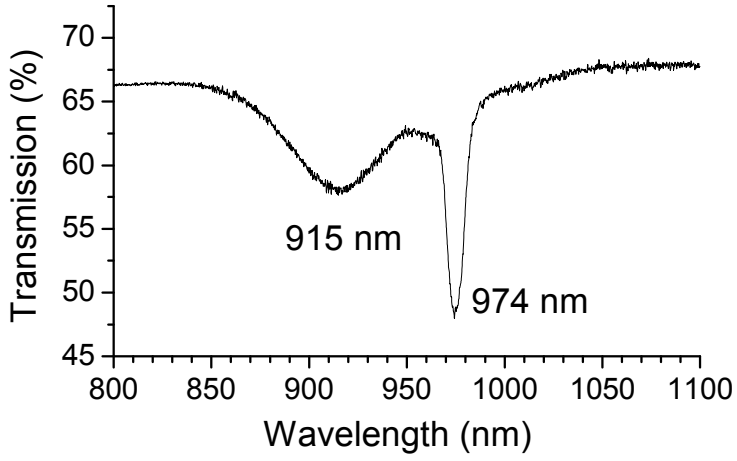

Figure 5.7 Absorption spectrum of the multi-mode laser fiber.

The absorption spectrum shows a behavior well known from literature [8]. The absorption bands of ytterbium in silica glass are at 939 nm and 974 nm [95]. The first absorption band is shifted to 915 nm in the Al^{3+} co-doped silica matrix by the Stark energy split characteristics of this host.

Fluorescence Spectra and Lifetime

Fig. 5.8 shows the fluorescence spectra of a 1 m long multi-mode laser fiber. The *x* co-ordinate shows the wavelength (nm), the *y* ordinate shows the different applied pump wavelengths (nm), and the *z* co-ordinate shows the fluorescence intensity (a.u.).

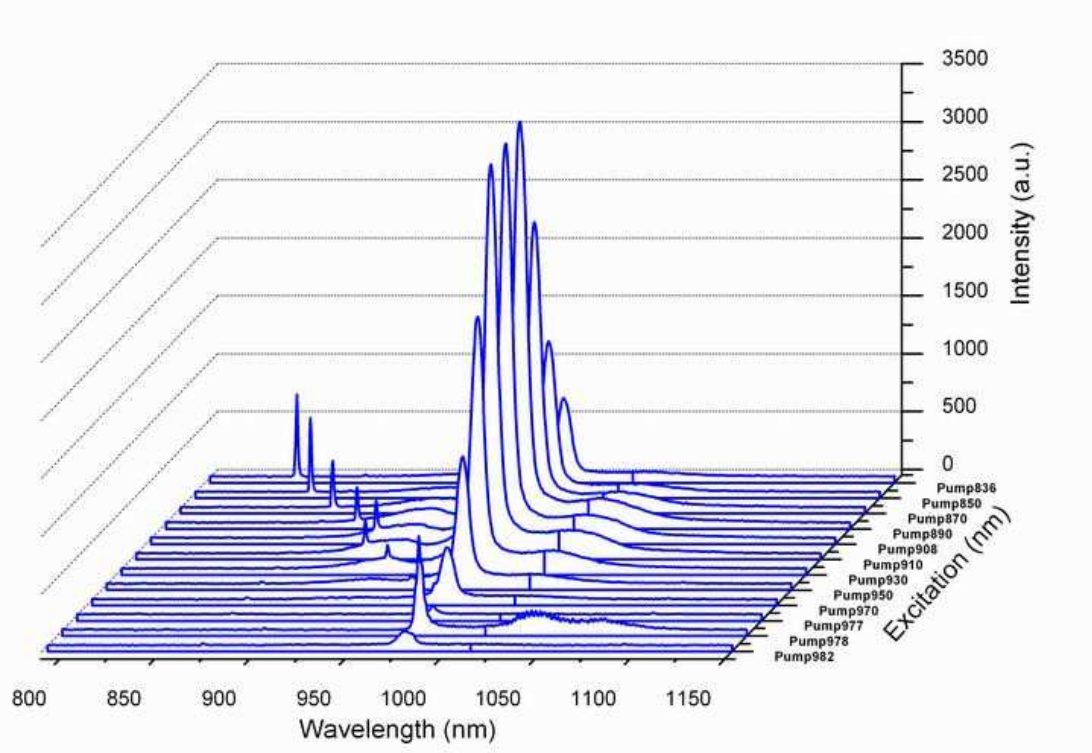

Figure 5.8 Fluorescence spectra.

The intensity ratio between the first fluorescence peak at 976 nm and the second peak at 1018 nm (16.6) stays constant for pump wavelengths between 890 nm and 910 nm. This ratio is least (4.9) for the pump wavelength of 978 nm. At this wavelength the second fluorescence maximum shifts to 1036 nm with a third maximum appearing at 1073 nm. The pump wavelength dependence of the emission behavior is a characteristic of alumina co-doped silica host

[6,20]. The different fluorescence maxima at different fiber lengths when pumped at 908 nm are listed in Tab. 5.5.

Table 5.5 Fluorescence lifetimes for different fiber lengths, pumped at 908 nm.

Fiber	Length (cm)	Fluorescence	
		spectra maxima (nm)	lifetime τ (µs)
$Yb_{17.2}Ti_{6.6}(SiO_2)_{76.2}$ (f-9)	4	976, 1035, 1068	805 ± 7
$Yb_1Al_{10}(SiO_2)_{89}$ (f-20 and f-21)	270	978, 1029, 1065	777 ± 16
	152	976, 1017, -	810 ± 30
	20	974, 1042, 1072	764 ± 4
	12	977, 1027, -	811 ± 24
	1	977, 1022, 1073 [(a)]	810 ± 7
		Mean value	794 ± 42

[(a)] Peak at 1073 nm only if pumped at 978 nm.

The deviation of the main emission peak between the different fibers lies within the relative accuracy ± 2 nm of the spectrometer. The value in literature is 975 nm [8,9]. Table 5.5 also lists the fluorescence lifetime recorded for a 4 cm long piece of f-9 (non-lasing fiber), a 20 cm long fiber piece f-20 (mono-mode laser) and for fiber f-21 (multi-mode laser). The latter fiber was investigated at different lengths, (270, 152, 12 and 1.0) cm. The fluorescence lifetime was recorded at least at 4 different chopper wheel excitation frequencies and wavelengths. With the setup the temporal resolution was measured to be < 3 µs. The numerical analysis of the fluorescence intensity decay curve was performed starting at least 30 µs after the end of excitation. The dynamic range was at least one decade.

Comparable measurement on a commercial 0.5 at.-% Yb-doped Ge-co-doped MCVD-built fiber resulted in (729 ± 17) µs. Values for Yb-doped MCVD-built fibers reported in the literature are in the range of 720 µs to 1350 µs [78]. The fluorescence lifetime of the sol-gel based ytterbium aluminum silica glass fiber is also within this range.

6 Laser

In Appendix G, *Laser Equations*, the interaction of matter with radiation, the laser rate equations, and the gain of a fiber laser are discussed in general. The transitions of Yb^{3+} and the performance of the first Yb^{3+} sol-gel fiber lasers are described in the following.

6.1 Ytterbium

Figure 6.1 shows the ground-state absorption spectrum and emission spectrum [8], and the energy level diagram of Yb^{3+} in silica. The abscissa denotes the wavelength (nm), the ordinate the cross section (10^{-24} m^2).

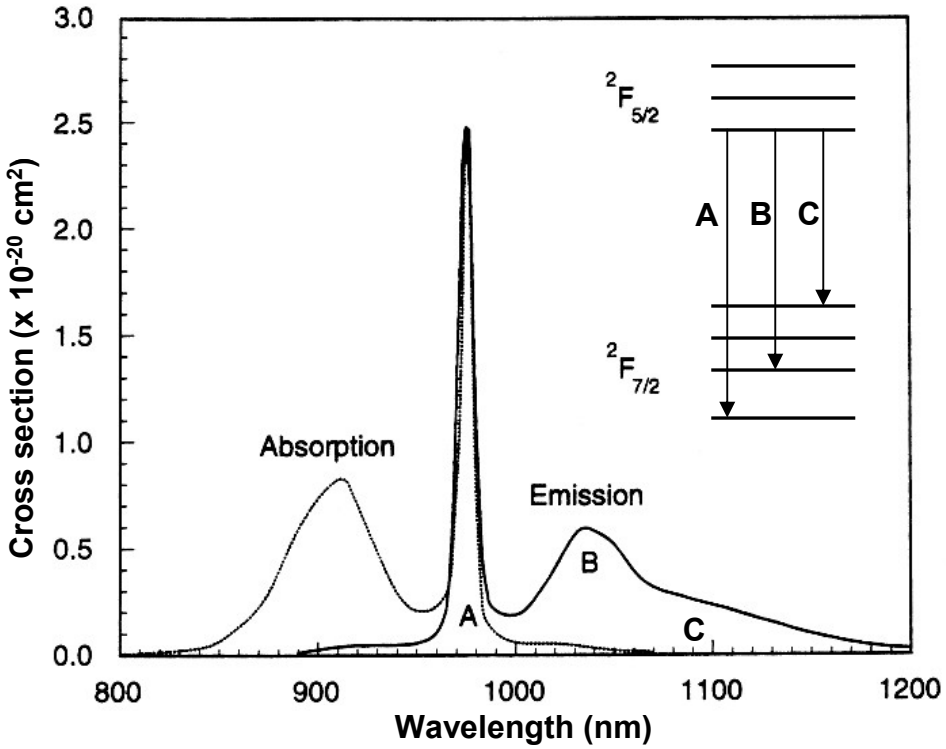

Figure 6.1 Ground-state absorption spectrum and emission spectrum [8], and energy level diagram, of Yb^{3+} in silica.

The specific characteristic of ytterbium is the simplicity of its energy scheme. It consists only of two states, the $^2F_{7/2}$ ground state and the $^2F_{5/2}$ excited state with the energy of approx.

10’000 cm^{-1}. The peak centered at 974 nm (transition A in Fig. 6.1) corresponds to a pure 3-level laser transition directly to the ground state and has a width of 10 nm full width half maximum (FWHM). The second peak centered at 1036 nm (transition B) has a width of 50 nm FWHM. The position of the transitions is independent of pump wavelength. Laser action on this transition is nearly 4-level in nature, in fact ytterbium has three- and quasi-four-level transition dynamics. The broad fluorescence spectrum of ytterbium allows emitting laser light within a wide range, 970 nm – 1200 nm, depending on fiber length. Longer fibers emit radiation at longer wavelength since the shorter wavelengths are reabsorbed due to the spectral overlap between the emission and absorption spectra, transition C.
Ytterbium transitions are inhomogeneously broadened in a silica glass matrix. The calculated stark splitting of the $^2F_{5/2}$ level of 0.25 wt.-% Yb^{3+} in 35 wt.-% aluminum co-doped silica glass amounts to 695.44 cm^{-1} [76,93]. The different ytterbium ions are surrounded by different local fields in the unordered amorphous silica glass host. Inhomogeneous broadening descends in the order of tellurite glasses, silicate, borate and phosphate glasses [94,95].
The damage of optical glasses is the extreme case of losses. Intensities up to 1.3 W/ μm^2 have been demonstrated in MCVD fiber lasers without damaging the waveguide. The surface damage threshold of optical glasses ranges from 50 W/μm^2 to 83 W/μm^2 and from 27 W/μm^2 to 83 W/μm^2 for colored glasses. The internal damage threshold, measured with 3 ns pulses, ranges from 23 W/μm^2 to 150 W/μm^2. It is typically higher, since surface defects also in case of polished surfaces favor local intensity peaks [96]. Damage thresholds for MCV deposited fibers usually are two magnitudes of orders lower. The possible maximal intensity of guided (laser) light in doped sol-gel silica glass is assumed to be significantly lower than the data above due to structural defects such as the radial shaped cross sections. The intensity of radiation in the fiber cores in this work was 4 orders of magnitudes beneath the mentioned damage limits.
When counter-propagating narrow-bandwidth light waves are superimposed, they form a standing-wave pattern. In a gain medium, this has two effects: the gain is saturated preferentially in the antinodes of the pattern, and the resulting amplification is dominated by the excitation density in the antinodes. This can lead to a deformation of the spectral shape of the gain, in particular to a gain saturation which is stronger for the wavelength of the saturated light field than for some other wavelengths. Consequences of this spatial hole burning for the operation of lasers are the difficulty to achieve single-frequency operation with standing-wave laser cavities and potentially reduced laser efficiency.

Table 6.1 lists the characteristics of representative continuous wave Yb-doped silica fiber lasers, listed in order of increasing laser wavelength.

Table 6.1 Characteristics of representative continuous wave Yb-doped silica fiber lasers, listed in order of increasing laser wavelength [9]

Laser Wavelength	Pump Wavelength	Ytterbium conc.	Fiber length	Other features	Threshold	Slope efficiency	Output power @ pump power	Ref
974 nm	900 nm	580 ppm	0.5 m	Dye laser pump	11.5 mW[(a)]	67%[(a)]	9.3 mW @ 25.3 mW[(a)]	[97]
980 nm	890 nm	$2x10^{20}$ Yb/cm^3	8.6 cm	Dye laser pump	15.8 mW[(1)]	66%[(1)]	10.6 mW @ 48.4 mW[(1)]	[98]
1019 nm	869 nm	0.11 wt% Yb	7 m	Ti : sapphire	14 mW [(i)]	41%[(i)]	215 mW @ 550 mW[(i)]	[99]
1040 nm	974 nm	500 ppm Yb	5 m	DCF/Ti:sapphire	75 mW[(i)]	70%[(i)]	470 mW @ 750 mW[(i)]	[100]
1047 nm	974 nm	1800 ppm Yb	10 cm	Single-frequency	<230 μW[(1)]	44%[(1)]	7.S mW @ 18 mW[(1)]	[101]
1065 nm	915 nm	-	-	DCF/LD bar	< 100mW[(1)]	54%[(1)]	16.4 W @ 32.5 W[(1)]	[102]
1084 nm	937 nm	(3-10)$x10^{19}$ Yb/cm^{-3}	20 m	Square inner clad	Approx. 0.4 W	72 % ± 3 %	4 W @ 7 W	[103]
~ 1090 nm	875 nm	~ 600 ppm Yb	-	DCF/LD pump	5 mW[(1)]	69%[(1)]	51 mW @ 80 mW[(1)]	[104]
1098 nm	850 nm	550 ppm Yb	90 m	Ti: sapphire pump	33 mW[(1)]	79%[(1)]	410 mW @ 550 mW[(1)]	[8]
1101 nm	915 nrn	-	-	DCF/LD bar	2.2 W[(1)]	52%[(1)]	20.4 W @ 32.5 W[(1)]	[102]
1102 nm	1047 nm	550 ppm Yb	90 m	Nd:YLF pump	30 mW[(1)]	90%[(1)]	520 mW @ 600 mW[(1)]	[8]
1114 nm	915 nm	1.5 wt% Yb	50 m	DCF/4 LD bars	0.6 mW[(i)]	~65%[(i)]	35.5 W @ 55.4 W[(i)]	[105]
1115 nm	1047 nm	700 ppm	100 m		610 mW[(i)]	28%[(i)]	660 mW @ ~3W[(i)]	[106]
1120 nm	915 nm	-	-	DCF14 LD bars	<22 W[(i)]	58.3%[(i)]	110 W @ 180 W[(i)]	[107]
1140 nm	1047 nm	550 ppm Yb	90 m	Nd:YLF pump	6 mW[(1)]	66%[(1)]	330 mW @ 500 mW[(1)]	[8]

[(i)] With respect to incident pump power; [(1)] with respect to launched pump power; [(a)] with respect to absorbed pump power, -: data not available; LD: laser diode; DCF: double-clad fiber.

6.2 Yb^{3+} Sol-Gel Fiber Lasers

The single-mode fiber (f-20, with 6.3 µm core and 140 µm cladding diameter) and the multi-mode fiber (f-21, with 10.4 µm core and 230 µm cladding diameter) both with a $Yb_1Al_{10}(SiO_2)_{89}$ core were investigated with different lengths on the setup shown in figure 5.1. Table 6.2 shows the laser performances.

Table 6.2 $Yb_1Al_{10}(SiO_2)_{89}$ fiber laser performances.

Fiber No.	Length (cm)	Performance			
		Threshold (mW)	Slope efficiency (%)	Ouput power (mW)	Wavelength (nm)
Mono-Mode (f-20)	20	-	-	-	1033 ± 2
	22	-	-	-	(1033, 1037, 1040, 1044) ± 2 [(a)]
	33.2	71 ± 13	27 ± 4	5 ± 1	7 lines within (1063 – 1091) ± 2 [(a)]
	65	47 ± 5	64 ± 3	3.9 ± 0.5	(1042, 1080, 1088) ± 2
Multi-mode (f-21)	40	32 ± 2	69 ± 4	44 ± 2	(1077 ± 2)
	100	72.5 ± 2.0	73 ± 5	34.2 ± 2.0	1096 ± 2
	152 [(b)]	90 ± 2	71 ± 4	27 ± 2	(1042, 1108) ± 2 [(c)]

(a) Depending on out coupling mirror adjustment.
(b) This fiber reached the recorded maximal output while pumped at 878 nm.
(c) 1042 nm with only Fresnel reflection at the out-coupling fiber end, 1108 nm with air gap between fiber end and out-coupling mirror.

With reabsorption longer fibers show higher thresholds. The behavior of the multi-mode fibers agrees well therewith. With the exception of the 1 m long multi-mode fiber laser (f-21) pumped at 878 nm for maximal output, all fibers reached best performance at 908 nm pump wavelength. Figure 6.2 shows the laser performance of the (1 m) long multi-mode fiber having the highest slope efficiency (73 %). The abscissa shows the launched pump power (mW), the ordinate shows the output power (mW).

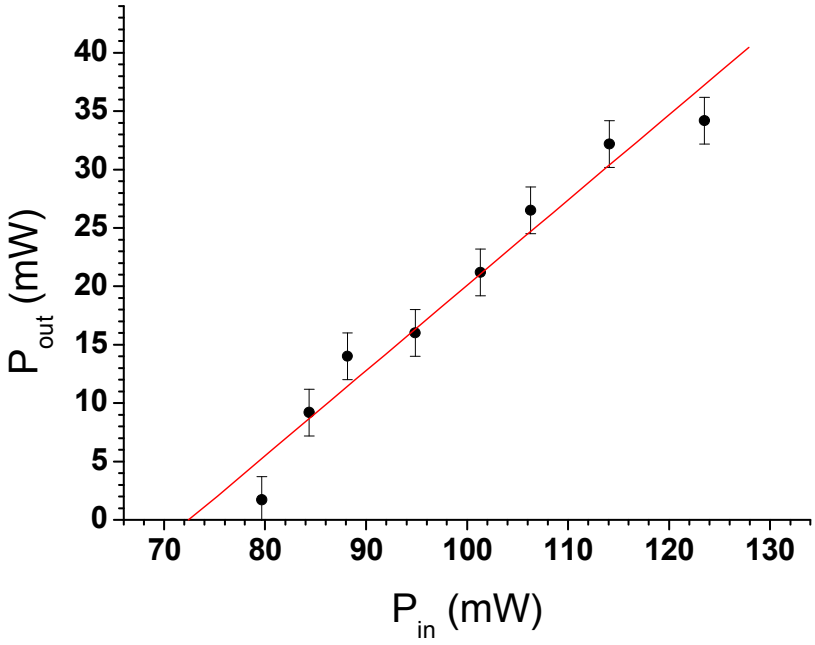

Figure 6.2 Laser performance: threshold 72.5 mW, slope efficiency 73 % (from linear regression), and maximal output (limited by available pump power) 34.2 mW.

The $Yb_1Al_{10}(SiO_2)_{89}$ fiber laser in this work is tunable from 1033 nm to 1108 nm depending on fiber length. The tunability was investigated with a resonator consisting of a mirror with R = 98.8 % at 1100 nm and 50 % at 908 nm, and different output couplers of R_1 = 4.8 %, R_2 = 16.2 %, and R_3 = 30 % respectively at 1100 nm Figure 6.3 shows the laser emission wavelength (nm) as a function of the fiber length (cm).

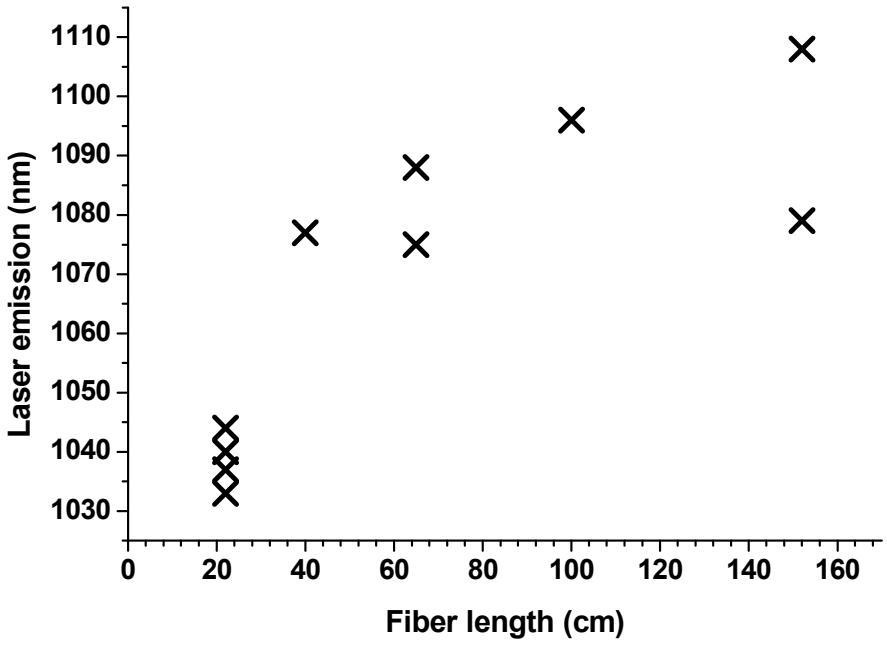

Figure 6.3 Laser emission depending on fiber length.

A clear trend towards longer laser wavelengths with higher fiber length can be ascertained, due to sidestepping the re-absorption. At the pump level available in this work, only the 152 cm long multi-mode fiber (f-21) showed laser action with Fresnel reflection at the cleaved fiber output end. Ytterbium fiber laser action is reported in literature usually with Fresnel reflection at the cleaved fiber ends only. In the 1 m long multi-mode fiber laser emitting at 1096 nm, the emission was constant for pump wavelengths between 835.5 nm and 982.0 nm. For varied pump power the emission wavelength was stable for all fibers. We assume that in the limited range of available pump power the expected blue shift is not yet visible.

Appendix

A Index of Refraction

Generally, the index of refraction of fibers depends on temperature, wavelength, thermal history, and tension. Here, we discuss the dependences upon wavelength and temperature more into detail.

In general the index of refraction can be calculated via the dispersion formula, Eq. (A.1),

$$n^2 - 1 = \frac{A_1\lambda^2}{\lambda^2 - B_1} + \frac{A_2\lambda^2}{\lambda^2 - B_2} + \frac{A_3\lambda^2}{\lambda^2 - B_3}, \tag{A.1}$$

with the Sellmeier coefficients A_1, A_2, A_3, B_1, B_2, and B_3 calculated with the method of least squares on the basis of the refractive indices at standard wavelengths or from literature, e.g. Landolt-Börnstein [82].
Furthermore the refractive index depends on the temperature of the media. There are two notation for the refractive index' coefficient of temperature, the absolute one, measured in vacuum, and the relative coefficient, measured at dry, ambient air with a pressure of 101.325 kPa, both linked via Eq. (A.2),

$$\frac{dn}{dT}_{absolute} = \frac{dn}{dT}_{relative} + n\frac{dn_{air}}{dT}. \tag{A.2}$$

B Fluorescence Lifetime of Small Nd^{3+} Doped Particles

Today's state of the art techniques to produce small particles and nanoparticles are laser ablation [108-111], the in-situ formation of native nanoparticles [112] such as e.g. sol-gel technology [113,114], solid state reactions [115], spray pyrolysis [116] or milling [117]. Also quantum dots (of cadmium sulfide) in thin glass films have been demonstrated with the sol-gel technique [118]. The modifications of spectroscopic properties of the nanoparticles need to be investigated [119]. Reported measurements of Nd-doped YAG polycrystalline cluster powders in air show lifetimes up to 510 ± 25 μs [120]. The fluorescence lifetime at a wavelength of 884 nm of heavily doped Nd:YAG nanoceramic grains with average diameters of 25 nm and 138 nm in air are reported [115]. Strongly non-exponential decay curves were observed due to efficient cross relaxation. The emission spectra of Nd:YAG sintered nanocrystalline laser ceramics show a broadening of emission lines [115,121-124]. These experimental results base on particles with diameters smaller than the wavelengths. Methods for embedding submicron particles into waveguides e.g. by the sol-gel technique are published for many systems [118,125-128].

The transition from macroscaled single crystals to submicron particles by milling increases not only the ratio of surface to bulk and thereby the influence of surrounding media onto the optically active ions, but also increases the number of disordered unit cells at the crystals surface. The first effect – increased ratio of surface to bulk – can quench fluorescence lifetimes by multi-phonon processes in the surrounding media, which is the more pronounced the higher the possibility of vibronic energy transfer to the surrounding media is [116,129,130]. From the point of view of classical solid state physics [131], the second effect – disordered surface unit cells – decreases phonon state densities in crystals by perturbed crystal lattices. As a result there are more structural defects such as atomic zero-dimensional misordering or two-dimensional defects like grain boundaries, and lattice imperfections which trap and dissipate energy (impurity quenching) [132]. OH groups e.g. of an organic solvent which is sufficiently wetting the submicron particles, can quench the fluorescence lifetime, representing the third mechanism. As fourth effect, the surrounding media changes the effective index of refraction [108,133], influencing the ${}^4F_{3/2} \rightarrow {}^4I_{11/2}$ transition in case of Nd^{3+}. Table B.1 shows the physical properties of commercial laser rods.

Table B.1 Physical properties of commercial $Nd_{0.03}:Y_{2.97}Al_5O_{12}$.

Physical property [a]	Value (unit)	Remarks
Relative molecular mass Mw	595.29 (g / mol)	For 1 at.-% Nd [b]
Poissons number ν_p	0.25 (1)	-
Luminescence lifetime τ_f [b]	230 – 255 (μs)	-
Youngs modulus *E*	3.17×10^4 (kg/mm^2) 311 (GPa)	-
Heat conductivity	14 ($Wm^{-1}K^{-1}$) 10.5 ($Wm^{-1}K^{-1}$)	at 20 °C at 100 °C
Thermal shock resistance	790 (Wm^{-1})	-
Lattice constant [c]	12.005 - 12.01 (Å)	Cubic
Relaxation time / energy @ 1064.1 nm of terminal lasing level	30 (ns) / 2110 (cm^{-1})	-
Linewidth	0.6 (nm)	-
Loss coefficient	0.003 (cm^{-1})	at λ = 1064 nm
$n_{1.0\ \mu m}$	1.8197 (1)	-
dn/dT	7.3×10^{-6} (K^{-1})	at unknown intervall of λ
Melting point	1950 (°C)	-
Density ρ	4.55 (g/ml)	-
Hardness on Mohs' scale	8 – 8.5 (1)	-

[a] Various information for this work were taken from [10,14,134].

[b] As indicated by the chemical formula $Nd_{0.03}:Y_{2.97}Al_5O_{12}$, YAG doped with 1 at.-% Nd was used in this work only.

[c] Value depending from source.

The investigation of fluorescence lifetime in Nd:YAG ($Nd_{0.03}:Y_{2.97}Al_5O_{12}$) nanoparticles as function of diameter and/or of the refractive index of the surrounding has not been addressed so far. Therefore the first goal was to investigate the dependence between fluorescence lifetime and particle diameter of Nd:YAG at ambient temperature. The second attempt was to repeat these measurements in liquid environment with different indices of refraction, smaller than YAG. Milled Nd:YAG powder was brought into 2-propanol, which serves simultaneously as organic dispersion medium and temperature stabilizer, and lowers the average index of refraction compared to the index of YAG. The prolonged radiation decay was measured in relation to particle size and constant refractive indices. The effects of temperature rise and heat conduction in nanocrystalline powders, totally different from macroscopic single crystals [124], were negligible in this work due to the liquid phase providing constant temperature during fluorescence lifetime investigations.

Using Stokes' law Eq. (B.1), the particle size distribution at the corresponding sedimentation height and sedimentation duration was calculated, after immersing the powders in liquid. The velocity v of a sinking particle with spherical shape is given by

$$v = \frac{2ga^2\left(\rho_p - \rho_s\right)}{9\eta}, \tag{B.1}$$

g is earth' gravity, a is the particle radius, ρ_s the density of solvent, ρ_p the density of particles, and η is the viscosity of the solvent. To compare the subsequently measured lifetimes with theory, three different methods reported in literature were considered. According to Meltzer and coworkers [135], the lifetime is enlarged proportional to

$$\frac{1}{\tau_f} \sim \left[\frac{n_{eff}^2 + 2}{3}\right]^2 \cdot n \ . \tag{B.2}$$

These authors expand the Lorentz virtual spherical cavity model with n_{eff}, the index of refraction between particle and surrounding depending on volume fractions. Yablonovitch and coworkers [136] change the lifetime in a real dielectric sphere by

$$\frac{1}{\tau_f} = \frac{1}{\tau_0}\left(\frac{3}{\frac{n_i^2}{n_e^2} + 2}\right)^2 \frac{n_e}{n_i}, \tag{B.3}$$

with the internal (n_i) and the external (n_e) index of refraction. Toptygin [137] uses the empty spherical cavity model

$$\frac{1}{\tau_f} = \frac{1}{\tau_0}\left(\frac{3n^2}{2n^2 + 1}\right)^2 n. \tag{B.4}$$

The latter formula can be derived by Eq. (B.3) by equaling n_i to unity. The first mentioned work differs from the two others but verifies its prediction also with experimental results. It is therefore assumed that there is still incertitude in how to describe numerically the effect of fluorescence lifetime prolongation.

The milling, the resulting particle size distribution, the results of the sedimentation and fluorescence lifetime investigation, and the results of the index variation and fluorescence lifetime investigation are presented in the following. To the end, possible alternatives to the conducted experiments are listed.

Milling

Subsequently high energy ZrO_2 ball milling of 1 at.-% Nd:YAG ($Nd_{0.03}:Y_{2.97}Al_5O_{12}$) was performed. As starting material, a Nd:YAG boule (FEE, Idar-Oberstein, Germany) was used. In Nd:YAG garnets, grown by the Czochralski method, the Nd-content varies along the growth axis due to segregation. The average at.-% Nd content in this work was 1%. The boule was pre-crushed manually with a hammer and a metal chisel in an aluminum vessel and 29.4 g of the pre-crushed particles subsequently milled with a planetary mill (pulverisette 7, Fritsch GmbH, Idar-Oberstein Germany). The milling was performed by the mill manufacturer and repeated at the IAP. 2-propanol with a purity of 99.9 wt.-% served as organic solvent for grinding. Table B.2 shows grinding set and parameters and 50% number of diameter d_{50}, for a detailed analysis of the grinding bowl and balls refer to table B.3.

Table B.2 Planetary mill grinding set and parameters.

Total grinding time (h)	Remarks [a]	Result [b] d_{50}
0.05	Pre-crushing, no solvent used ZrO_2 grinding bowl, 7 ZrO_2-balls / 15 mm diameter 800 rotations per minute	-
0.5	10 ml 2-propanol added [c]	< 3.5 μm
1	2 ml -2-propanol added [c]	< 2.6 μm
2	-	< 2.0 μm
3	2 ml 2-propanol added [c]	< 1.9 μm
5	5 ml 2-propanol added [c] Balls replaced by 20 ZrO_2-balls / 20 mm diameter	< 1.5 μm
10	-	< 1.0 μm

[a] Remarks denote deviations from the upper cells or additional setups.
[b] As measured by Fritsch GmbH (Idar-Oberstein, Germany) [138].
[c] Quality and source unknown, used by Fritsch GmbH (Idar-Oberstein, Germany).

Table B.3 Analysis of grinding set. [138]

Formula	Content [a] (%)
ZrO_2	94.50
HfO_2	1.5
SiO_2	< 0.1
Al_2O_3	< 0.1
Fe_2O_3	< 0.05
CaO	< 0.05
MgO	< 3.1 – 3.3
Na_2O	< 0.03
others	< 0.1

[a] Assumed as to be wt.-%.

Particle Size Distribution

The particle size class distribution was determined with a commercial laser particle sizer (analysette 22, Fritsch GmbH, Idar-Oberstein Germany) by the mill manufacturer and with dynamic light scattering (DLS) at the IAP. The two milling charges, the one from the mill manufacturer and the one milled at the IAP were investigated with SEM at the IAP. The data from the manufacturer of the size distribution is shown in Fig. B.1, where the abscissa denotes the particle size (μm) and the ordinate shows the occurrence and cumulative occurrence (both %). Fig. B.2 shows a SEM micrograph of the clustery powder.

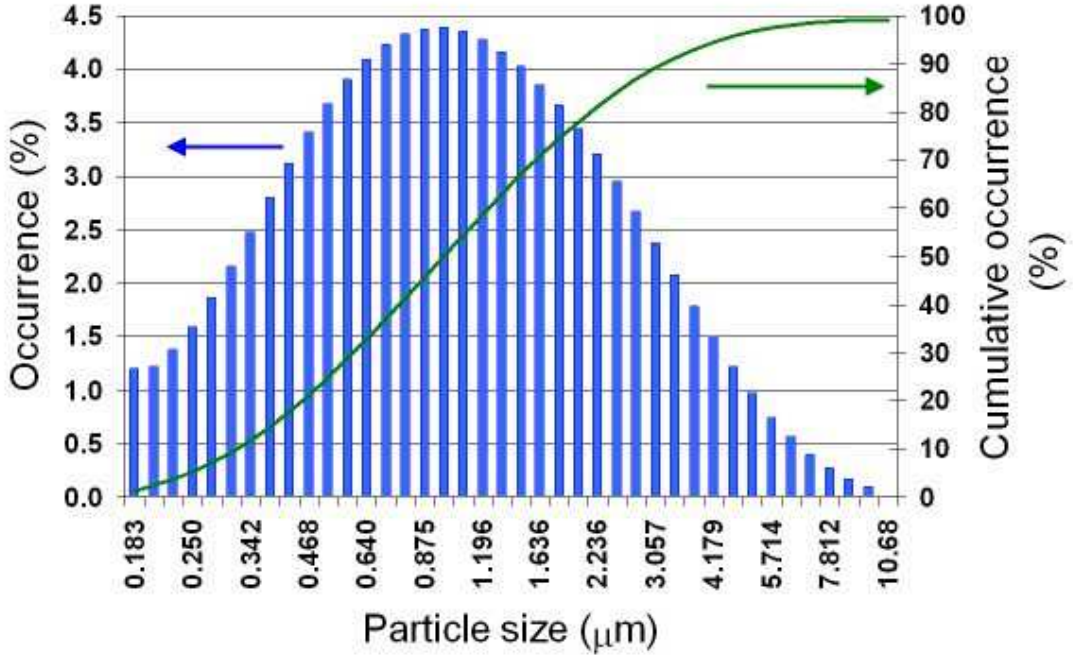

Figure B.1 Resulting distribution of particle diameter classes. The fraction of particles smaller than 174 nm in diameter was not determined.

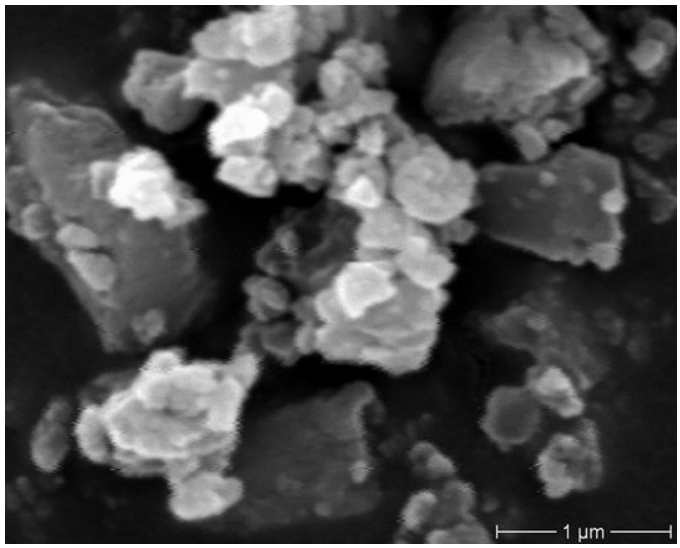

Figure B.2 SEM micrograph of the milled Nd:YAG powder showing clusters.

The powder shows many clusters. As observed by SEM ultrasound treatment shows no effect on this clustered system. The resulting powder consisted of 64.8 wt.-% Nd:YAG and 35.2 wt.-% ZrO_2 abrasive wear. The d_{50} of the entire powder was smaller than 1 µm. The fraction of ZrO_2 abrasive wear of the used mill shows particle sizes bigger than 1 µm, typically around 3 µm [138]. Thus the d_{50} of the Nd:YAG fraction was effectively smaller. Figure B.3 shows the taken XRD pattern using CuKα_1 with $\lambda = 0.15460$ nm and characterized with data from literature [139,140]. The abscissa shows the diffraction angle 2θ (°), the ordinate the diffraction intensity (a.u.).

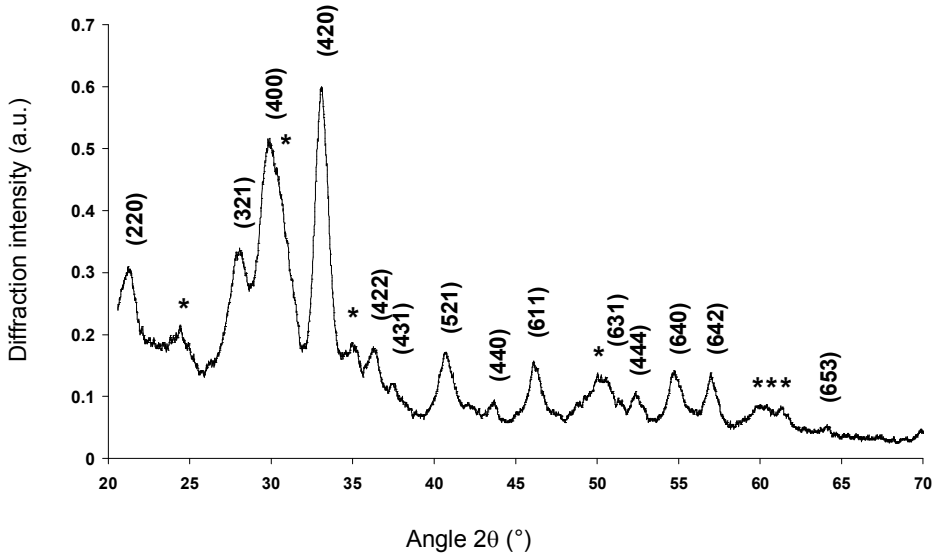

Figure B.3 XRD powder diffraction pattern. The asterisks mark reflexes from ZrO_2 mill wear.

The position of the reflexes of the milled powder is in accordance with the Nd:YAG pattern from literature. Some reflexes originating from ZrO_2 mill wear are visible.

Sedimentation and Fluorescence Lifetime Investigation

(2.00 ± 0.02) g milled powder was added to 30 ml 2-propanol (n^{25}_D = 1.377, > 99.9 wt.-%) in glass tubes. The glass tubes were brought to a vertical position for the sedimentation to start. Fluorescence lifetime measurements were done after different sedimentation durations at different sedimentation heights. Temperature was measured during all investigations. This method using sedimentation leads only to estimated values on the one hand due to unknown shape of particles, the polydisperse system with clusters, wear of ZrO_2 and a too high overall-particle-in-solvent volume fraction during sedimentation [141]. On the other hand, with the employed method of powder insertion the sedimentation results in the upper limit of the particle size distribution.

Pump light from a laser diode pulsed with a sharp falling edge (λ = 808.5 nm, 0.12 W average power at 200 Hz and 1 ms puls duration) was launched to the sedimentation glass tubes at different sedimentation heights. Emitted fluorescence was collected with a silica fiber bundle, and the fluorescence lifetime was detected using a cooled photomultiplier (7102, Hamamatsu Photonics Swiss Office Solothurn) and a digital storage oscilloscope (Textronix TDS 684A, Tektronix represented by Linktronix AG). A grating monochromator was set to 1064 nm, and an additional interference filter with a transmission of 0.089 % at 808 nm and 89.8 % at 1064 nm was used to minimize influence of pump light. The experimental setup is shown in Fig. B.4. The signal response lifetime was below 100 ns.

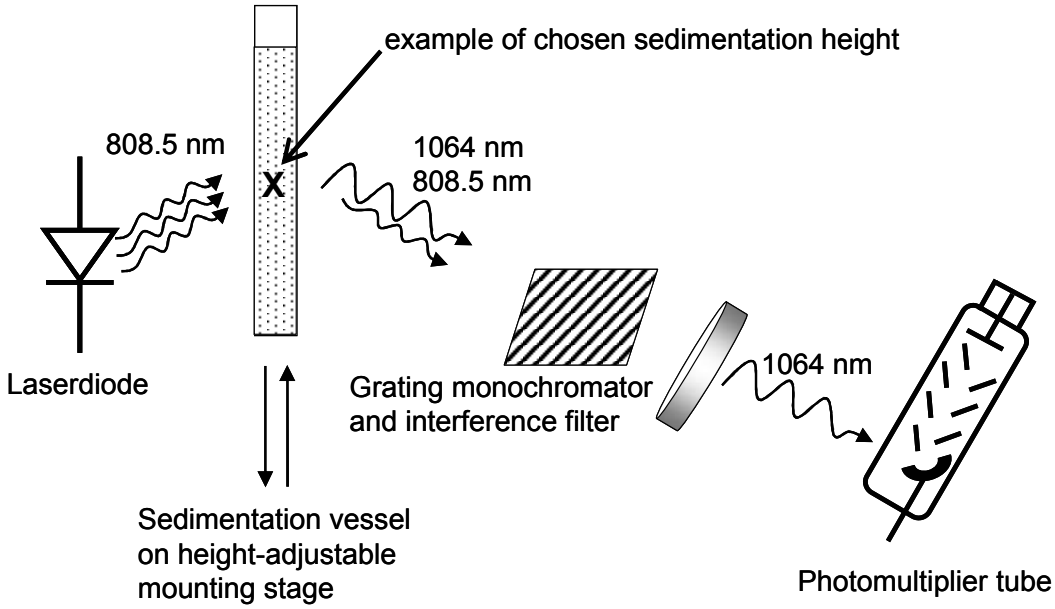

Figure B.4 Setup for sedimentation and fluorescence lifetime measurement.

Three different samples were investigated, s-1, s-2 and s-3, each was measured at least twice. The temperature during all measurements was (22 ± 1) °C. The fluorescence lifetimes versus particle sizes (function of sedimentation height and sedimentation duration) are listed in table B.4. A typical fluorescence decay is shown in figure B.5, with the abscissa as the time scale (ms), and the ordinate denoting the fluorescence intensity (a.u.). The decay was fitted for all measurements with a single exponential decay within one decade observed.

Table B.4 Particle size versus fluorescence lifetime for constant refractive indices.

Sample	Fitted τ_f (μs)	Particle size (nm)
s-1	314	709
	288	709
s-2	432	761
	288	761
s-3	309	992
	361	992
	238	992
Average value: 318 μs (± 62 μs)		

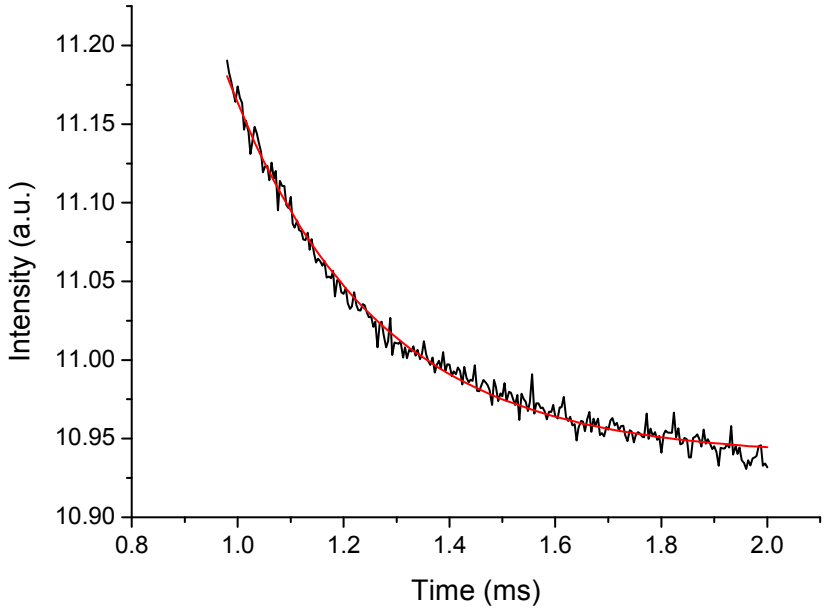

Figure B.5 Fluorescence decay.

The highest measured fluorescence lifetime for particles with diameters smaller than 1 µm amounts to 432 µs, measured for a fraction with calculated value of 761 nm as upper diameter limit. The average value of all measurements of the size class up to 1 µm is 318 µs. The decay has a standard deviation of ± 62 µs. The lowest measured fluorescence lifetime amounts to 238 µs for a diameter of 992 nm. The data in this work is a convolution of two distributions: on each height in the vessel the whole distribution of particle sizes from zero to the chosen upper size is present; the second distribution is the dependence of lifetime on particle size. As yet the available data do not allow a conclusion.

Index Variation and Fluorescence Lifetime Investigation

To vary the influence of the surrounding onto the local field via different index of refractions, varying phase fractions of the milled Nd:YAG powder was poured into three different organic solvent showing different indices of refraction. Well known organic compounds show indices from 1.283 for trifluoroacetic acid up to 1.749 for diiodomethane [142]. We chose 2-propanol (n^{25}_D = 1.377, > 99.9 wt.-%), 1-octanol (n^{25}_D = 1.429, puriss ≥ 99.5 wt.-%) and benzyl alcohol (n^{25}_D = 1.540, ≥ 99.0 wt.-%) due to their low toxicity and availability. The values for the indices of refraction for the different solvents were taken from the suppliers' material data sheets. Together with these new samples the first samples series (s-1, s-2 and s-3) were investigated

too, after one year of storing. All samples were investigated in the same setup as before just after setting up, and after 23 hours sedimentation time at a height corresponding numerically to 0.9 μm particle size. The corresponding nomenclature is *shaked* or *sedimented*. The results are listed in Table B.5.

Table B.5 Fluorescence lifetime in the three different refractive indices.

Sample and/ solvent	Code	Treatment	Fraction (wt.-%)	Lifetime (μs)
s-1, 2-propanol	s-1sed	sedimented	8	341 ± 29
	s-1shaked	shaked	8	243 ± 89
s-2, 2-propanol	s-2sed	sedimented	8	160 ± 14
	s-2shaked	shaked	8	341 ± 48
s-3, 2-propanol	s-3sed	sedimented	8	342 ± 73
	s-3shaked	shaked	8	381 ± 105
2-propanol	2-propanol.1	shaked	19	274 ± 111
	2-propanol.2	shaked	23	223 ± 46
	2-propanol.3	shaked	20	312 ± 61
1-octanol	1-octanol.1	shaked	22	227 ± 60
	1-octanol.2	shaked	22	248 ± 156
	1-octanol.3	shaked	25	406 ± 2
Benzyl alcohol	benzyl alcohol.1	shaked	16	370 ± 126
	benzyl alcohol.2	shaked	19	335 ± 107
	benzyl alcohol.3	shaked	20	324 ± 47
	benzyl alcohol sed	sedimented	20	257 ± 28

Figure B.6 shows a plot of the data in Tab. B.5. The ordinate shows the measured fluorescence lifetime (μs). The abscissa shows the index of refraction of the solvent. The plot shows the different theories. To simplify matters and to see the trend only, in Eq. (B.2 – Meltzer and coworkers), n_{eff} was set as to be index of refraction too, together with n. In Eq. (B.3 – Yablonovitch and coworkers) the internal index was set to be the index of YAG, whereas the external index was the one of the solvent. In Eq. (B.4 - Toptygin) n was the solvents index. For the experimental data the measured lifetimes are assigned to the index of the used solvent.

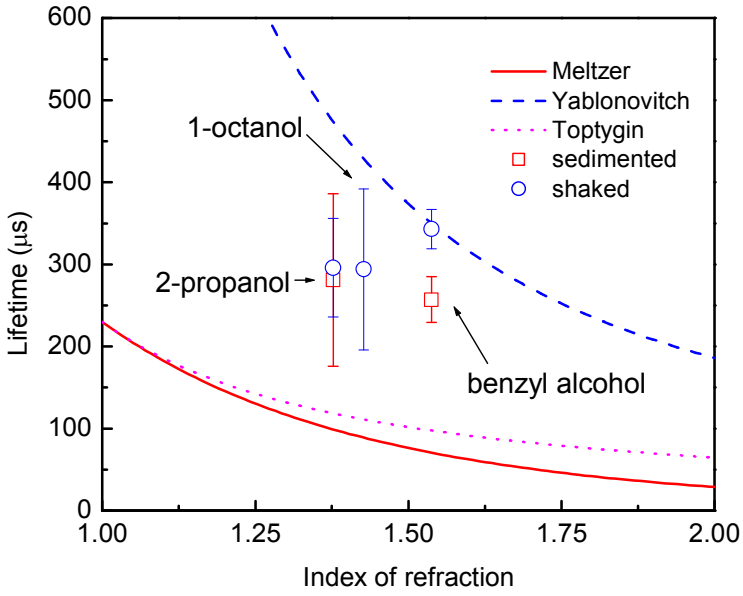

Figure B.6 Measured fluorescence lifetimes in different surroundings, compared to the theories from literature.

There exist significant discrepancies between the different theories, as it can be seen in Fig. B.6. The measurements are not attributable to any of the theories. The applied method of milling without controlled quantitative fractioning of the different particle size classes is unsuitable to investigate the dependence of fluorescence lifetime upon particle size. The clusters are more or less filled with the suspending liquid, depending on the liquid's viscosity and on the pore size of the clusters. The determination of the pore size/distribution was beyond the scope of this work. The dynamic viscosity values in contrast are available in literature, such as the viscosity at 20 °C η_{20} of 2-propanol is 2.256 x 10^{-3} (Nsm^{-2}), η_{15} of 1-octanol 10.6 x 10^{-3} (Nsm^{-2}) and η_{20} of benzyl alcohol 5.8 x 10^{-3} (Nsm^{-2}) [142]. Neglecting the wettability it can be said: in case of the liquid with the smallest viscosity, 2-propanol, more filled small pores define the refractive index of the local field most. In case of 1-octanol the pores are filled little, and benzyl alcohol penetrates the clusters more than 1-octanol but less than 2-propanol. Thus 2-propanol samples should show the longest lifetime, followed by benzyl alcohol and 1-octanol, in contradiction to the experimental result.

Alternatives

An alternative to investigate this powder with its wide particle size distribution and clusters is the quantitative fractioning. This idea was pursued twice. First 5 grams of the powder were bagged in a polyamid (nylon) precision sieve cloth with 15 μm mesh width (VWR International AG, Dietikon Switzerland) and dipped 500 times in stirred H_2O within 5 days. H_2O had to be taken since propanols are corroding nylon. The cloudy solvent was subsequently excited. No fluorescence was detectable, also after the solvent was concentrated with a rotary evaporator. As second attempt, a 1 m high and 5 centimetres wide tube was filled with 2-propanol and charged with a suspension of few grams milled powder in several millilitres 2-propanol. After sedimentation during one week, 10 cm high fractions of the cloudy solvent column were siphoned. The fractions were concentrated but fluorescence was not detectable.

Other possibilities are the addition of chemical additives avoiding quenching or the production of native nanoparticles, to obtain particles with diameter small enough, and in significant amounts. The production of native nanoparticles is described in various publications, e.g. [113,114,143], or patents [144,145], together with well investigated properties [121,122,146-150].

The present work is continued in the frame of a Swiss National Science Foundation project. CdSe quantum dots and native Nd:$NaYF_4$ nanoparticles produced by precipitation synthesis are incorporated in fiber core matrices.

C Photonic Crystal Fiber

First PCF were drawn in Bern within the frame of this work. The preform consisted entirely of Herasil-3 quartz. It was constituted by an encasing tube, (19 ± 0.5) mm outer diameter, (16 ± 0.5) mm inner diameter and length (80 ± 0.5) cm, equipped with six small tubes, (5 ± 0.5) mm outer diameter, (3 ± 0.5) mm inner diameter and length (75 ± 0.5) cm, and one quartz rod, (5 ± 0.5) mm diameter and length (75 ± 0.5) cm. The preform was drawn at normal pressure and 1750 °C oven temperature. Figure C shows the fiber.

Figure C Photonic crystal fiber. The diameter is 200 µm.

Eminent deformations of the initially circular cross sections have to be noticed. Not all of the different components are fused to each other. Since the rod after drawing has a relative greater radius than the other small tubes, we attribute all these irregularities to the low drawing temperature and speed applied. A temperature of 1750 °C is close to the setting temperature of quartz glass 1710 °C [14,72]. The temperature gradient leads to distinct lower temperatures in the innermost part. This causes totally inhomogeneous drawing conditions along the widespread cross section (19 mm) of the preform.

The development of PCF was continued in the frame of two PhD thesis at the IAP.

D Chemistry

The basic formulation for stable sols and the particulate instruction to achieve highly viscous sols are described in the following. The details of the chemicals employed in the sol-gel process are summarized in Table D.1.

Table D.1 Details of the employed chemicals.

Nomenclature	Source		Relevant properties	
	Name	Purity / Content	Relative molecular Mass [(a)] Mw	Density [(a)] $d\ ^{20}/_{4}$
Tetraethyl-orthosilicat, TEOS	Fluka [(b)]	puriss. ≥ 99.0 wt.-%	208.3 g/mol	0.933 g/ml
Titan(IV)-isopropoxid, TIP	Fluka	purum	284.2 g/mol	0.96 g/ml
Ethanol	Merck [(c)]	absolut zur Analyse	46.07 g/mol	0.79 g/ml
Water	IAP [(d)]	Milli-Q	18.02 g/mol	1.00 g/ml
Hydrochloric acid HCl aq.	Fluka	puriss p.a. ≥ 36.5 wt.-%	36.46 g/mol	1.18 g/ml
Aluminum nitrate nonahydrate	Fluka	puriss p.a. ≥ 98.0 wt.-%	375.13 g/mol	(solid)
Ytterbium nitrate pentahydrate	Aldrich [(e)]	99.9 wt.-%	449.13 g/mol	(solid)

(a) according to Falbe [14].
(b) Fluka Chemie GmbH Buchs, Switzerland.
(c) Merck (Schweiz) AG Chemicals Dietikon, Switzerland.
(d) Milli-Q of Millipore.com, installed at the Institute of Applied Physics, University of Bern, Switzerland.
(e) Fluka Chemie GmbH Buchs, Switzerland on behalf of Aldrich of Sigma-Aldrich Corporation.

Basic Formulation

1 mol TEOS was dissolved in 8 mol EtOH and stirred for 5 minutes. Ethanol as a polar (and protic) solvent was ideal since it dissolves easily inorganic nitrates. 22 ml of HCl aq. with a diluted normality of 0.15 N (corresponding to 3 mmol HCl and 1.234 mol H_2O) was added while stirring vigorously, resulting in a clear colorless, lightly warmed (35 °C) solution. The final mixture showed a concentration of approx. 1.4 N SiO_2 after two hours stirring at ambient temperature. If titanium was the desired co-dopant, 1 mol TIP was dissolved in 7.5 mol EtOH to obtain a clear very lightly yellow, lightly warmed (35 °C) solution. This solution showed a

normality of approx. 1.4 N at ambient temperature after two hours stirring. If aluminum was the desired co-dopant, 1 mol aluminum nitrate nonahydrate was dissolved in 27.6 mol EtOH by two hours stirring to obtain a clear colorless solution, showing approx. 0.51 N at ambient temperature. 1 mol ytterbium nitrate pentahydrate was dissolved in 16.7 mol EtOH (approx. 0.86 N). The corresponding amount of the co-dopant solution of titania or aluminum nitrate was slowly poured into the TEOS-solution while stirring vigorously. In case of TIP the mixtures became thereby lightly yellow and approx. 35 °C to 40 °C warm. Finally, the desired amount of ytterbium (between 1 at.-% and 20 at.-%) was added. The final sol was stirred for at least 2 hours and stored for 48 hours before use. All these preparations were conducted in sealable low density polyethylene vessels. None of the sols showed gelation within one month, thus no gelation inhibitor such as acetylacetone [151] was therefore required. 30 of 50 sols with similar composition were long-term stored at the same conditions, e.g. ambient temperature. 97 % of these sols (29) were still liquid after (6 ± 1) months, 90 % (27) after (9 ± 1) months and only 37 % (11) appeared as gels after (12 ± 1) months storage time. The reasons for inconsistent gelling times are compositions which were not exactly the same and variations of the unknown impurities in the fine chemicals, as shown by analysis certificates (e.g. [152]). Some ions can act catalytically in a sol-gel system, e.g. the ions of chromium, molybdenum, tungsten or fluorine [17].

Particular Formulations for Highly Viscous Sols

For the core deposition in the fiber preform tubes, the amount of solvent (EtOH in all cases) in the basic formulation was stepwise minimized down to 77.5 wt.-%. Three fiber preforms have thereby been produced (Table D.2). The most concentrated sols, used for the laser fibers f-20 and f-21, consisted of 1.26 mol TEOS, 0.14 mol aluminum nitrate nonahydrate, 15 mmol ytterbium nitrate pentahydrate, 4 mmol HCl in 1.556 mol H_2O, and 11 mol EtOH.

Table D.2 Produced fiber preforms.

IAP code [(a)]	Composition	Preform description	Layers	
			No.	Thickness (µm) [(b)]
f-9	$Yb_{20}Ti_{6.4}(SiO_2)_{73.6}$	Non-lasing fiber	6	1.4 ± 0.2
f-20	$Yb_1Al_{10}(SiO_2)_{89}$	Mono-mode fiber laser	3	2.7 ± 0.1
f-21	$Yb_1Al_{10}(SiO_2)_{89}$	Multi-mode fiber laser	6	2.7 ± 0.1

(a) Code used in the Laser Division of the Institute of Applied Physics (IAP), University of Bern, Switzerland.

(b) As measured by profilometry on f-21 and assigned to f-9 and f-21 by microscopical comparison of the preform slides.

E Stress Determination

Axially Symmetric Stress Distribution

When an optical ray passes through an anisotropic medium, its polarization is generally changed. The two components of the (transverse) electric field propagate with different velocities, as they experience different refractive indices *n(t,s)*, Fig. E.

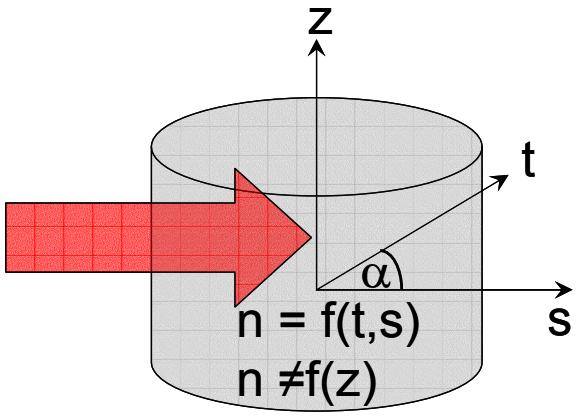

Figure E Optical ray passing trough anisotropic medium.

Due to the circular shape of the index variations in case of a symmetric stress distribution, the two components of the light vector then accumulate a total phase retardation profile $\delta^{tot}(t)$, only as function of t. For one-dimensional tomography of circular symmetric fibers the Abel-inversion was used in this work to recover the radial fields from the projection data [85]. The application of the Abel-transform to the phase retardation profile yields

$$\sigma_{zz} + \frac{E}{1-\nu}\Delta\varepsilon = -\frac{1}{\pi C}\int_r^R \frac{d\delta^{tot}/dt}{\sqrt{t^2 - r^2}}\,dt = \tilde{\sigma}_{zz}^{tot} = \sigma_{zz}^{el} + \tilde{\sigma}_{zz}^{in}\,, \qquad \text{(E.1)}$$

with the axial stress σ_{zz}, Young's modulus E, Poisson's ratio ν, and the photoelastic constant, C. The Abel-inversion of the total retardation profile is the sum of the elastic stress profile and a constant offset proportional to the inelastic strain. The offset has been labeled by the oxymoron "inelastic stress" by Paek et al. [87]. With this interpretation the Abel-transform can be taken as the superposition of a real "elastic" stress and a virtual "inelastic" stress with the "inelastic" stress defined as

$$\tilde{\sigma}_{zz}^{in} = \frac{E}{1-\nu}\Delta\varepsilon\,. \qquad \text{(E.2)}$$

The tildes in equations (E.1) and (E.2) indicate that the stress is only virtual, in analogy to the meaning of the quotation marks in the text. The integral of the axial stress, the real, elastic contribution in Eq. (E.1), vanishes over the fibers area, i.e.

$$\int_A \sigma_{zz}^{el} dA = 0\,, \tag{E.3}$$

according to St Venant's principle [153] which only holds for the elastic contribution. Therefore the virtual "inelastic stress" can be determined with the expression

$$\tilde{\sigma}_{zz}^{in} = \frac{\int_A \tilde{\sigma}_{zz}^{tot} dA}{\int_A dA}\,, \tag{E.4}$$

for the virtual "inelastic stress". The corresponding ("real") inelastic strain anisotropy can subsequently be deduced from equation (E.2). Once the profile has been separated from the virtual "inelastic stress", it can be inserted in the "sum rule", which connects the stress components for the case of circular symmetry [85],

$$\sigma_{zz} = \sigma_{rr} + \sigma_{\theta\theta}\,. \tag{E.5}$$

The sum rule applies only to cylinders where Young's modulus and Poisson's ratio do not depend on position. The stress components in the cylindrical coordinates are

$$\begin{aligned}
\sigma_{rr} &= \frac{1}{r}\frac{\partial F}{\partial r} + \frac{1}{r^2}\frac{\partial^2 F}{\partial \theta^2}\,,\\
\sigma_{\theta\theta} &= \frac{\partial^2 F}{\partial r^2}\,,\\
\sigma_{r\theta} &= \frac{1}{r^2}\frac{\partial F}{\partial \theta} - \frac{1}{r}\frac{\partial^2 F}{\partial r \partial \theta}\,,
\end{aligned} \tag{E.6}$$

with the Airy stress function $F(r,\theta)$ [85,154], and together lead to the equation of equilibrium when circular symmetry is assumed

$$\sigma_{\theta\theta} = \sigma_{rr} + r\frac{\partial \sigma_{rr}}{\partial r}\,. \tag{E.7}$$

Inserting the sum rule, equation (E.5), yields a differential equation which can be solved for the radial stress,

$$\sigma_{rr}(r) = \frac{1}{r^2}\int_0^r \sigma_{zz}(\rho)\rho d\rho \,. \qquad \text{(E.8)}$$

Clearly σ_{rr} must vanish outside the fiber, which is only guaranteed when the integral of the axial stress over the fiber areas vanishes (St Venant's principle). The further procedure is outlined below. A detailed discussion of the three inversions to perform one-dimensional tomography, Abel, onion-peeling and filtered backprojection methods, can be found in the literature [85,155].

Non-Axially Symmetric Stress Distribution

For a fiber with non-axially symmetric stress distribution, the two-dimensional (2-D) cross-secional stress profile can be determined from not just one but many projected phase profiles with different projection angels from - 90° to + 90°, Fig. E. The projected phase retardation profile for a certain projection angle α can be written as a line integral [86],

$$\delta_\alpha(t) = (2\pi/\lambda)\cdot\int\left[n_z(t,s) - n_t(t,s)\right]ds \,, \qquad \text{(E.9)}$$

where s is the propagation direction of collimated incoming light that is perpendicular to the fiber axis z, t is another transverse axis that is perpendicular to the z and s axis, λ is the wavelength of the light source, in our case amounting to 632.8 nm (incoherent collimated HeNe laser radiation), and $n_z\,(t,s)$ and $n_t\,(t,s)$ are the 2-D RIP of the two electric fields polarized along axial direction z and transverse direction t of the fiber. These phase retardation profiles with many different projection angles form a 2-D projected phase retardation profile $\delta\,(t,\alpha)$, called a sonogram [85].
The sinogram is used to calculate the 2-D axial stress distribution $\sigma_{zz}\,(x,y)$ of a fiber by use of the inverse Radon transformation [156,157]:

$$\sigma_{zz}(x,y) = \lambda/(2\pi C)\cdot iradon\{\delta(t,\alpha)\}, \qquad \text{(E.10)}$$

with *iradon{}* representing the inverse Radon transformation. The actual reconstruction of cross sectional stress data is obtained by use of a filtered backprojection algorithm as explained by Kak et. al. [156] and Abe and coworkers [157]. For the present work it was performed at the APL by the inverse Radon-transform implementation IRADON of the computer algebra environment MATLAB[F].

[F] http://www.mathworks.com/products/matlab/

Assuming that the parameters of a fiber do not change as a function of axial position z, the other nonzero stress tensor components in the circular cylindrical coordinate system ($\sigma_{\rho\rho}$, $\sigma_{\varphi\varphi}$, $\sigma_{\rho\varphi}$) are calculated by use of the Airy stress function $F(r,\theta)$

$$\frac{\partial^2 F}{\partial r^2}+\frac{1}{r}\frac{\partial F}{\partial r}+\frac{1}{r^2}\frac{\partial^2 F}{\partial \theta^2}=\sigma_{zz}-\chi, \tag{E.11}$$

where χ is an arbitrary harmonic function that satisfies $\nabla^2\chi=0$ for the case of circular symmetry, similar to the derivation above. The stress function is submitted to the boundary conditions

$$F(r,\theta)\big|_{r=a}=0, \quad \frac{\partial}{\partial r}F(r,\theta)\big|_{r=a}=0, \tag{E.12}$$

with the outer radius a of the cylinder. With the stress components in the cylindrical coordinates, equation (E.6), Since the fiber-stress distribution is not axisymmetric, the shear stress $\sigma_{r\theta}$, becomes nonzero and the stress tensor constructed with the generated components is not diagonal, but it was diagonal in the case of axially symmetric stress distribution. The stress tensor σ can finally be written as

$$\sigma=\begin{bmatrix}\sigma_{rr} & \sigma_{r\theta} & 0\\ \sigma_{r\theta} & \sigma_{\theta\theta} & 0\\ 0 & 0 & \sigma_{zz}\end{bmatrix}. \tag{E.13}$$

For a more detailed derivation of the mechanical theory see the APL works [85,158] and Puro and Kell [154].

F Bleaching

When pumping active media, both absorption and induced emission occur. The occupation N in the higher (2) and the ground state (1) is given by

$$\begin{aligned} \frac{dN_2}{dt} &= B_{12}\rho N_1 - B_{21}\rho N_2 \\ \frac{dN_1}{dt} &= -B_{12}\rho N_1 + B_{21}\rho N_2 \end{aligned}, \tag{F.1}$$

with B_{12} and B_{12} the Einstein[F] coefficients for absorption and induced emission respectively and the energy density $\rho(\omega)$. In a stationary equilibrium the total dynamics are given with $g_1B_{12}=g_2B_{21}$, with the degeneracies g_1 and g_2. The idealized linewidth is

$$\frac{d\Delta N}{dt} = -B_{21}\rho(N_2 - N_1) - B_{21}\rho(N_2 - N_1) = -2B_{21}\rho(\Delta N), \tag{F.2}$$

with $\Delta N(0) = -N_0$ (the thermal population is neglected) and $\rho(0) = \rho_0$ as boundary conditions. A solution for $\Delta N(t)$ is

$$\Delta N(t) = -N_0(N_0 h\nu - 2\rho_0)\frac{e^{tB_{21}(N_0 h\nu - 2\rho_0)}}{N_0 h\nu e^{tB_{21}(N_0 h\nu - 2\rho_0)} - 2\rho_0}, \tag{F.3}$$

and a solution for $\rho(t)$

$$\rho(t) = \frac{\rho_0(N_0 h\nu - 2\rho_0)}{N_0 h\nu e^{tB_{21}(N_0 h\nu - 2\rho_0)} - 2\rho_0}. \tag{F.4}$$

The limes for this set of differential equations is (stationary case),

$$\lim_{t\to\infty}\Delta N(t) = 0; -(N_0 h\nu - 2\rho_0) = -N_0 h\nu + 2\rho_0 = 0, \tag{F.5}$$

[F] Hundred years ago 1905 in Bern, Swiss citizen Albert Einstein explained among the many revolutions within his annus mirabilis the photoelectric effect [160] with a mathematical description with quanta of lights.

and for $\rho(t)$

$$\begin{aligned}\lim_{t\to\infty}\rho(t) &= -\frac{N_0 h\nu - 2\rho_0}{2} = \rho_0 - \frac{N_0 h}{2} \quad if \quad N_0 h\nu - 2\rho_0 < 0 \\ \lim_{t\to\infty}\rho(t) &= -\frac{N_0 h\nu - 2\rho_0}{2} = 0 \quad if \quad N_0 h\nu - 2\rho_0 > 0\end{aligned} \quad . \tag{F.6}$$

The lengthwise dependency now is given by

$$\begin{aligned}\frac{d}{dt} &= \frac{d}{dz}\frac{dz}{dt} = c\frac{d}{dz} \\ \frac{d\Delta N}{dz} &= -\frac{2B_{21}}{c}\rho\Delta N \\ \frac{d\rho}{dz} &= \frac{h\nu B_{21}}{c}\rho\Delta N\end{aligned} , \tag{F.7}$$

with the solution as before for

$$\rho(z) = \frac{\rho_0(N_0 h\nu - 2\rho_0)}{N_0 h\nu e^{z\frac{B_{21}}{c}(N_0 h\nu - 2\rho_0)} - 2\rho_0} . \tag{F.8}$$

The part of an incident pump beam that is above a certain energy density $\rho(z)$ sees the gain medium in the fiber core as to be transparent, that is to say that the number of absorbing ions equals the number of emitting ions. This derivation is correct only when stimulated processes are predominant. [159]

To incorporate spontaneous emission, the derivation has to start with the modified Eq. (F.1)

$$\begin{aligned}\frac{dN_2}{dt} &= B_{12}\rho N_1 - B_{21}\rho N_2 - \frac{N_2}{\tau_f} \\ \frac{dN_1}{dt} &= -B_{12}\rho N_1 + B_{21}\rho N_2 + \frac{N_2}{\tau_f}\end{aligned} , \tag{F.9}$$

with the fluorescence lifetime τ_f.

G Laser Equations

Interaction of Matter with Radiation

The Einstein coefficient A_{21} describes the probability of the transition of an electron in an atom from an upper energy level E_2 to the lower level E_1. The electron thereby emits a phonon of the frequency

$$\omega_{21} = \frac{E_2 - E_1}{\hbar}, \tag{G.1}$$

where $\hbar$ is the reduced Planck constant. The photon will generally be emitted in random direction with a random polarization (if external fields are absent). When considering an ensemble of atoms, the number of excited atoms is decreased according to

$$\frac{dN_2}{dt} = -N_2 A_{21}, \tag{G.2}$$

with the solution $N_2(t) = N_{2o} \exp(-A_{21}t)$.

Real systems are formed by many energy levels a, b, … so that Eq. (G.2) is modified to

$$\frac{dN_2}{dt} = -N_2 A_{21} - N_2 A_{2a} - N_2 A_{2b} - ... = -N_2 \sum_j A_{2j}\,. \tag{G.3}$$

The time within the number of excited atoms decreased to $1/e$ is called lifetime τ_2, with

$$\frac{1}{\tau_2} = \sum_j A_{2j} = \sum_j \frac{1}{\tau_{2j}}\,. \tag{G.4}$$

The spectral shape $g(\omega)$ of the spontaneous emitted radiation is called line shape, usually scaled

$$\int g(\omega)\, d\omega = 1\,. \tag{G.5}$$

Generally $g(\omega)$ shows a maximum at the frequency ω_{21} and has a finite width, the linewidth, leading to

$$A_{21}(\omega) = A_{21} g(\omega), \tag{G.6}$$

and

$$\frac{dN_2}{dt} = -N_2 \int A_{21}(\omega) d\omega = -N_2 A_{21}. \tag{G.7}$$

Electrons can be stimulated by incident photons to drop from the upper to the lower level. This mechanism is the so called stimulated emission. The thereby additionally emitted photon has exactly the same properties as the incident photon. The frequency dependency of the Einstein coefficient for stimulated emission is again determined by the line shape of the transition

$$B_{21}(\omega) = B_{21} g(\omega). \tag{G.8}$$

The dependency between the Einstein coefficient and the so called cross section for stimulated emission is

$$B_{21}(\omega) = \frac{c_0}{\hbar\omega} \sigma_{21}(\omega), \tag{G.9}$$

with c_0 the speed of light, 299 792 458 m/s in vacuum. The temporal change of the number of atoms in the higher state now is not only proportional to the number of atoms in the higher state, but also proportional to the number of incident photons, thus the radiant energy density $\rho(\omega)$

$$\frac{dN_2}{dt} = -N_2 \int B_{21}(\omega)\, \rho(\omega)\, d\omega = -N_2 B_{21} \int g(\omega)\, \rho(\omega)\, d\omega. \tag{G.10}$$

In case of a monochromatic radiation field $\rho(\omega) = \rho_0 \delta(\omega - \omega_0)$ and thereby

$$\frac{dN_2}{dt} = -N_2 B_{21} \int g(\omega)\, \rho_0 \delta(\omega - \omega_0)\, d\omega = -N_2 B_{21} g(\omega_0)\, \rho_0. \tag{G.11}$$

Analogous the number of atoms in case of stimulated absorption is given by

$$\frac{dN_1}{dt} = -N_1 B_{12} \int g(\omega)\, \rho(\omega)\, d\omega, \tag{G.12}$$

Without pumping the optically active system externally, the thermal occupation in the upper level at the temperature T is described by the Maxwell-Boltzmann statistics

$$\frac{N_2}{N_1} = e^{-\frac{\Delta E}{k_B T}}. \tag{G.13}$$

with the Boltzmann constant k_B. In fact, all atoms at thermal equilibrium virtually are in the ground level, since $N_2/N_1 \approx \exp(-90)$ in case of ytterbium. The relation between the two Einstein coefficients A and B is

$$g_1 B_{12} = g_2 B_{21}, \tag{G.14}$$

with the degeneracies g_1 and g_2, and

$$A_{21} = B_{21} \frac{h\omega_{21}^3}{\pi^2 c_0^{\,3}} = B_{21} \frac{8\pi h \nu_{21}^3}{c_0^{\,3}}. \tag{G.15}$$

This compilation was extracted from [134,159,161].

Laser Rate Equations

The following equations described the superior case of the four level laser transitions. The time dependent population change of the upper level of the laser transition is given by [134]

$$\frac{dn_2}{dt} = -(n_2 - \frac{g_2}{g_1} n_1) c\phi\, \sigma_{em} - \frac{n_2}{\tau_{21} + \tau_{20}} + W_p n_0. \tag{G.16}$$

The time dependent population change of the terminal level of the laser transition is given by

$$\frac{dn_1}{dt} = (n_2 - \frac{g_2}{g_1} n_1) c\phi\, \sigma_{em} + \frac{n_2}{\tau_{21}} - \frac{n_1}{\tau_{10}}. \tag{G.17}$$

The populations N_1 of the terminal and N_2 of the upper laser level are now expressed as population densities n_1 and n_2, $n_{tot} = n_1 + n_2 + n_0$ with n_0 the ground state population density. The population of the pump band is assumed to be 0 since the transition from this level to the upper laser level occurs very rapidly. $c = c_0/n$ is the speed of light in the medium, ϕ is the photon density within the laser resonator and σ_{em} the stimulated emission cross section. W_P is the pumping rate already incorporating the quantum efficiency parameter.

The fluorescence lifetime τ_f is determined by the lifetime τ_{21} of the transitions from the upper laser level to the terminal level and to the ground state level τ_{20},

$$\frac{1}{\tau_f} = \frac{1}{\tau_{21}} + \frac{1}{\tau_{20}}. \tag{G.18}$$

Gain of a Fiber Laser

Already with low pumping rates high amplification values can be reached in a fiber. The gain g as function of the fiber length l is calculated with [9]

$$g(l) = -\sigma_a N_0 \eta_s l + (1+\gamma_S)\frac{\sigma_e \tau_2}{h\nu_p}\frac{P_{abs}}{A}\frac{F}{\eta_p}\xi, \tag{G.19}$$

where

N_0 = dopant concentration
σ_e = emission cross section
σ_a = absorption cross section
γ_s = σ_a / σ_e, adjusting factor
τ_2 = excited state lifetime
$h\nu_p$ = pump photon energy
P_{abs} = total pump power absorbed by the dopant
A = fiber core area
F = overlap between pump and signal mode profiles and dopant profile
η_p = overlap between pump mode intensity profile and dopant profile
η_s = overlap between signal mode intensity profile and dopant profile
ξ = correction term

Far below laser threshold, Eq. (G.19) signifies the small signal gain, e.g. in a fiber amplifier. Eq. (G.19) is general in that it can be applied to either a three- or a four level laser by simply adjusting the factor γ_s. The first term represents the unsaturated ground-state absorption (GSA) at the laser wavelength. For a four level laser, there is no signal GSA, and γ_s equals zero. The correction factor ξ accounts for pump exited state absorption (ESA) and also contains a small correction term owing to ground-state depletion. In the absence of ESA, under most practical operation conditions ξ is around 1 if pump and signal wavelengths are close. The fact that the laser medium is a waveguide is described by the spatial overlap integrals *F,*

η_p and η_s between the dopant distribution, the signal and/or the pump mode intensity profile. [9]

Just before laser action, on every complete two-way passage of the light through the fiber, the loss will just equal the gain. The threshold condition therefore is expressed by

$$G = \sqrt{R_1 R_2}\, e^{2(g-\alpha)l} = 1, \qquad \text{(G.20)}$$

with the reflectivities of the mirrors R_1 and R_2 and the absorption coefficient per unit length, α, representing all dissipative losses into a single parameter.

Excited atoms can not only lead to amplification by stimulated emission of radiation, but also to further absorption processes of the incident pump radiation. The laser threshold is raised and the slope efficiency reduced. In some cases, e.g. erbium doped ZBLAN[G] host fiber laser, this effect can be useful but in general ESA signifies unwanted losses.

[G] ZBLAN fibers are heavy metal fluoride glasses, e.g. $ZrFM_4$-BaF_2-LaF_3-AlF_3-NaF with Pb as an example for M.

Bibliography

[1] S. B. Poole, D. N. Payne, R. J. Mears, M. E. Fermann, and R.I. Laming. Fabrication and characterization of low-loss optical fibers containing rare-earth ions. *Journal of Lightwave Technology*, 4(7):870-876, 1986.

[2] S. Nagel, J. B. McChesney, and K. L. Walker. An overview over the Modified Chemical Vapour Deposition (MCVD) Process and Performance. *IEEE Journal of Quantum Electronics*, OE-18(4):459-476, 1982.

[3] J. MacChesney. MCVD: Its origin and subsequent development. *IEEE Journal of Selected Topics in Quantum Electronics*, 6(6):1305-1306, 2000.

[4] J. MacChesney and K. Walker. An overview of the modified chemical vapor deposition (MCVD) process and performance. *IEEE Journal of Quantum Electronics*, QE-18(4):459- 476, 1982.

[5] F. Wu, D. Machewirth, E. Snitzer and G.H. Sigel. An efficient single-mode Nd^{3+} fiber laser prepared by the sol-gel method. *Journal of Material Research*, 9:2703-2705, 1994.

[6] M. Locher, D. Michel, W. Lüthy, and H.P. Weber. Rare-earth doped sol-gel materials for optical waveguides. *Optics and Lasers in Engineering*, 43(3-5):341-347, 2005.

[7] H. Qiu, P. Yang, J. Dong, P. Deng, J. Xu, and W. Chen. The influence of Yb concentration on laser crystal Yb:YAG. *Materials Letters*, 55:1-7, 2002.

[8] H. M. Pask, R. J. Carman, D. C. Hanna, A. C. Tropper, C. J. Mackechnie, P. R. Barber, and J. M. Dawes. Ytterbium-doped silica fiber lasers: versatile sources for the 1-1.2 μm region. *IEEE Journal of Selected Topics on Quantum Electronics*, 1(1):2-13, 1995.

[9] M. J. F. Digonnet. Continuous-wave silica fiber lasers. *Rare-Earth-Doped Fiber Lasers and Amplifiers*, 113-170. Basel : Marcel Dekker Inc., 2001.

[10] A. A. Kaminskii. *Laser Crystals.* New York : Springer-Verlag, 1981.

[11] Z. Liu, N. Sarukura, and M.A. Dubinskii. All-Solid, Short-Pulse, Tunable, Ultraviolet Laser Sources Based on Ce^{3+}-Activated Fluoride Crystals. In: P. Misra and M.A. Dubinskii. *Ultraviolet Spectroscopy and UV Lasers*. New York [etc.] : Marcel Dekker, Inc., 2002.

[12] D.W. Coutts, and A.J.S. McGonigle. Cerium-Doped Fluoride Lasers. IEEE Journal of Quantum Electronics, 40(19):1430-1440 , 2004.

[13] S. Sudo. Progress in Optical Fiber Amplifiers, p19-21. *Current Trends in Optical Amplifiers and their Applications*. Teaneck NJ : World Scientific, 1996.

[14] J. Falbe and M. Regitz. *Römpp Chemie Lexikon*. Stuttgart : Thieme, 1995.

[15] W. A. Gambling, H. Masumura, and C. M. Ragdale. Zero-mode dispersion in single-mode fibers. *Electronics Letters*, 14(19):618-620, 1978.

[16] K. Yoshida. Preparation and preform fabrication of silica optical fibers. *Properties, Processing and Applications of Glass and Rare Earth-Doped Glasses for Optical Fibers*. Stevenage : Inspec, 1998.

[17] C. Brinker and G. Scherrer. *Sol-Gel science - the physics and chemistry of Sol-Gel processing*. San Diego : Academic Press, 1990.

[18] H. Murata. *Handbook of Optical Fibers and Cables*. Basel : Marcel Dekker, 1996.

[19] D. Barbier, X. Orignac, X. M. Du, and R. M. Almeida. Improved composition for sol-gel rare-earth doped planar waveguides. *Journal of Sol-Gel Science and Technology*, 8(1-3):1013-1016, 1997.

[20] K. Arai, H. Namikawa, K. Kumata, T. Honda, Y. Ishii, and T. Handa. Aluminum or phosphorus co-doping effects on the fluorescence and structural properties of neodymium-doped silica glass. *Journal of Applied Physics*, 59(10):3430-3436, 1986.

[21] J. K. Krebs and U. Happek. Yb^{3+} energy levels in α-Al_2O_3. *Journal of Luminescence*, 94-95:65-68, 2001.

[22] A. Patra, R. Reisfeld, and H. Minti. Influence of aluminum oxide on intensities of Sm^{3+} and Pr^{3+} spectral transitions in sol-gel glasses. *Materials Letters*, 73:325-329, 1998.

[23] F. Pedrotti, L. Pedrotti, W. Bausch, and H. Schmidt. *Optik: Eine Einführung*. Toronto : Prentice Hall, 1996.

[24] J. A. Buck. *Fundamentals of Optical Fibers*. Hoboken : John Wiley & Sons, 2004.

[25] M. Born. *Principles of Optics*. Cambridge : Cambridge University Press, 1999.

[26] J. D. Jackson. Classical Electrondynamics. New York [etc.] : Wiley, cop. 1999.

[27] B.E.A. Saleh, and M.C. Teich. Fundamentals of Photonics. New York [etc.] : Wiley, cop. 1991.

[28] S. G. Johnson and J. D. Joannopoulos. *Photonic Crystals: The Road from Theory to Practice*. Boston : Kluwer, 2002.

[29] F. Lederer. *Optics in Photonic Crystals*, talk. Bern : University Bern, 2005.

[30] D. Gloge. Weakly guiding fibers. *Applied Optics*, 10(10):2252-2258, 1971.

[31] Y. Katsuyama, M. Tokuda, N. Uchida, and M. Nakahara. New method for measuring V-value of a single-mode optical fiber. *Electronics Letters*, 12(25):669-670, 1976.

[32] K. S. Chiang. Finite element analysis of weakly guiding fibers with arbitrary refractive-index distribution. *Journal of Lightwave and Technology*, LT-4(8):980-990, 1986.

[33] S. Sakaguchi and S. Todoroki, D. Hewak. *Properties, Processing and Applications of Glass and Rare Earth-Doped Glasses for Optical Fibers*: Stevenage : Inspec, 1998.

[34] H. Kuhn and H.-D. Försterling. *Principles of Physical Chemistry*. New York : John Wiley & Sons, 1999.

[35] J.G. Nellist. *Understanding Telecommunications and Lightwave Systems*. New York : Wiley-IEEE Press, 1994.

[36] Polymicro Technologies, LLC. *The Book on the technologies of Polymicro*. Phoenix : Polymicro, 2004.

[37] D. Marcuse. *Light Transmission Optics*. New York : Van Nostrand Reinhold, 1982.

[38] O. Humbach, H. Fabian, U. Grzesik, U. Haken, and W. Heitman. Analysis of OH absorption in synthetic silica. *Journal of Non-Crystalline Solids*, 203:19-26, 1996.

[39] M. L. Hair. Hydroxyl groups on silica surface. *Journal of Non-Crystalline Solids*, 19:299-309, 1975.

[40] K. M. Davis and M. Tomozawa. An infrared spectroscopic study of water-related species in silica glasses. *Journal of Non-Crystalline. Solids*, 201(3):177-178, 1996.

[41] G. Klaus. *Glas I*, Lecture script. Zürich : Swiss Federal Institute of Technology Zürich, 2001.

[42] A. Bruce. Loss of silica fibers. *Properties, Processing and Applications of Glass and Rare Earth-Doped Glasses for Optical Fibers,* 65-68. Stevenage : Inspec, 1998.

[43] T. T. Volotinen, A. E. Konkarikoski, C. B. Arvidsson and T. K. Ericsson. Impact of silica glass structure on transmission properties of Ge-doped single-mode fibers. *Proceedings of SPIE*, 4940:1-13, 2003.

[44] Ministère de Culture et Communication. *La grotte de Lascaux*. URL: http://www.culture.gouv.fr/culture/arcnat/lascaux/fr, 2005-11-01.

[45] Wikipedia. *Cave of Lascaux*.
URL: http://en.wikipedia.org/wiki/Lascaux, 2005-10-29.

[46] M. Ruspoli. *Lascaux, Heiligtum der Eiszeit*. Basel : Herder, 1986.

[47] E. Chalmin, C. Vignaud, and M. Menu. Palaeolithic painting matter: natural or heat-treated pigment? *Applied Physics A - Materials Science & Processing,* 79(2):187-191, 2004.

[48] E. Chalmin, M. Menu, and C. Vignaud. Analysis of rock art painting and technology of Palaeolithic painters. *Measurement Science and Technology*, 14(9):1590-1597, 2003.

[49] V. Matejec, M. Hayer, M. Pospisililova, and I. Kasik. Preparation of optical cores of silica optical fibers by the sol-gel method. *Journal of Sol-Gel Science and Technology*, 8:889-893, 1997.

[50] V. Matejec, I. Kasik, M. Hayer, D. Berkova, M. Chomat, and J. Skokankova. Fabrication of Silica Optical Fibers Doped in the Core with Aluminium Oxide and Rare-Earth Elements by Using Xerogels. *Revue Roumaine de Chimie*, 47:1233-1239, 2002.

[51] T. Kitagawa, S. Shibata, and M. Horiguchi. Wholly synthesised fluorine-doped silica optical fibres by sol-gel method. *Electronics Letters*, 23(24):1295-1296, 1987.

[52] S. Shibata, T. Kitagawa, and M. Horiguchi. Fabrication of fluorine-doped silica glasses by the sol-gel method. *Journal of Non-Crystalline Solids*, 100(1-3):269-273, 1988.

[53] S. Shibata. Sol-gel-derived silica preforms for optical fibers. *Journal of Non-Crystalline Solids*, 178:272-283, 1994.

[54] K. Mauritz. *Sol-Gel Chemistry*.
URL: http://www.psrc.usm.edu/mauritz/solgel.html, 2005-10-29.

[55] C. Brinker. Sol to gel to glass: gelation and gel structure. *J. Non-Crystalline Solids*, 70(3):301-322, 1985.

[56] K. D. Keefer. Silicon Based Polymer Science: A Comprehensive Resource. *ACS Advances in Chemistry*, Ser. No. 224:227-240. Washington DC : American Chemical Society, 1990.

[57] R. Iler. *The Chemistry of Silica*. New York : Wiley, 1979.

[58] L. C. Klein. *Sol-Gel Technology for Thin Films, Fibers, Preforms, electronics and Specialty Shapes*. New Jersey : Noyes Publications, 1988.

[59] L. L. Hench and J. K. West. The Sol-Gel Process. *Chemical Reviews*, 90:33-72, 1990.

[60] D. R. Uhlmann, J. M. Boulton, G. Teowee, L. Weisenbach, and B. J. J. Zelinski. Sol gel synthesis of optical thin films and coatings. *Proceedings of the SPIE*, 1328:270-295, 1990.

[61] B. E. Yoldas. Process induced variations in sol-gel derived oxide coatings. *Proceedings of the SPIE*, 1328:296-306, 1990.

[62] Heraeus Glasschmelze, Heraeus Quarzglas GmbH & Co. KG. *Cleaning of Vitreous Silica*, Data Sheet Q-A3/131.2. Hanau : 2005.

[63] N. Porter. *Webster's Revised Unabridged Dictionary*, Springfield : C. & G. Merriam Co., 1913.

[64] P. Tosin. *Bedienungsanleitung für die Fiberproduktionsanlage des IAP bei Cableoptics SA in Cortaillod (NE)*, scientific report. Bern : University of Bern, 1997.

[65] R. Innocente. *Quartz glass types and properties for telecommunication applications*, personal communication and material data sheet. Bern/Zürich : 2005.

[66] A. Schreiber, Heraeus Glasschmelze, Heraeus Quarzglas GmbH & Co. KG. *Heraeus Lamp Material*, data sheets CILM.v.2.5, 2004.

[67] K. Lyytikäinen, S. T. Huntington, A. L. G. Carter, P. McNamara, S. Fleming, J. Abramczyk, I. Kaplin and G. Schötz. Dopant diffusion during optical fibre drawing. *Optics Express*, 12(6):972-977, 2004.

[68] P. McNamara, K. J. Lyytikainen, T. Ryan, I. J. Kaplin, and S. P Ringer. Germanium-rich "starburst" cores in silica-based optical fibres fabricated by modified chemical vapour deposition. *Optics Communications*, 230(1-3):45-53, 2004.

[69] R. Renner-Erny, L. Di Labio, and W. Lüthy. *On the Possibility of a Tb-doped Sol-Gel-based Fibre Laser*, research report. Bern : University Bern, 2005.

[70] J. R. Ferraro and L. J. Basile. *Fourier Transform Infrared Spectroscopy. Applications to Chemical Systems*, Vol.4. Orlando : London Academic Press Inc., 1985.

[71] K.I. White. Practical application of the refracted near-field technique for the measurement of optical fibre refractive index profiles. *Optical and Quantum Electronics*, 11(2):185-196, 1979.

[72] M. Hayer, V. Matejec, D. Berkova, I. Kasik, J. Kanka, P. Peterka, and P. Honzatko. Effect of High-Temperature Treatment on Optical Properties of Silica Films Doped with Al2O3, P2O5 and Rare-Earth Elements. *Journal of Sol-Gel Science and Technology*, 19:293-296, 2000.

[73] H.G. Pfaender. *Schott-Glaslexikon*. Landsberg am Lech : mvg-Verlag, 1997.

[74] D. Hewak. *Properties, Processing and Applications of Glass and Rare Earth-Doped Glasses for Optical Fibers*. Stevenage : Inspec, 1998.

[75] J.-W. Lee, G. H. Sigel Jr., and J. Li. Processing-induced defects in optical waveguide materials. *Journal of Non-Crystalline Solids*, 239(1-3):57-65, 1998.

[76] D. W. Hall, M. J. Weber, and R. T. Brundage. Fluorescence line narrowing in neodymium laser glasses. *Journal of Applied Physics*, 55(7):2642-2647, 1984.

[77] P. Tosin, W. Lüthy, and H.P.Weber. *Determination of the spectral absorption in silica samples with known rare earth dopant concentration*, scientific report. Bern : University of Bern, 1997.

[78] R. Paschotta, J. Nilson, P.R. Barber, J.E. Caplen, A.C. Tropper, and D.C. Hanna. Lifetime quenching in Yb-doped fibres, *Optics Communications*, 136:375-378, 1997.

[79] H. An, Y. Tang, P. McNamara and S. Fleming. Viewing structural inhomogeneities at the core-cladding interface of re-heated MCVD optical fiber preforms with optical microscopy. *Optics Express*, 12(25):6153-6158, 2004.

[80] P. K. Bachmann, W. Hermann, H. Wehr, and D. U. Wiechert. Stress in optical waveguides. I. Preforms. *Applied Optics*, 25(7):1093-1098, 1986.

[81] S. R. Nagel. Silica-based glass optical fiber properties and fabrication methods. *Proceeding of SPIE*, 1085:56-76, 1989.

[82] H. Borchers, H. Hausen, K.-H. Hellwege, KL. Schäfer, and E. Schmidt (eds). *Landolt–Börnstein*. Berlin : Springer Verlag, 1971.

[83] U. C. Paek and R. B. Runk. Physical behavior of the neck-down region during furnace drawing of silica fibers. *Journal of Applied Physics*, 49(8): 4417-4422, 1978.

[84] P. K. Bachmann, W. Hermann, H. Wehr, and D. U. Wiechert, Stress in optical waveguides. II. Fibers. *Applied Optics*, 26(7):1175-1182, 1987.

[85] P. K. Bachmann, D. U. Wiechert, and T. P. M. Meeuwsen. Thermal expansion coefficients of doped and undoped silica prepared by means of PCVD. *Journal of Materials Science*, 23(7):2584-2588, 1988.

[86] F. Dürr. *Laser-induced stress changes in optical fibers*, Dissertation 3314 (2005). Lausanne : École Polytechnique Fédérale de Lausanne, 2005.

[87] Y. Park, U.-C. Paek, and D. Y. Kim. Complete determination of the stress tensor of a polarization-maintaining fiber by photoelastic tomography. *Optics Letters*, 27(14):1217-1219, 2002.

[88] Y. Park, U.-C. Paek, S. Han, B. H. Kim, C. S. Kim, and D. Y. Kim. Inelastic frozen-in stress in optical fibers. *Optics Communications*, 242(4-6):431-436, 2004.

[89] P.Y. Fonjallaz, H. G. Limberger, R. P. Salathé, F. Cochet, and B. Leuenberger. Tension increase correlated to refractive-index change in fibers containing UV-written Bragg gratings. *Optics Letters*, 20(11):1346-1348, 1995.

[90] F. Dürr, H.G.Limberger, R.P. Salathe, F. Cochet, A.A. Rybaltovsky, Y.V. Larionov, S.L. Semjonov, and E.M. Dianov. UV-induced stress changes in phosphorous-doped fibers drawn at different drawing tensions. *Bragg Gratings, Photosensitivity, and Poling in Glass Waveguides*, paper WA2. Washington DC : OSA Technical Digest, 2003.

[91] F. Dürr. *Stress determination measurements*, personal communication. Lausanne : École Polytechnique Fédérale de Lausanne, 2005.

[92] M. F. Yan, J. B. MacChesney, S. R. Nagel, and W. W. Rhodes. Sintering of optical waveguide glasses. *Journal of Materials Science*, 15(6):1371-1378, 1980.

[93] K. Lu and N. K. Dutta. Spectroscopic properties of Yb-doped silica glass. *Journal of Applied Physics*, 91(2):576-581, 2002.

[94] D. W. Hall, W. F. Hagen, and M. J. Weber. Modelling Broad-Band and Multiple-Frequency Energy Extraction from Glass Laser Amplifiers. *IEEE Journal of Quantum Electronics*, QE-22(6):793-796, 1986.

[95] C. Jiang, H. Liu, Q. Zeng, Y. Wang, J. Zhang, and F. Gan. Stark energy split characteristics of ytterbium ion in glasses. In: S. Jiang (ed.). Rare-Earth-Doped Materials and Devices IV, *Proceedings of SPIE*, 3942:312-317, 2000.

[96] H. Hack and N. Neuroth. Resistance of optical and colored glasses to 3-nsec laser pulses. *Applied Optics*, 21(18):3239-3248, 1982.

[97] P. J. Suni, D. C. Hanna, R. M. Percival, I. R. Perry, R. G. Smart, J. E. Townsend, and A. C. Tropper. Lasing characteristics of ytterbium, thulium and other rare earth doped silica based fibers. *Proceedings of SPIE*, 1171:244-260, 1989.

[98] J. R. Armitage, R. Wyatt, B. J. Ainslie, and S. P. Craig-Ryan. Highly efficient 980 nm operation of an Yb^{3+}-doped silica fibre laser. *Electronics Letters*, 25(5):298-299, 1989.

[99] J. Y. Allain, J. F. Bayon, M. Monerie, P. Bernage, and P. Niay. Ytterbium-doped silica fibre laser with intracore Bragg gratings operating at 1.02 μm. *Electronics Letters*, 29(3):309-310, 1993.

[100] H. M. Pask, J. L. Archambault, D. C. Hanna, L. Reekie, P. St. J. Russell, J. E. Townsend, and A. C. Tropper. Operation of cladding-pumped Yb^{3+}-doped silica fibre lasers in 1 μm region. *Electronics Letters*, 30:863-864, 1994.

[101] A. Asseh, H. Storoy, J. T. Kringlebotn, W. Margulis, B. Sahlgren, R. Stubbe, and G. Edwall. 10 cm Yb^{3+} DFB fibre laser with permanent phase-shifted grating. *Electronics Letters*, 31(12):969-970, 1995.

[102] D. Inniss, D. J. DiGiovanni, T. A. Strasser, A. Hale, C. Headley, A. J. Stentz, R. Pedrazzani, D. Tipton, S. G. Kosinski, D. L. Brownlow, K. W. Quoi, K. S. Kranz, R. G. Huff, R. Espindola, J. D. LeGrange, G. Jacobovitz-Veselka, B. Boggavarapu, X. He, D. Caffey, S. Gupta, S. Srinivasan, K. McEuen, and R. Patel. Ultrahigh-power single-mode fiber lasers from 1.065 to 1.472 μm using Yb-doped cladding-pumped and cascaded Raman lasers. *Proceedings of the Conference on Lasers and Electro-Optics CLEO'97*, postdeadline paper CPD31. Baltimore : 1997.

[103] J. Swiderski, A. Zajac, M. Skorczakowski, Z. Jankiewicz and P. Konieczny. Rare-earth doped high-power fiber lasers generating in near infrared range. *Opto-electronics Review*, 12(2):169-173, 2004.

[104] V. P. Gapontsev, I. E. Samartsev, A. A. Zayats, and R. R. Loryan. Laser-diode pumped Yb-doped single mode tunable fibre lasers. *Conference about advanced solid state lasers*, paper WC1-1:214-216. Hilton Head (NC) : 1991.

[105] M. Muendel, B . Engstrom, D. Kea, B. Laliberte, R. Minns, R. Robinson, B . Rockney, Y. Zhang, R. Coilins, P. Gavrilovic, and A. Rowley. 35-W single-mode ytterbium fiber laser at 1.1 μm. *Proc. Conf Lasers Electro-Optics, CLEO'97*, Postdeadline paper CPD30, 1997.

[106] C. J. Mackechnie, W. L. Barnes, D. C. Hanna, and J. E. Townsend. High-power ytterbium (Yb^{3+})-doped fiber laser operating in the 1.12 μm region. *Electronics Letters*, 29(1):52-53, 1993.

[107] U. Haken, O. Humbach, S. Ortner, and H. Fabian. Refractive index of silica glass: influence of fictive temperature. *Journal of Non-Crystalline Solids*, 256:9-18, 2000.

[108] H.-Y. Lee. *Herstellung und Sinterverhalten durch Nd-YAG Laserstrahlung hergestellter ultrafeiner Oxidpulver*, Dissertation. Clausthal : Technische Universität Clausthal, 1992.

[109] S. I. Dolgaev, A. V. Simakin, V. V. Voronov, G. A. Shafeev, and F. Bozon-Veruraz. Nanoparticles produced by laser ablation of solids in liquid environment. *Applied Surface Science*, 186(1-4):546-551, 2002.

[110] A. V. Simakin, V. V. Voronov, N. A. Kirinchenko, and G. A. Shafeev. Nanoparticles produced by laser ablation of solids in liquid environment. *Proceedings of SPIE*, 5121, 2002.

[111] J. Lee, M. F. Becker, and J. W. Keto. Dynamics of laser ablation of microparticles prior to nanoparticle generation. *Journal of Applied Physics*, 89(12):8146-8152, 2001.

[112] X. Li, H. Liu; J. Wang; X. Zhang and H. Cui. Preparation and properties of YAG nanosized powder from different precipitation agent. *Optical Materials*, 25(4):407-412, 2004.

[113] D. Hreniak and W. Strek. Synthesis and optical properties of Nd^{3+}-doped $Y_3Al_5O_{12}$ nanoceramics. *Journal of Alloys and Compounds*, 341:183-186, 2002.

[114] D. Hreniak, W. Strek, and P. Mazur. Preparation, spectroscopy and morphology of Nd:YAG nanostructures. *Materials Science*, 20(2):39-45, 2002.

[115] S. Singh, W. A. Bonner, W. H. Grodkiewicz, M. Grasso, and L. G. Van Uitert. Nd-doped yttrium aluminum garnet with improved fluorescent lifetime of the $^4F_{3/2}$ state. *Applied Physics Letters*, 29(6):343-345, 1976.

[116] Y. C. Kang, S. B. Park, I. W. Lenggoro, and K. Okuyama. Preparation of non-aggregation YAG-Ce phosphor particles by spray pyrolysis. *Journal of Aerosol Science*, 29(Suppl.1):S911-S912, 1998.

[117] B. C. Kim, H. Uono, T. Fuse, T. Ishihara, and M. Senna. Fabrication of nanosized Si powders with a narrow size distribution by two-step milling. *Journal of Materials Research*, 18(6):1368-1373, 2003.

[118] H. Minti, M. Eyal, R. Resifeld, and G. Berkovic. Quantum dots of cadmium sulfide thin glass films prepared by sol-gel technique. *Chemical Physics Letters*, 183:277-282, 1991.

[119] J. Hecht. *City of Light: The Story of Fiber Optics*. New York : Oxford University Press, 1999.

[120] H. P. Christensen, D. R. Gabbe, and H. P. Jenssen. Fluorescence lifetime for neodymium-doped yttrium aluminium garret and yttrium oxide powders. *Physical Review B*. 25(3):1467-1473, 1982.

[121] A. A. Kaminskii, K. Ueda, A. F. Konstantinova, H. Yagi, T. Yanagitani, A. V. Butashin, V. P. Orekhova, J. Lu, K. Takaichi, T. Uematsu, M. Musha, and A. Shirokava. Refractive Indices of Laser Nanocrystalline Ceramics Based on $Y_3Al_5O_{12}$. *Crystallography Reports*, 48(5):868-871, 2003.

[122] A. A. Kaminskii, M. Sh. Akchurin, V. I. Alshits, K. Ueda, K. Takaichi, J. Lu, T. Uematsu, M. Musha, A. Shirikawa, V. Gabler, H. J. Eichler, H. Yagi, T. Yanagitani, S. N. Bagayev, J. Fernandez, and R. Balda. New Data on the Physical Properties of $Y_3Al_5O_{12}$–Based Nanocrystalline Laser Ceramics. *Crystallography Reports*, 48(3):562-519, 2003

[123] G. A. Kumar, J. Lu, A. A. Kaminskii, K. Ueda, H. Yagi, T. Yanagitani, and N. V. Unnikrishnan. Spectroscopic and Stimulated Emission Characteristics of Nd^{3+} in Transparent YAG Ceramics. *IEEE Journal of Quantum Electronics*, 40(6):747-758, 2004.

[124] Y. Feng, J.-F. Bisson, J. Lu, S. Huang, K. Takaichi, A. Shirakawa, M. Musha, and K. Ueda. Thermal effects in quasi-continuous-wave Nd^{3+}- $Y_3Al_5O_{12}$ nanocrystalline-powder random laser. *Applied Physics Letters*, 84(7):1040-1042, 2004.

[125] Z. He, K. Chen, J. Xu, D. Feng, H. Han, and Z. Wang. Luminescent Ge nanocrystallites embedded in a-SiO_2 films. *Proceedings of SPIE*, 3175:37-41, 1998.

[126] H. K. Schmidt and M. Mennig. Optical Materials by a Modified Sol-Gel Nanoparticle Process. *Proceedings of SPIE*, 3943:74-84, 2000.

[127] A. Matsuda, Y. Kotani, T. Kogure, T. Umezawa, M. Tatsumisago, and T. Minami. Preparation of transparent anatase nanocrystals-dispersed silica films via sol-gel process at low temperatures. *Proceedings of SPIE*, 3943:85-94, 2000.

[128] S. J. L. Ribeiro, R. R.Goncalves, Y. Messaddeq, M. A. Aegerter, M. Montagna, C. Duverger, and M. Ferrari. Rare earth doped HfO_2 nanoparticles embedded in SiO_2-HfO_2 planar waveguides. Preparation, optical, structural and spectroscopic characterization. *Proceedings of SPIE*, 3943:10-18, 2000.

[129] W. Miniscalco. Optical and Electronic Properties of Rare Earth Ions in Glasses. *Rare-Earth-Doped Fiber Lasers and Ampifiers*, 2nd edited, revised and expanded. Basel : Marcel Dekker Inc., 2001.

[130] A. Kiel. Multi-Phonon Spontaneous Emission in Paramagnetic Crystals. *Third International Conference on Quantum Electronics*, 1:765-772. New York : Columbia University Press, 1963.

[131] L. A. Riseberg and H. W. Moos. Multiphonon Orbit-Lattice Relaxation of Excited States of Rare-Earth Ions in Crystals. *Physical Review*, 174(2):429-438, 1986.

[132] H. G. Danielmeyer, M. Blatte, and P. Balmer. Fluorescence quenching in Nd:YAG. *Applied Physics*, 1(5):269-274, 1973.

[133] G. L .J .A. Rikken and Y. A. R. R. Kessender. Local Field Effects and Electric and Magnetic Dipole Transitions in Dielectrics. *Physical Review Letters*, 74(6):880-883, 1995.

[134] W. Koechner. *Solid-State Laser Engineering*. Heidelberg : Springer Verlag, 1999.

[135] R. S. Meltzer, S. P. Feofilov, B. Tissue, and H. B. Yuan, Dependence of fluorescence lifetimes of $Y_2O_3:Eu^{3+}$ nanoparticles on the surrounding medium. *Physical Review B*, 60(20):R14012-R14015, 1999.

[136] E. Yablonovitch, T. J. Gitter, and R. Bath. Inhibited and Enhanced Spontaneous Emission from Optically Thin AlGaAs/GaAs Double Heterostructures. *Physical Review Letters*, 61(22):2546-2549.

[137] D. Toptygin. Effects of the Solvent Refractive Index and Its Dispersion on the Radiative Decay Rate and Extinction Coefficient of a Fluorescent Solute. *Journal of Fluorescence*, 13(3):201-219, 2003.

[138] U. Gerber : *Milling data and experiences*, personal communication. Idar-Oberstein : 2003.

[139] International Centre for Diffraction Data JCPDS. *Selected Powder Diffraction Data for Metals and Alloys,* Data Book Volume I and II(patterns 13-307 and 24-1164). Pennsylvania : 1978.

[140] International Centre for Diffraction Data JCPDS, *Database PCPDFWIN v. 2.2*(patterns 77-0602 and 77-0603). Pennsylvania : 1978.

[141] T. Tadros. *Solid liquid dispersions*. London : Academic Press Inc., 1987.

[142] R. C. Weast (ed). *Handbook of Chemistry and Physics*. Cleveland : CRC Press, 1973.

[143] St. Herr, K. Kömpe, H.-U. Güdel, and M. Haase. Highly Efficient Multicolor Upconversion Emission in Transparent Colloids of Lanthanide-Doped NaYF4 Nanocrystals. *Advanced Materials*, 16(23-24):2102-2105, 2004.

[144] T. Yanagitani, H. Yagi, and M. Ichikawa, *Japanese Patent* 10-101333, 1998.

[145] T. Yanagitani, H. Yagi, and M. Yamasaki, *Japanese Patent* 10-101411, 1998.

[146] M. Semita, H. Haneda, T. Yanagitani, and S. Shirasaki. Induced emission cross section of Nd:$Y_3Al_5O_{12}$ ceramics. *Journal of Applied Physics*, 67(1):453-458, 1990.

[147] Ju. Lu, Ji. Lu, A. Shirakawa, K. Ueda, H. Yagi, T. Yanagitani, V. Gabler, H. J. Eichler, and A. A. Kaminskii. New Highly Efficient 1.3 μm CW Generation in the $^4F_{3/2} \rightarrow {}^4I_{13/2}$ Channel of the Nanocrystalline Nd^{3+}:$Y_3Al_5O_{12}$ Ceramic Laser under Diode Pumping. *Physica Status Solidi (A)*, 189(2):R11-R13, 2002.

[148] Ji. Lu, K. Ueda, H. Yagi, T. Yanagitani, Y. Akiyama and A. A. Kaminskii. Neodymium doped yttrium aluminum garnet ($Y_3Al_5O_{12}$) nanocrystalline ceramics – a new generation of solid state laser and optical materials. *Journal of Alloys and Compounds*, 341:220-225, 2002.

[149] A. A. Kaminskii, H. J. Eichler, K. Ueda, S. N. Bagaev, G. M. A. Gad, J. Lu, T. Murai, H. Yagi, and T. Yanagitani. Observation of stimulated raman scattering in $Y_3Al_5O_{12}$ single crystals and nanocrystalline ceramics and in these materials activated with laser ions Nd^{3+} and Yb^{3+}. *JETP Letters*, 72(10):499-502, 2000.

[150] J. Lu, M. Prabbu, J. Song, C. Li, J. Xu, K. Ueda, A. A. Kaminskii, H. Yagi, and T. Yanagitani. Optical properties and highly efficient laser oscillation of Nd.YAG ceramics. *Journal of Applied Physics B*, 71:469-473, 1991.

[151] C. Urlacher. *Corrélations entre microstructure et propriétés de guidage optique de couches de minces élaborées par le sol-gel : application au ZrO_2 et au titanate de plomb*, dissertation. Lyon : Université de Claude Berndard, 1996.

[152] A. Tomczak, RDH. *Certificate of analysis inspection*, certificate B acc. to EN 10204 : Seelze, RDH Laborchemikalien GmbH & Co., 1999.

[153] M. J. Folkes and R. G. C. Arridge. The measurement of shear modulus in highly anisotropic materials: the validity of St Venant's principle. *Journal of Physics D: Applied Physics*, 8:1053-1064, 1975.

[154] A. E. Puro and K.-J. E. Kell. Complete Determination of Stress in Fiber Preforms of Arbitrary Cross Section. *Journal of Lightwave Technology*, 10(8):1010-1014, 1992.

[155] C. J. Dasch. One-dimensional tomography: a comparison of Abel, onion-peeling, and filtered backprojection methods. *Applied Optics*, 31(8):1146-1152, 1992.

[156] A. C. Kak and M. Slaney. *Principles of Computerized Tomographic Imaging*, chapter 3. Philadelphia : Society for Industrial and Applied Mathematics, 2001.

[157] T. Abe, Y. Mitsunaga, and H. Koga. Photoelastic computer tomography: a novel measurement method for axial residual stress profile in optical fibres. *Journal of the Optical Society of America A (Optics and Image Science)*, 3(1):133-138, 1986.

[158] F. Dürr, H. G.Limberger, R. P. Salathe, F. Hindle, M. Douay, E. Fertein, and C. Przygodzki. Tomographic measurements of femtosecond-laser induced stress changes in optical fibers. *Applied Physics Letters*, 84(24):4983-4985, 2004.

[159] Th. Feurer. *Experimentelle Optik*, lecture script. Bern : Universität Bern, 2005.

[160] A. Einstein. Über einen die Erzeugung und Verwandlung des Lichtes betreffenden heuristischen Gesichtspunkt. *Annalen der Physik*, 4(17):132-148, 1905.

[161] D. Hanna. Fibre Lasers. In: C.E. Webb and J.D. Jones (eds.). *Handboook of Laser Technology and Applications*, Vol II:963-976. Philadelphia : Institute of Physics Publishing, 2004.

Acknowledgments

This thesis is the result of my research work at the Advanced Photonics Laboratory of the Swiss Federal Institute of Technology Lausanne, and the Institute of Applied Physics at the University of Bern, in the years 2002-2005.

I thank especially my parents for their unshakable support and believing in me!

First of all I want to thank Prof. René P. Salathé, the director of my PhD committee, and the members of my committee Prof. Willy Lüthy, Dr. Markus Pollnau and Dr. Valerio Romano. I was able to start in Berne also thanks to Prof. Heinz P. Weber. I thank you all for the chance to work on this project, and for your assistance and support. Later on, the head of my research unit in Bern became Prof. Thomas Feurer. He had always time to give me his support and to share with me his enthusiasm for physics. Many times my eyes were opened by these teachers for important details and coherences. I will never forget e.g. Willy Lüthy's "have a seat" (in order to elaborate together the solution for a particular problem and to revise manuscripts) and Valerio Romano's active and experienced aid in the laboratory as well as for writing scientific papers.

I express my gratitude to Prof. Nava Setter and Prof. Philippe Renaud who kindly accepted to be on my exam jury!

I thank the staff at the IAP and the APL for the excellent atmosphere at work and for the cordial hospitality! I benefit from endless help and an immeasurable pool of knowledge. I always felt it a great privilege to study and to work in these surroundings with all these experts! The co-operation in the research teams at the IAP and the APL was very amicable and productive, and many laughs inspired the every day work life! When I started with my work, Gabriel Dumitru welcomed me not only with a cordial "welcome on board" but also with an efficient introduction to the equipment. I was temporarily office guest in the group of Jürg Balmer, Maité Braud, Michael Grünig and Felix Staub – thank you for the hospitality. The discussions with Peter Blattnig were always bright and broadened my scientific horizon. Eva Krähenbühl performed many SEMs and never failed to share her vast experience with me, and Werner Lüscher, Hans Lüthi and Samuel Studer created countless artful constructions, many of them as a case of emergency, and Martin Locher and Ruth Renner-Erny often not only helped me to find and to put away the equipment, but also in optimizing setups. The camaraderie with Dietrich Feist, Andreas Galler, Roger Hänni, Beat Hiltbrunner, Niklaus Jaussi, Matthias Meier, Peter Peier and Daniel Weber was sportively motivating, not only professionally. I am grateful to Andreas Friedrich, Beat Locher, Peter Oberli, Alfred Stähli, Hansjürg Weder and Max Wüthrich for technical support.

I thank Guido Bucher for DLS measurements, and together with Jaroslav Ricka and Petr Hajicek for fruitful discussions, Laetitia Laversenne for instructions in grinding and polishing planar waveguides, and together with Camelia Borca and Yaroslav Romanyuk for their assistance in Lausanne. The tomographic investigations were performed together with Christian Ban, Florian Dürr, Hans G. Limberger and Julien Sauvet. I learned a lot from these experts. I thank Philipp Burmester (Institute of Laser-Physics, University of Hamburg, Germany) for helpful suggestions, Urs Krähenbühl and Edith Vogel (Department of Chemistry and Physics, Uni Bern) for preliminary mill tests, Hans Leber and Thomas Gerber (PSI Paul Scherrer Institut, Switzerland) for their help in getting XRD data. I thank the secretaries at the APL and the IAP for providing the administrative infrastructure, especially Yvette Bernhard for the assistance at the EPFL, and Beatrice Thut for the many hints and tips in and around Berne, and the delightful Bernese term for sweets, "Güezi", which I will use for the rest of my life. The staff of the Library of Exact Sciences many times traced publications difficult to get and shared their know-how with me during lunch.

I'm grateful to Peter Blattnig, Andreas Galler, Luca Modolo and Sophie Thompson for cross-reading reports and manuscripts.

I was experiencing countless personally valuable and enriching contacts during this thesis.

This work was mainly supported in part by the Swiss National Centre for Competence in Research (NCCR), Quantum Photonics Project 8 High Power Laser. This financial support was greatly appreciated.

Among my private friends, especially Cornelia Berchtold-Büechi, Thomas Buck, Peter Müllner and Isabel Thoma: thank you for advices and inspirations, and thank you, Sandra and Theo Meister-Sordo, for your inspiring and delicious hospitality!

I am for ever grateful for being born and raised in this country, to benefit from its outstanding social, cultural and technological infrastructure, to attend its excellent schools, in this safe and secure environment, especially in the cities of Bern, Biel-Bienne, Lausanne and Zürich.

Thanks to God for this privileged life!

Lausanne, Dezember 2005
Urs Pedrazza

Curriculum Vitae

Urs Pedrazza

Email	urs@pedrazza.ch	
PhD thesis	2002-2005	Swiss Federal Institute of Technology Lausanne (EPFL) in collaboration with the University of Bern
Diploma thesis	2002	Sulzer Innotec
Diploma	1995-2001	Certified materials science engineer at the Swiss Federal Institute of Technology Zürich (ETHZ)
Matura	1992-1995	General qualification for university entrance, school for extension studies, canton Zürich
Employment	1990-1993	Chemical laboratory assistant at the ETHZ
Apprenticeship	1987-1990	Chemical laboratory assistant at the ETHZ
Elementary School	9 years, obligatory schooldays in Zürich	